The Optical Properties of Silicon Nanocrystals and the Role of Hydrogen Passivation

Andrew Richard Wilkinson

January 2006

A thesis submitted for the degree of

Doctor of Philosophy

of

The Australian National University.

CERTIFICATE

This thesis, to the best of my knowledge and belief, does not contain any results previously published by another person or submitted for a degree or diploma at any university except where due reference is made in the text.

Andrew R. Wilkinson

January 31, 2006

Acknowledgements

First and foremost I would like to thank my excellent supervisor Prof. Rob Elliman. I could not have hoped for a better mentor. His dedication, knowledge, and skill as a research scientist are an inspiration. Thank you.

Next I would like to thank the rest of the research group: my fellow students Nat Smith and Marc Spooner and postdoctoral fellows Dr. Tessica Dall and Dr. Manuel Forcales for making the last few years friendly, enjoyable and rewarding.

I would also like to thank the people of EME in general, for providing a friendly and flexible place to work.

I would like to thank and acknowledge contributions from the following people:

- my advisory panel Prof. Barry Luther-Davies and Prof. Andres Cuevas. In particular, I would thank Barry for performing the PDS measurements (Chapter 3) and Andres for introducing me to the *alneal* process (Chapter 6) and providing access to the CSES group facilities
- Chris Samundsett, for growing a range of high quality thermal oxides (used throughout the thesis) and sample cutting (Chapter 4)
- Dr. Terry Mernagh of Geoscience Australia for his patient help and access to his Raman system (Chapter 4), at a time where every Argon ion laser we touched would spontaneously fail!
- Prof. Elmars Krausz of RSC for access to his equipment over the years. In particular, a high sensitivity Ge detector (Chapter 7). Also Dr. Barry Prince of RSC for performing some preliminary Raman measurements.

- Dr. Tessica Dall for suggesting corrections to this thesis
- Dr. Manuel Forcales for his contributions to the work presented in Chapter 7
- Ben Cornish of RPO, for precision cutting of some samples
- Dr Sanju Deenapanray of CSES for annealing some samples
- Glen McCarthy of LPC for generously sharing access to the sole copy of TFCalc, which he depended on.
- Dr. Zou Jin of UQ (formerly of USyd) for preparing samples for and imaging with high-resolution TEM (Chapter 2).
- Non-academic staff at EME, especially Martin Conway, Tom Halstead and Fred Johnson, for keeping everything running smoothly, and Renee Vercoe for keeping EME running
- The School Computer Unit
- DEST for my APA Scholarship, and the RSPhysSE/ANU for my supplementary scholarship, and the Student Convenor Prof. Neil Manson for being so friendly and understanding.
- anyone else I may have neglected to mention

Last, but certainly not least, I am indebted to the support of my family and friends. Thank you Mum and Dad for supporting whatever I do. Thank you 5263 crew and associates for many fun and "crazy" years. Thank you my Biarittz "that's livin'" flatmates for the many good times. Thank you Kristy, for helping me so much over the years - I wouldn't have been able to do it without you. And thank you Nu Nu for all your support and for keeping me on track throughout my thesis writing.

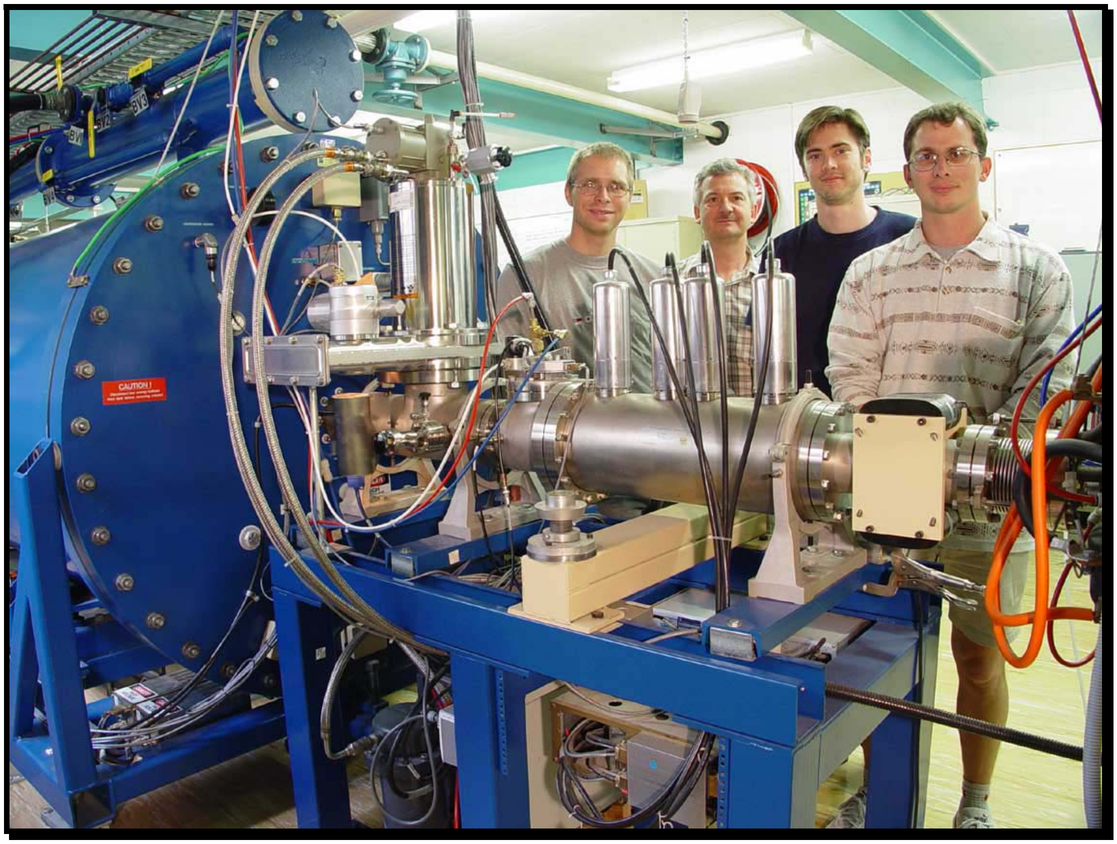

Si Nanocrystal Colleagues with HE implanter, ANU. Left to right: Marc Spooner, Prof. Rob Elliman, yours truly, and Nat Smith.

Abstract

This thesis examines the optical properties of nanoscale silicon and the sensitization of Er with Si. In this context, it predominantly investigates the role of defects in limiting the luminescence of Si nanocrystals, and the removal of these defects by hydrogen passivation. The kinetics of the defect passivation process, for both molecular and atomic hydrogen, are studied in detail. Moreover, the optical absorption of Si nanocrystals and the effect of annealing environment (during nanocrystal synthesis) on the luminescence are investigated. The effect of annealing temperature and hydrogen passivation on the coupling (energy transfer) of Si nanocrystals to optically active centres (Er) is also examined.

The electronic structure of silicon-implanted silica slides is investigated through optical absorption measurements. Before and after annealing to form Si nanocrystals, optical absorption spectra from these samples show considerable structure that is characteristic of the particular implant fluence. This structure is shown to correlate with the transmittance of the samples as calculated from the modified refractive index profile for each implant. Due to the high absorption coefficient of Si at short wavelengths, extinction at these wavelengths is found to be dominated by absorption. As such, scattering losses are surprisingly insignificant. To eliminate interference effects, photothermal deflection spectroscopy is used to obtain data on the band structure of Si in these samples. This data shows little variance from bulk Si structure and thus little effect of quantum confinement. This is attributed to the dominance of large nanocrystals in the absorption measurements.

The effect of annealing environment on the photoluminescence (PL) from silicon nanocrystals synthesized in fused silica by ion implantation and thermal annealing is studied as a function of annealing temperature and time. Interestingly, the choice of annealing environment (Ar,

N_2, or 5 % H_2 in N_2) is found to affect the shape and intensity of luminescence emission spectra, an effect that is attributed both to variations in nanocrystal size and the density of defect states at the nanocrystal/oxide interface.

The passivation kinetics of luminescence-quenching defects, associated with Si nanocrystals in SiO_2, during isothermal and isochronal annealing in molecular hydrogen are studied by time-resolved PL. The passivation of these defects is modeled using the Generalized Simple Thermal model of simultaneous passivation and desorption, proposed by Stesmans. Values for the reaction-rate parameters are determined for the first time and found to be in excellent agreement with values previously determined for paramagnetic Si dangling-bond defects (P_b-type centers) found at planar Si/SiO_2 interfaces; supporting the view that non-radiative recombination in Si nanocrystals is dominated by such defects.

The passivation kinetics of luminescence-quenching defects during isothermal and isochronal annealing in atomic hydrogen are studied by continuous and time-resolved PL. The kinetics are compared to those for standard passivation in molecular hydrogen and found to be significantly different. Atomic hydrogen is generated using the *alneal* process, through reactions between a deposited Al layer and H_2O or –OH radicals in the SiO_2. The passivation and desorption kinetics are shown to be consistent with the existence of two classes of non-radiative defects: one that reacts with both atomic and molecular hydrogen, and the other that reacts only with atomic hydrogen. A model incorporating a Gaussian spread in activation energies is presented that adequately describes the kinetics of atomic hydrogen passivation and dissociation for the samples.

The effect of annealing temperature and hydrogen passivation on the excitation cross-section and PL of erbium in silicon-rich silica is studied. Samples are prepared by co-implantation of

Si and Er into SiO_2 followed by a single thermal anneal at temperatures ranging from 800 to 1100 °C, and with or without hydrogen passivation performed at 500 °C. Using time-resolved PL, the effective erbium excitation cross-section is shown to increase by a factor of 3, while the number of optically active erbium ions decreases by a factor of 4 with increasing annealing temperature. Hydrogen passivation is shown to increase the luminescence intensity and to shorten the luminescence lifetime at 1.54 μm only in the presence of Si nanocrystals. The implications of these results for realizing a silicon-based optical amplifier are also discussed.

Journal Publications Related To This Thesis

Chapter 4:

- A. R. Wilkinson and R. G. Elliman, "The effect of annealing environment on the luminescence of silicon nanocrystals in silica", *J. Appl. Phys.* **96**, 4018 (2004)

Chapter 5:

- A. R. Wilkinson and R. G. Elliman, "Kinetics of H_2 passivation of Si nanocrystals in SiO_2", *Phys. Rev. B* **68**, 155302 (2003)

- R. G. Elliman, A. R. Wilkinson, N. Smith, M. G. Spooner, T. D. M. Weijers, M. J. Lederer, B. Luther-Davies, M. Samoc, "Light emission from Si nanocrystals - size does matter !", *J. Korean Phys. Soc.* **45**, s656 (2004)

Chapter 6:

- A. R. Wilkinson and R. G. Elliman, "Maximizing light emission from Si nanocrystals - the role of hydrogen", *Nucl. Instr. Methods Phys. Res. B* **242***, 303* (2006)

- A. R. Wilkinson and R. G. Elliman, "Passivation of Si nanocrystals in SiO_2: atomic versus molecular hydrogen", *Appl. Phys. Lett.* **83**, 5512 (2003)

- R. G. Elliman, T. D. M. Weijers-Dall, M. G. Spooner, Tae-Hyun Kim, and A. R. Wilkinson, “Stress and stress relief in dielectric thin films –the role of hydrogen”, *Nucl. Instr. Methods Phys. Res. B,* accepted (2005)

Chapter 7:

- A. R. Wilkinson, M. Forcales, and R. G. Elliman, “The effect of annealing temperature and hydrogen passivation on the sensitization of erbium in silicon-rich silica”, *Appl. Phys. Lett.*, submitted (2005)

Table of Contents

CHAPTER
1

Introduction

1.1 Motivation

The success of today's microelectronic industry is based on silicon.[1] Silicon as a material is widely available, can be highly purified, and has favourable thermal and mechanical properties, all which render the processing of devices based on it straightforward. Moreover, and perhaps most importantly, the natural oxide of silicon (SiO_2), effectively passivates the surface of silicon, is an excellent insulator and diffusion barrier and has a very high etching selectivity with respect to silicon.

However, concerns about the continuing success of the microelectronics industry related to fundamental and processing aspects have been raised in recent years.[1, 2] An important example is related to the limitation of the operating speed of microelectronic devices due to the interconnects. As gate lengths decrease, a situation is reached where the delay due to the interconnect exceeds the gate switching delay. A possible solution to this and the problems associated with the increasing complexity of the interconnect architecture, is the use of optical interconnects. Due to its compatibility with the microelectronics industry, silicon is the obvious material of choice. This is one of the main driving forces behind silicon optoelectronics.[1]

Another driving force is the communications industry. Most of the components currently used in communication systems are heavily based on technologies other than that of silicon. However a niche exists for silicon where cost-effective solutions are required. For example, at low bit-rates and short distances where Si-based optoelectronics are predicted to meet most requirements at a lower cost, exploiting the compatibility with Si-technology in terms of functionality, compactness, reliability and production yield.[3]

The development of Si-based photonics has lagged far behind the development of electronics for a long time.[4] The main reason for this slow progress has been the lack of practical Si light sources, i.e., efficient Si light-emitting diodes (LED) and injection lasers. This is because Si is an indirect-band-gap material. Lasing is also hindered by fast non-radiative processes such as Auger or free-carrier absorption that strongly prevent population inversion at the high pumping rates needed to achieve optical amplification. However, many different strategies have been employed to overcome these material limitations. Present-day Si LEDs are only a factor of ten away from the market requirements[5, 6] and optical gain has been reported.[7] Availability of Si nanotechnology played a primary role in these achievements.[4]

1.2 Unique Properties of Silicon Nanocrystals

Bulk silicon is an indirect bandgap semiconductor with a centro-symmetric crystalline structure. As a result, bulk silicon is not directly suited for optoelectronics. The indirect bandgap makes light emission by free carrier recombination extremely unlikely, whilst the lattice symmetry results in the lack of electro-optic (Pockels) effect. Moreover, the bulk Si bandgap of 1.16 eV (1.07 μm) prevents its use for light detection at the technologically important 1.3 and 1.55 μm.[3] Therefore, several approaches have been attempted, to date, and a large amount of resources have been devoted to improving the optoelectronic capabilities silicon. This effort, with prototypic devices demonstrated, has included doping with active impurities (e.g. Er), the use of new phases such as silicides (e.g. Fe_2Si_3), and direct modification of the bandstructure of Si by alloying (e.g. alloys of Si with Ge, Sn and/or C). However, a major change in emphasis was brought about by the discovery in 1990 that porous Si, a sponge-like form of silicon produced by electrochemical etching, exhibited strong visible luminescence at room temperature.[8] The strong luminescence of porous Si is based on the lifting of the lattice periodicity inducing an uncertainty in the k-space and therefore altering the indirect nature of this material.[9, 10]

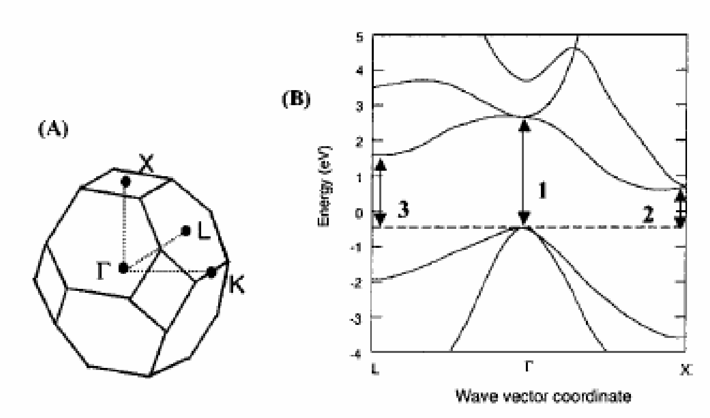

Figure 1-1: (a) Brillouin zone for the diamond lattice, and (b) bulk bandstructure of Si. The arrows in (b) indicate the energies of the direct (1) and indirect phonon assisted transitions Γ → X (2) and Γ → L (3).[11]

As a consequence of its indirect band gap (see Figure 1-1), bulk Si has a typical room temperature quantum efficiency of < 0.001% compared to around 1 – 10 % for GaAs light-emitting diodes and around 30 % for specialised GaAs and InP devices. This poor efficiency results primarily from the fact that the lowest energy transition (Γ → X, see Figure 1-1), violates conservation of momentum and therefore requires phonon assistance. As a consequence, the exciton lifetime is very long and non-radiative recombination dominates the relaxation process. In nanoscale structures, the requirement for momentum conservation is relaxed and the probability for direct transitions is increased.[8, 12] The number of non-radiative centres is also reduced by the small scale of the material. Under such conditions, radiative recombination can become a competitive relaxation mechanism.

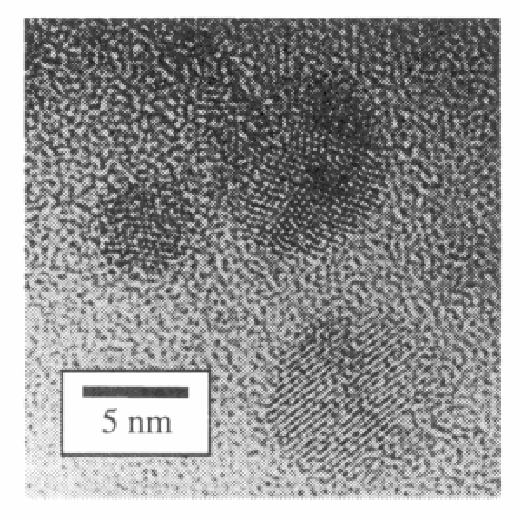

Figure 1-2: TEM image of nanocrystals in SiO_2 formed by ion-implantation of Si into SiO_2 followed by thermal annealing.[13]

Quantum confinement effects only become significant when the nanocrystal dimensions are of the order of, or less than, the Bohr radius of excitons (~4.9 nm for Si). Crystallites of this size are present in porous silicon. An alternative fabrication method produces Si nanocrystals in SiO_2 by the precipitation and growth of excess silicon, as shown in Figure 1-2, and was the method used in this thesis. The most obvious consequences of such carrier confinement are an increase in the Si bandgap energy, and an increase in the oscillator strength for optical transitions. The former results in a blue shift of the optical emission with decreasing particle size, and hence enables the emission to be tuned, whilst the latter increases the probability for such emission. A theoretical model for the size (d) dependence on the luminescence based on the quantum confinement effect has been proposed by Ranjan *et al.,*[14] which takes into account the volume of the crystal ($V \propto d^3$), the energy upshift of the band gap ($\Delta E \propto d^{-x}$), the variation in oscillator strength ($f_{osc} \sim d^{-\beta}$), and the size distribution of nanocrystals (Gaussian: $P(d) \propto \exp\left[\frac{-(d-d_0)^2}{2\sigma^2}\right]$). The main prediction of this simple model is a red-shift in luminescence and a narrowing of the spectral width (for fixed σ) with increasing nanocrystal diameter, as shown in Figure 1-3. Another major contribution to the increase in emission efficiency is a reduction in the number of non-radiative recombination centres through physical confinement of the carriers. Lastly, the reduction of the effective refractive index of the material increases the extraction efficiency via refractive index matching. [That is, Fresnel reflection of light at normal incidence to a material/air interface can be written as $R = \frac{(n-1)^2}{(n+1)^2}$, which gives R < 4 % for SiO_2 ($n = 1.45$) and R > 30 % for Si ($n = 3.5$).][15]

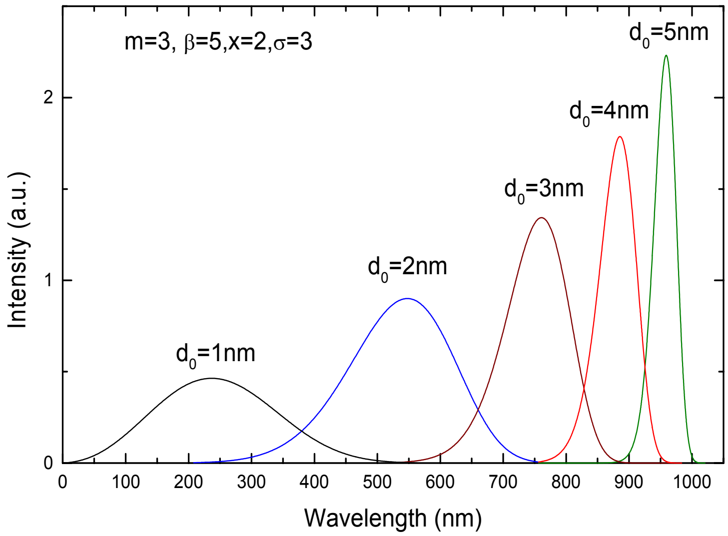

Figure 1-3: Theoretical spherical nanocrystal luminescence spectra based on Ranjan *et al.* model[14] showing its dependence on nanocrystal size (mean diameter), assuming a Gaussian size distribution ($\sigma = 3$).

Non-radiative recombination centres quench the luminescence emission from Si nanocrystals.[9] It is well known, however, that these defects can be passivated by annealing in a hydrogen-rich ambient, a process that can increase the luminescence intensity by as much as an order of magnitude.[16-19] It has also been demonstrated that passivation leads to a red-shift in the luminescence emission when samples contain a broad nanocrystal size distribution. It has been speculated that this results from a disproportionate increase in the emission from larger nanocrystals due to the fact that these are more likely to contain defects.[20] However, the precise mechanism remains unclear. Thus in this thesis, hydrogen passivation and desorption kinetics over a broad temperature range are used to systematically determine the relative concentration of trapped H in order to resolve the passivation mechanism.

Optical absorption in composite materials containing crystallites small compared to the wavelength of light are generally well described by electrostatic considerations which result in effective medium theories such as that due to Maxwell-Garnett or Bruggeman.[21] However, significant departures from such theories have been reported for porous silicon when the crystallite size is reduced below a critical value.[10] This is believed to be a direct consequence of quantum confinement effects that results in a reduction in the density of states and their shift to higher energies. Absorption spectra can therefore provide valuable information about the evolution of the electronic structure of nanocrystals as a function of their size, as well as provide essential data for quantitative modeling of luminescence. Photothermal deflection spectroscopy and conventional optical absorption spectroscopy were used to study such effects in this thesis.

An observation of major significance for potential device applications is the fact that energy transfer between silicon nanocrystals and rare-earth ions, such as Er, is extremely efficient.[22] In a material where both Si nanocrystals and Er ions are present, the photoexcited exciton is preferentially transferred from the Si nanocrystals to the Er ions, which release it radiatively. As such, nanocrystals act as very effective sensitizers for rare-earth excitation and because they have broad-band absorption cross-sections that are 10^2 - 10^4 times greater than isolated rare-earth ions can increase the luminescence emission from such ions by the same order.[23] Moreover, non-radiative de-excitation processes present in bulk Si, such as Auger relaxation or energy back-transfer, are strongly reduced, further improving the luminescence efficiency.[1] This provides the basis for fabricating a rare-earth optical amplifier that can be pumped with a broad-band source rather than a resonantly tuned laser, a feature that also raises the possibility of a multi-wavelength amplifier in which several rare-earth elements are simultaneously excited by the same nanocrystals. Recent reports have shown that amorphous Si nanoclusters can also act as sensitizers for Er.[24] A chapter of this thesis investigates the effect of hydrogen passivation on the interaction between Si nanoclusters/nanocrystals and Er.

1.3 Thesis Structure

The experimental techniques used in this work are briefly discussed in Chapter 2. Chapters 3 to 7 are related but self-contained research studies. Each of these chapters include more specific experimental details. Chapter 3 studies the electronic structure of Si nanocrystals through optical absorption measurements. Chapters 4 to 7 are concerned predominantly with light emission from Si nanocrystals and their interaction with defects and impurities. More specifically, Chapter 4 investigates the effect of annealing environment (Ar, N_2, forming gas) on the photoluminescence of Si nanocrystals; Chapters 5 and 6 deal with the passivation of non-radiative recombination centers with molecular and atomic hydrogen; and Chapter 7 explores the energy interaction between Si nanocrystals and Er^{3+} rare earth ions. Chapter 8 summarizes the conclusions of this thesis, and discusses possible directions for future work.

1.4 References

[1] L. Pavesi, J. Phys.: Condens. Matter **15**, R1169 (2003).

[2] International Technology Roadmap for Semiconductors, http://public.itrs.net (2004).

[3] G. Masini, L. Colace, and G. Assanto, Mat. Sci. Eng. B **89**, 2 (2002).

[4] P. Bettotti, M. Cazzanelli, L. Dal Negro, et al., J. Phys.: Condens. Matter **14**, 8253 (2002).

[5] M. A. Green, J. Zhao, A. Wang, et al., Nature **412**, 805 (2001).

[6] B. Gelloz and N. Koshida, J. Appl. Phys. **88** (2000).

[7] L. Pavesi, L. Dal Negro, C. Mazzoleni, et al., Nature **408** (2000).

[8] L. T. Canham, Appl. Phys. Lett. **57**, 1046 (1990).

[9] C. Delerue, G. Allan, and M. Lannoo, Phys. Rev. B **48**, 11024 (1993).

[10] D. Kovalev, Phys. Stat. Sol. B **215**, 871 (1999).

[11] J. D. Holmes, K. J. Ziegler, R. C. Doty, et al., J. Am. Chem. Soc. **123**, 3743 (2001).

[12] H. Takagi, H. Ogawa, Y. Yamazaki, et al., Appl. Phys. Lett. **56**, 2379 (1990).

[13] M. L. Brongersma, (Ph.D. Thesis, FOM-Institute for Atomic and Molecular Physics, 1998).

[14] V. Ranjan, V. Singh, and G. John, Phys. Rev. B **58**, 1158 (1998).

[15] E. Hecht, *Optics* (Addison-Wesley, San Francisco, 2002).

[16] S. P. Withrow, C. W. White, A. Meldrum, et al., J. Appl. Phys. **86**, 396 (1999).

[17] K. S. Min, K. V. Shcheglov, C. M. Yang, et al., Appl. Phys. Lett. **69**, 2033 (1996).

[18] S. Cheylan and R. G. Elliman, Appl. Phys. Lett. **78**, 1225 (2001).

[19] E. Neufield, S. Wang, R. Apetz, et al., Thin Solid Films **294**, 238 (1997).

[20] S. Cheylan and R. G. Elliman, Appl. Phys. Lett. **78**, 1912 (2001).

[21] C. F. Bohren and D. R. Huffman, *Absorption and scattering of light by small particles* (Wiley, New York, 1983).

[22] A. Polman, J. Appl. Phys. **82**, 1 (1997).

[23] F. Priolo, G. Franzò, D. Pacifici, et al., J. Appl. Phys. **89**, 264 (2001).

[24] G. Franzò, S. Boninelli, D. Pacifici, et al., Appl. Phys. Lett. **82**, 3871 (2003).

CHAPTER

2

Experimental

2.1 Sample Preparation Methodology

Si nanocrystals can be formed through a variety of methods including laser ablation,[1] molecular beam epitaxy,[2] gas evaporation,[3] ion implantation,[4] chemical vapour deposition[5] and cosputtering.[6] These methods generally rely on the supersaturation of a SiO_2 film with excess Si atoms and a subsequent high-temperature anneal to precipitate the Si into nanocrystals. This is a good approach, as silica films offer a robust material for potential devices applications and additionally provide surface passivation for the nanocrystals.

Ion-implantation and high temperature annealing were employed for nanocrystal synthesis throughout the current study. The use of thermal oxides and ion implantation at keV energies, as used here, are standard for semiconductor device technology. Ion implantation also provides accurate control over the excess-Si depth distribution by the choice of acceleration energy and ion fluence.[7, 8] However, the stochastic nature of the ion stopping process results in an approximately Gaussian Si distribution, which in turn results in a broad size distribution of nanocrystals (see Figure 2-1). This is because the nucleation and growth of nanocrystals is strongly dependent on the local degree of supersaturation. The mean nanocrystal size is therefore depth dependent, with smaller nanocrystals formed at the concentration tails. Nevertheless, this synthesis method provides a simple and flexible approach to nanocrystal synthesis and is well suited to experimental investigations of nanocrystals and their properties.

Following implantation, the silicon-rich SiO_2 was annealed at temperatures above 900 °C to form Si nanocrystals. The annealing temperature routinely used was 1100 °C. For ion implanted nanocrystals this temperature is widely used as a standard anneal as it gives maximum light emission within the practical limits of Si processing.[9] However, different temperatures and durations were also investigated as the size distribution and quality of passivation depends on these factors.[10]

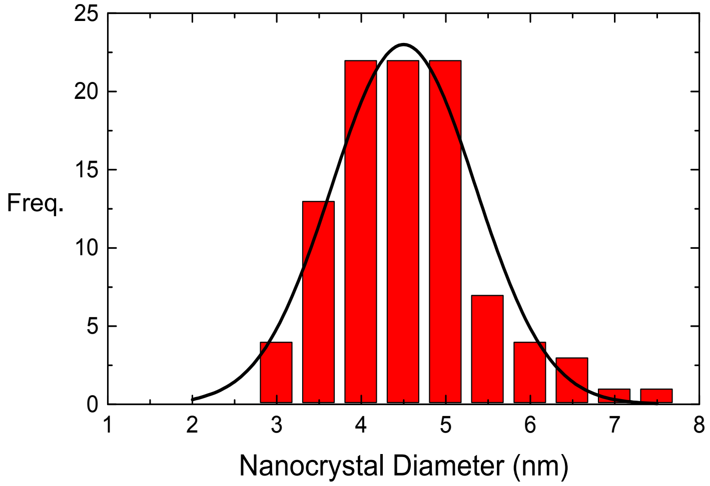

Figure 2-1: Typical nanocrystal size distribution (from TEM). Implant: 100 keV, 8×10^{16} Si/cm^2.

To improve the photoluminescence (PL) efficiency by reducing non-radiative recombination, hydrogen passivation was performed by thermally annealing the samples in forming gas (5 % H_2 in N_2) or through the *alneal* process. The former process supplies molecular hydrogen and the latter supplies atomic hydrogen. The *alneal* is simply a post metallization anneal (PMA) in which Al is evaporated onto the surface of the sample prior to furnace annealing[11] (this is described in §2.2.3).

The effect of Er-doping was investigated with Er introduced into Si-rich thermal SiO_2 samples through ion implantation. The samples were co-implanted with both Si and Er before any heat treatment to precipitate the nanocrystals. After implantation, the samples were annealed at a range of temperatures (800 - 1100 °C) to form the nanocrystals and to optically activate the Er.

The samples were characterized predominantly through room-temperature PL and time-resolved PL (TRPL). However, other techniques including optical absorption (OA) spectroscopy, photothermal deflection spectroscopy (PDS), Raman spectroscopy and transmission electron microscopy (TEM) were also used. The specific details of the experimental methods and apparatus are outlined below.

2.1.1 Ion Implantation

As mentioned above, the nanocrystals investigated in this thesis were synthesized by ion implantation. All ion implantation experiments were carried out with either the ANU 175 kV ion implanter or the ANU 1.7 MV tandem accelerator (National Electrostatics Corporation, USA, 5SDH-4). A schematic diagram of the 5SDH-4 is shown in Figure 2-2. The accelerator is equipped with a SNICS (source of negative ions by caesium sputtering) ion source, which can produce a large variety of negative ion beams from solid cathode targets. In this source, Cs vapor produced in an oven enters an enclosed area between the cooled cathode and the heated ionizing surface. Some Cs condenses on the cathode and some is thermally ionized by the ionizer. The ionized Cs, now positively charged, is then accelerated towards the negatively biased cathode, sputtering particles from the cathode through a condensed Cs layer. Besides sputtering, the Cs enhances the negative ion formation by lowering the work function of the cathode surface. (In this work, pressed powders of Si and Er_2O_3 were used for Si and Er implantations, respectively.)

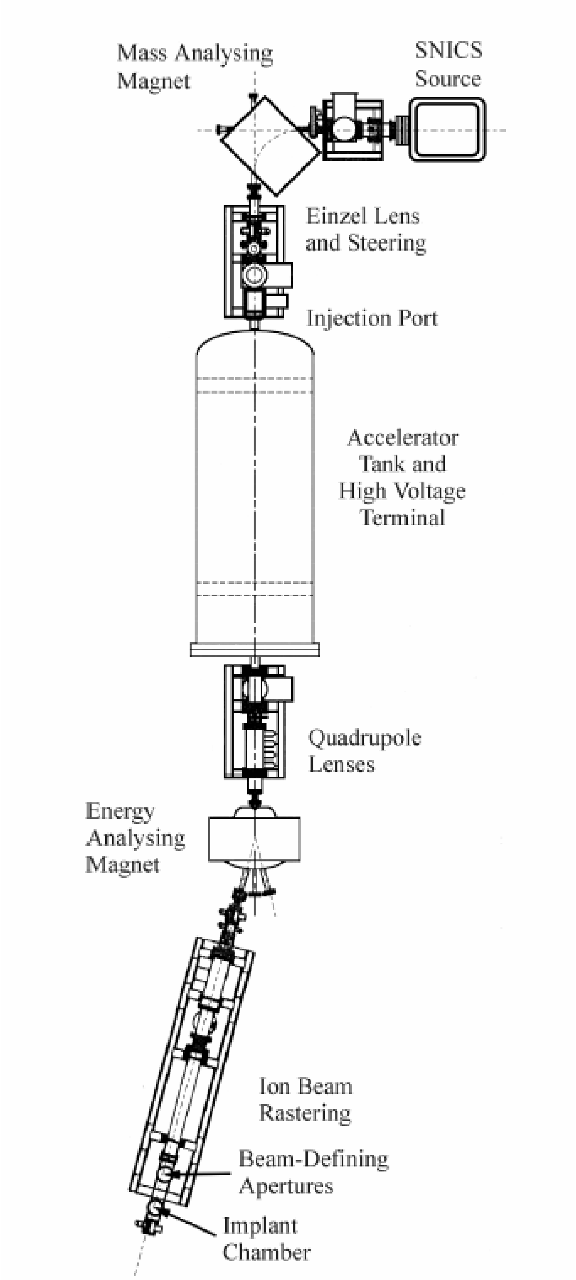

Figure 2-2: ANU 1.7 MV tandem accelerator (NEC 5SDH-4).

The sputtered ions are extracted through the centre of the ionizer, focused, and accelerated before mass selection with a 90° magnet. The beam is then focused and steered before injection into the high-voltage accelerator. This accelerator is a tandem accelerator of the Pelletron design. Inside the tank, the negatively charged beam is accelerated towards the positively charged terminal. At the terminal, a fraction of the negative ions are converted to positive ions by passing them through a nitrogen charge-exchange cell. The resulting positive ions are then accelerated away from the terminal towards the ground potential at the exit of the tank. The beam is then filtered with a 15° switching magnet, focused and steered. Finally, the beam is electrostatically rastered across a Ta aperture in front of the sample. The ion fluence is determined from the projected aperture area and the integrated ion charge with an uncertainty of ± 5 %. All implantations were performed at room-temperature. A cold shield (liquid-nitrogen cooled) was used to reduce sample surface contamination.

The principle and operation of the 175 kV ion implanter are similar to the injection stage of the 5SDH-4 accelerator, as shown in Figure 2-3.

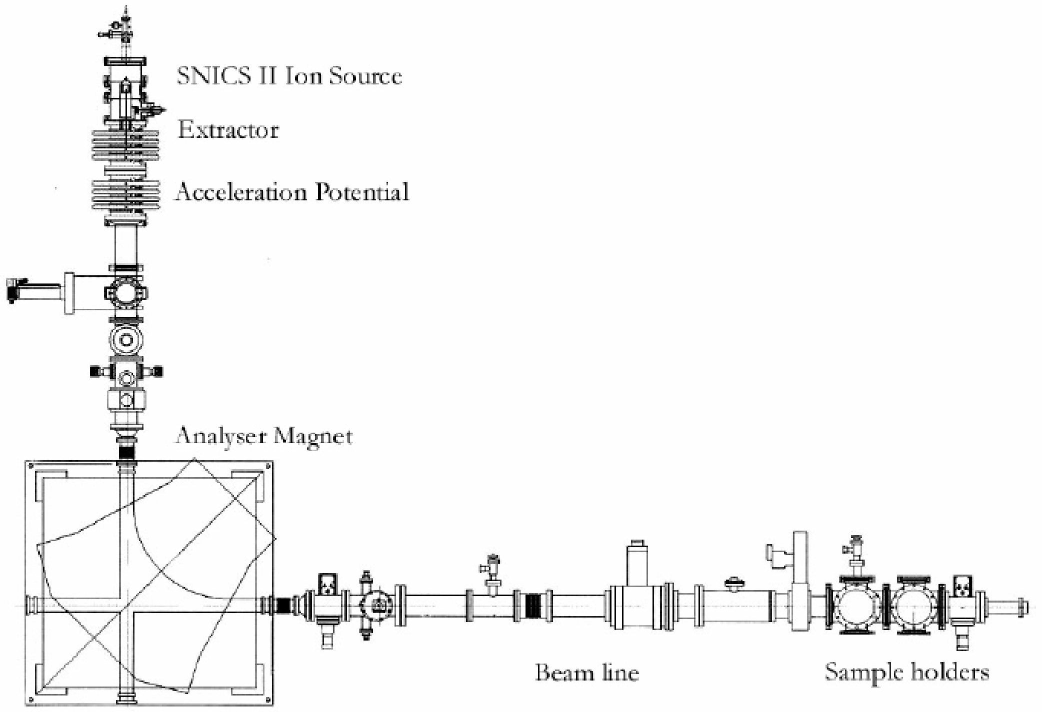

Figure 2-3: ANU 175 kV ion implanter.

The concentration depth profiles of the implanted ion species were calculated using Stopping and Range of Ions in Matter (SRIM) Monte-Carlo simulations.[8] SRIM uses a kinematic treatment of ion-atom collisions and semi-empirical electronic stopping data to calculate both the final distribution of the ions and also all kinetic phenomena associated with the ions' energy loss. This allows simulations of target damage and sputtering to be performed. [Note: SRIM 2000.39 was used for most calculations].

2.1.2 Thermal Annealing

In this work, thermal annealing was used to precipitate the excess Si into nanocrystals, to remove damage caused by ion implantation, for activation of erbium and for hydrogen passivation experiments. An appropriate combination of time and temperature is needed for each of these situations. Thermal annealing was carried out in either a rapid thermal annealing (RTA) system (AET-ADDAX RX) or in a conventional horizontal single-zone quartz-tube furnace (Lindberg 1500 °C) under flowing Ar, N_2 or forming gas (5 % H_2 in N_2). The gas was passed through a moisture filter before entering the furnace.

2.2 Sample Details

Detailed descriptions of the samples are shown here. However, each chapter also includes brief details of the samples used, for convenience.

2.2.1 Optical Absorption

Fused silica glass slides (GE 124) were used as the sample substrate for optical absorption measurements. These were implanted with Si^+ ions at 400 keV at fluences of 0.6, 1, 2, 3, 4, and 6 $\times 10^{17}$ cm^{-2}, using the 1.7 MV implanter. From SRIM simulations, this range corresponds to concentrations in the range from 2.5 to 25 at. % peak Si excess. This large range was chosen to encompass both dilute and non-dilute ripening.[9] The simulations also predict a projected range and straggle of 630 nm and 140 nm, respectively. The optical absorption was measured before and after annealing at 1100 °C for 1 hour in N_2.

2.2.2 Annealing Environment

Fused silica glass slides (GE 124) were used as the sample substrate for the annealing environment study. These were implanted with Si^- ions at 100 keV at a fluence of 8×10^{16} cm^{-2}, using the 175 kV implanter. This corresponds to a Si excess of approximately 10 at. % at the projected range of 150 nm. This Si excess is known to give strong luminescence. The purpose of this study was to assess the effect of different annealing gases on nanocrystal formation and luminescence efficiency. The gases investigated were N_2, Ar, and forming gas (5% H_2 in N_2).

2.2.3 Hydrogen Passivation

The samples used for all hydrogen passivation studies were fabricated by implanting a 1.25 μm thermal oxide with 400 keV Si^+ ions to a fluence of 2×10^{17} cm^{-2}. The oxide was a wet thermal oxide grown at 1100 °C on (100) Cz 0.1-0.3 ohm cm B-doped silicon in the Department of Engineering at the ANU. After implantation, the samples were annealed at 1100 °C for 1 hour in either N_2 or Ar. Hydrogen passivation was achieved either by annealing in forming gas (5% H_2 in N_2) or through the *alneal* process. This process consists of thermally evaporating a thin layer (100 nm) of Al onto the oxide surface before annealing. Significant amounts of atomic hydrogen can be generated within an oxide layer if chemically active metals such as Al or Cr are deposited on the surface prior to annealing.[12] H is believed to be generated by the reaction of water vapor adsorbed at the SiO_2 surface with the deposited Al. In most cases, the water is in the form of hydroxyl groups strongly bound to surface silicon atoms.[13] The Al layer is subsequently removed with a hot (90 °C) H_3PO_4 etch.

2.2.4 Erbium Interaction

A 1.25 µm oxide layer on (100) Si was implanted with 100 keV Si^- ions to a fluence of 1×10^{17} cm^{-2} and then with 500 keV Er^+ to fluences of 1×10^{14} and 1×10^{15} cm^{-2}. The samples were subsequently annealed at 800, 900, 1000 or 1100 °C. The samples were analyzed before and after passivation at 500 °C for 1 hour in forming gas (5% H_2 in N_2).

2.3 Sample Characterization

The experimental techniques used in this work are ion implantation (II), photoluminescence (PL) and time-resolved PL (TRPL), optical absorption (OA), photothermal deflection spectroscopy (PDS), and Raman spectroscopy. This section contains a brief description of the basic physical principles of the techniques and specific features of the experimental systems used.

2.3.1 Photoluminescence

Photoluminescence (PL) is a powerful, non-destructive, technique for measuring the optical properties of a sample. PL is the spontaneous emission of light from a material under optical excitation. A laser beam is directed onto the sample and, if of sufficient energy, photons are absorbed and electronic excitations are created. Eventually these excitations relax and the electrons return to the ground state. The relaxation can occur radiatively, with the emission of a photon, or non-radiatively through Auger recombination or defect-related relaxation. PL measures the radiative recombination and as such is a sensitive probe of electronic states.[14]

A schematic diagram of the PL system employed in the present study is shown in Figure 2-4. The system uses either an Ar^+ laser at 488 nm (2.54 eV) or a diode-pumped solid state laser at

532 nm (2.33 eV) as the excitation source. The laser is focused onto the sample with emitted light collected and focused with two quartz f/4 plano-convex lenses onto the entrance slits of the spectrometer (TRIAX 320). This symmetric lens geometry is used to reduce chromatic aberration. The samples are held at a fixed angle and distance from the collection optics so that relative intensity measurements can be made. The entrance slit is typically at 0.1 mm for spectral analysis. The grating for routine nanocrystal measurements has a groove density 150 g/mm and allows a spectral region of about 500 nm width (generally, 500 - 1000 nm) to be collected on the charge-coupled device (CCD) array at a fixed grating angle. The PL is measured using a liquid-nitrogen cooled Si CCD array (EEV CCD30-11). The response of the system was corrected using a black-body calibration source. A secondary exit port on the spectrometer allows the use of a range of detectors for specialist applications. For erbium measurements (1.5 μm emission), either a Peltier-cooled InGaAs photodiode (EOS IGA-020-TE2) or a liquid-nitrogen cooled Ge detector (ADC) was used. Standard lock-in amplifier techniques were used with the Ge detector.

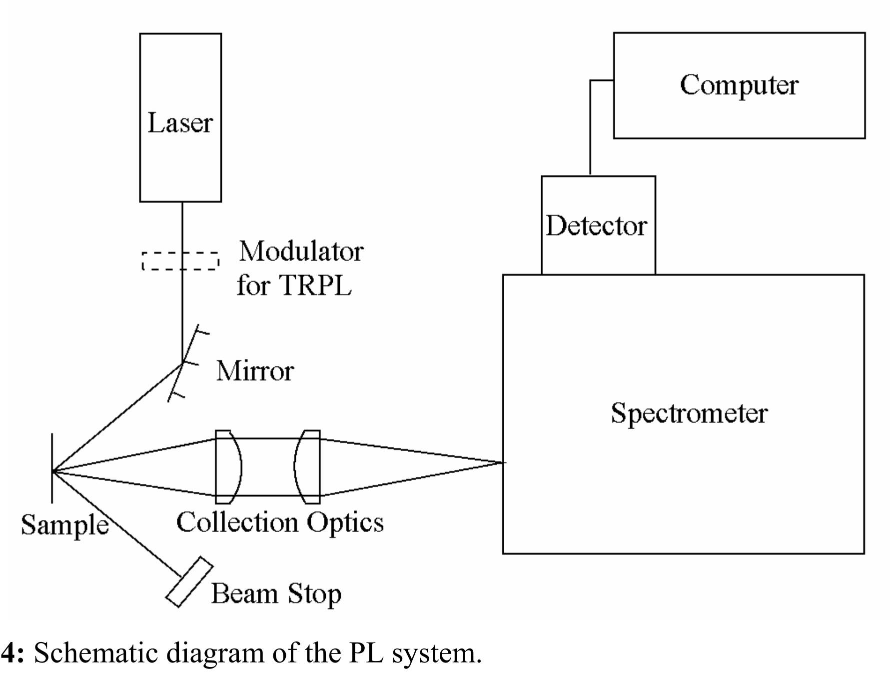

Figure 2-4: Schematic diagram of the PL system.

2.3.2 Time-Resolved Photoluminescence

Time-resolved PL (TRPL) was used to extract PL rise and decay lifetimes. For nanocrystal luminescence (typical lifetimes of 10 to 100 μs), a Brimrose TEM-85-10 acousto-optic modulator (AOM) (see Figure 2-4) was used to modulate the laser excitation source and the PL was detected with a room-temperature photomultiplier (Hamamatsu R928). The time resolution of this system was better than 1 μs. For erbium measurements (typical lifetimes of 1 to 10 ms), a mechanical chopper was used and PL detected with a liquid-nitrogen cooled Ge detector. The time resolution of this system was approximately 0.2 ms. The detector output was stored on a digital storage oscilloscope and averaged over 128 periods to improve the signal-to-noise ratio. The excitation source was either 488 nm or 532 nm.

2.3.3 Optical Absorption Spectroscopy

Optical absorption spectroscopy was used to study the optical absorption characteristics of the nanocrystals. These characteristics included such quantities as absorption coefficient, band gap energy and effects due to Mie extinction. A Shimadzu UV-3101PC UV-VIS-NIR scanning spectrophotometer was used in transmission mode over the wavelength range 200 to 3200 nm. The reference cell was left empty, with the background and substrate material measured separately and included in the analysis.

2.3.4 Photothermal Deflection Spectroscopy

Photothermal deflection spectroscopy (PDS) is a very sensitive technique introduced by Boccara *et al*. in 1979.[15] The underlying principle of PDS is the deflection of a light beam as it travels through a refractive index gradient created by a temperature gradient in a medium. Because this technique indirectly measures optical absorption, it significantly reduces artifacts due to interference effects present in standard optical absorption spectroscopy.[16, 17] Moreover, scattering and reflection losses do not produce photothermal signals.[18]

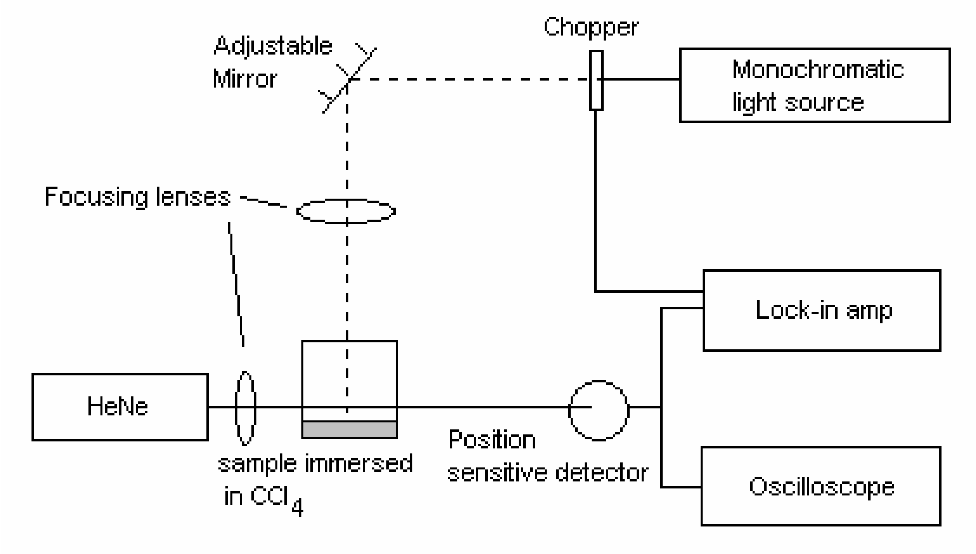

Figure 2-5: Schematic diagram of the PDS system.

With PDS, the absorbance was measured over the wavelength range 400 – 1600 nm. The sample is placed in a glass-windowed stainless steel cell and immersed in a suitable liquid, in this case CCl_4. The sample is then irradiated with chopped (18 Hz) monochromatic light. Absorption in the sample causes a periodic local heating in the sample. A probe laser beam (He-Ne), parallel to the sample surface (the so-called transverse PDS configuration), is used to measure the thermally induced refractive index change of the liquid (for CCl_4 $\frac{dn}{dT} \sim -0.271$)[17] in the vicinity of the sample surface. For these experimental conditions, the beam deflection was taken to be proportional to the temperature change. The raw PDS spectra were matched with the spectra obtained by transmission measurements over the range 600 to 800 nm. Full field calculations show that the PDS measurements are insensitive to interference effects for the sample configurations employed in the present work.[17]

2.3.5 Raman Spectroscopy

Raman spectroscopy is nondestructive and widely used to study the vibrational and structural properties of single crystals.[19] In this work, Raman was employed in an attempt to gain information on the nanocrystal size distribution. Laser Raman spectra were recorded on a DILOR Super Labram spectrometer equipped with a holographic notch filter, 600 and 1800 g/mm gratings, and a liquid-nitrogen cooled charge-coupled device (CCD) array detector. The samples were illuminated with the 514.5 nm (2.41 eV) line of an Ar^+ laser with an Olympus 100× microscope objective used to focus the laser beam and collect the scattered light. This system is located at Geoscience Australia.

2.4 References

[1] E. Werwa, A. A. Seraphin, L. A. Chiu, et al., Appl. Phys. Lett. **64**, 1821 (1994).

[2] Z. H. Lu, D. F. Lockwood, and J.-M. Baribeau, Nature **378**, 258 (1995).

[3] S. Hayashi, S. Tanimoto, and K. Yamamoto, J. Appl. Phys. **68**, 5300 (1990).

[4] T. Shimizu-Iwayama, S. Nakao, and K. Saitoh, Appl. Phys. Lett. **65**, 1814 (1994).

[5] H. Takagi, H. Ogawa, Y. Yamazaki, et al., Appl. Phys. Lett. **56**, 2379 (1990).

[6] S. Furukawa and T. Miyasato, Phys. Rev. B **38**, 5726 (1988).

[7] D. Stievenard and J. C. Bourgoin, *Ion implantation in semiconductors* (Trans Tech Publications, Zurich, 1988).

[8] J. F. Ziegler, J. P. Biersack, and U. Littmark, *The Stopping and Range of Ions in Solids* (Paragon Press, New York, 1985).

[9] C. Bonafos, B. Colombeau, A. Altibelli, et al., Nucl. Instr. Meth. Phys. Res. B **178**, 17 (2001).

[10] M. Lopez, B. Garrido, C. Bonafos, et al., Nucl. Instr. and Meth. B **178**, 89 (2001).

[11] A. R. Wilkinson and R. G. Elliman, Appl. Phys. Lett. **83**, 5512 (2003).

[12] R. F. Pierret, *Field effect devices* (Addison-Wesley, 1990).

[13] M. L. Reed and J. D. Plummer, J. Appl. Phys. **63**, 5776 (1988).

[14] T. H. Gfroerer, in *Encyclopedia of Analytical Chemistry*, edited by R. A. Meyers (Wiley, Chichester, 2000).

[15] A. C. Boccara, D. Fournier, and J. Badoz, Appl. Phys. Lett. **36**, 130 (1979).

[16] W. B. Jackson, N. M. Amer, A. C. Boccara, et al., Appl. Opt. **20**, 1333 (1981).

[17] R. G. Elliman, M. J. Lederer, and B. Luther-Davies, Appl. Phys. Lett. **80**, 1325 (2002).

[18] S. E. Bialkowski, *Photothermal Spectroscopy Methods for Chemical Analysis* (Wiley, New York, 1996).

[19] P. M. Fauchet and I. H. Campbell, Crit. Rev. Solid State Mater. Sci. **14**, S79 (1988).

CHAPTER

3

Electronic Structure of Si Nanocrystals in SiO_2

In this chapter, the electronic structure of silicon-implanted silica slides is investigated through optical absorption measurements. Silica samples were implanted with 400 keV Si^+ ions to six fluences in the range 0.6 – 6×10^{17} cm^{-2} and annealed at 1100 °C for 1 hour to form Si nanocrystals. Before and after annealing, optical absorption spectra from these samples (measured over the wavelength range of 200 to 3200 nm) show considerable structure that is characteristic of the particular implant fluence. This structure is shown to correlate with the transmittance of the samples as calculated from the modified refractive index profile for each implant. Due to the high absorption coefficient of Si at short wavelengths, extinction at these wavelengths is found to be dominated by absorption, with the effect of scattering being insignificant. To eliminate interference effects, a little-known but established technique known as photothermal deflection spectroscopy is used to obtain data on the band structure of Si in these samples (measured over the wavelength range of 400 to 1600 nm). This data shows little variance from bulk Si structure and thus little effect of quantum confinement. This is attributed to the dominance of large nanocrystals in absorption measurements, due to the broad size distribution of nanocrystals in the samples.

3.1 Introduction

Optical absorption provides critical data on the band structure of semiconductor nanocrystals.[1] However, such measurements are generally complicated by interference effects and scattering losses. These can distort Tauc plots and lead to erroneous band gap estimates for semiconductor nanocrystals.[2, 3] Awareness and understanding of these complications is essential for extracting accurate data.

In this chapter, optical measurements are employed to study the electronic structure of Si nanocrystals and Si-rich SiO_2. This chapter also examines optical scattering and interference effects caused by the modified refractive index profile produced by implantation, by both experimental and theoretical means.

3.2 Theoretical Considerations

3.2.1 Dielectric Functions

To model the refractive index profile of Si-rich oxides, an average dielectric function must be computed using effective medium theory.[4] Two commonly employed models are those due to Maxwell-Garnett[2] and the Bruggeman.[1] Both of these functions have been shown to follow from the same integral equation from different approximations.[4] However, the Bruggeman dielectric function applies to a two-component mixture in which there are no distinguishable inclusions embedded in a definite matrix. In contrast to the Maxwell-Garnett, it does not strictly apply to a particulate medium because there is no way to decide which component constitutes the particles and which the surrounding medium. Therefore, the Bruggeman dielectric function is expected to better describe the dielectric function of as-implanted samples, whereas the Maxwell-Garnett function should better describe the annealed samples where well-defined clusters are present.

The average dielectric function (ε_{av}) derived by Maxwell-Garnett, if the inclusions are spherical, is as follows

$$\varepsilon_{av} = \varepsilon_m \left[1 + \frac{3f\left(\dfrac{\varepsilon - \varepsilon_m}{\varepsilon + 2\varepsilon_m}\right)}{1 - f\left(\dfrac{\varepsilon - \varepsilon_m}{\varepsilon + 2\varepsilon_m}\right)} \right], \qquad (1)$$

and that derived by Bruggeman is

$$f\frac{\varepsilon-\varepsilon_{av}}{\varepsilon+2\varepsilon_{av}}+(1-f)\frac{\varepsilon_m-\varepsilon_{av}}{\varepsilon_m+2\varepsilon_{av}}=0\,, \tag{2}$$

where ε and ε_m are the respective dielectric functions of inclusions and the otherwise homogenous medium. f is the volume fraction of the inclusions, which can be written as

$$f=x\left(x+(1-x)\frac{\rho_{Si}}{\rho_{SiO_2}}\right)^{-1}, \tag{3}$$

where x is the atomic excess of Si, and ρ_{Si} and ρ_{SiO_2} are the atomic densities of c-Si (~5×10^{22} cm^{-3}) and a-SiO_2 (~7×10^{22} cm^{-3}), respectively.

For convenience, the complex dielectric function ($\varepsilon=\varepsilon'+i\varepsilon''$) can be related to the complex refractive index ($N=n+ik$) through the simple relations

$$n=\sqrt{\frac{\sqrt{\varepsilon'^2+\varepsilon''^2}+\varepsilon'}{2}}\,, \tag{4}$$

and

$$k=\sqrt{\frac{\sqrt{\varepsilon'^2+\varepsilon''^2}-\varepsilon'}{2}} \tag{5}$$

for a nonmagnetic material.[4]

3.2.2 Thin-Film Matrix Method

The transmission of films with non-uniform refractive index profiles were calculated using the well-known thin-film matrix method.[5] In this scheme, the sample is divided into a number of layers. For each layer, a characteristic matrix (M) is computed. The characteristic matrix relates the fields at the two adjacent boundaries:

$$\begin{bmatrix} E_I \\ H_I \end{bmatrix} = \mathrm{M}_I \begin{bmatrix} E_{II} \\ H_{II} \end{bmatrix} = \begin{bmatrix} \cos k_0 h & i \sin k_0 h / \mathrm{Y}_1 \\ \mathrm{Y}_1 i \sin k_0 h & \cos k_0 h \end{bmatrix} \begin{bmatrix} E_{II} \\ H_{II} \end{bmatrix}, \qquad (6)$$

where k_0h is the phase shift ($\pi n_1 d / \lambda$) of the wave as it traverses the layer and $\mathrm{Y}_1 \equiv \sqrt{\frac{\varepsilon_0}{\mu_0}} n_1 \cos\theta_{iII}$.

In a system with p layers, electric and magnetic fields of the first and last boundaries are related by

$$\begin{bmatrix} E_I \\ H_I \end{bmatrix} = \mathrm{M}_I \mathrm{M}_{II} \cdots \mathrm{M}_p \begin{bmatrix} E_{(p+1)} \\ H_{(p+1)} \end{bmatrix} = \begin{bmatrix} m_{11} & m_{12} \\ m_{21} & m_{22} \end{bmatrix} \begin{bmatrix} E_{(p+1)} \\ H_{(p+1)} \end{bmatrix}. \qquad (7)$$

From this equation, the transmittance can be calculated from multiplying

$$t = \frac{2\mathrm{Y}_0}{\mathrm{Y}_0 m_{11} + \mathrm{Y}_0 \mathrm{Y}_s m_{12} + m_{21} + \mathrm{Y}_s m_{22}} \qquad (8)$$

by its complex conjugate, where $\mathrm{Y}_0 = \sqrt{\frac{\varepsilon_0}{\mu_0}} n_0 \cos\theta_{iI}$ and $\mathrm{Y}_s = \sqrt{\frac{\varepsilon_0}{\mu_0}} n_s \cos\theta_{iII}$. In this case, transmission measurements were performed at normal incidence ($\theta_{iI} = \theta_{iII} = 0$), and Y_0 and Y_s were for air and SiO_2, respectively.

3.2.3 Small Particle Effects

A particle placed in a beam of light will scatter some of the light incident on it and absorb some of it. The attenuation of the incident light is known as extinction. Mie theory describes the way in which spherical, homogenous particles interact with electromagnetic radiation. The absorption and scattering efficiencies of a small sphere (small compared with the wavelength) may be written as[4]

$$Q_{abs} = \left(\frac{8\pi a}{\lambda}\right) \mathrm{Im} \frac{\varepsilon - \varepsilon_m}{\varepsilon + 2\varepsilon_m}, \qquad (9)$$

$$Q_{sca} = \frac{8}{3}\left(\frac{2\pi a}{\lambda}\right)^4 \left|\frac{\varepsilon - \varepsilon_m}{\varepsilon + 2\varepsilon_m}\right|^2, \qquad (10)$$

where ε and ε_m are the permittivities of the sphere and the surrounding medium, respectively. The extinction efficiency is simply $Q_{ext} = Q_{abs} + Q_{sca}$, and the extinction cross-section for each sphere of radius a is $C_{ext} = Q_{ext} \pi a^2$. This quantity is proportional to the measured absorption (extinction) coefficient α, specifically

$$\alpha = nC_{ext} y, \qquad (11)$$

where n is the number of particles per unit volume and y is the optical path-length.

Freely available software called Mietab[6], based on this theory, was used to calculate the extinction cross-sections shown in §3.4.3.

3.3 Experimental Methods

3.3.1 Sample Preparation

Si nanocrystals were synthesized by ion implantation of Si^+ into 1 mm thick fused silica slides (GE 124). The samples were implanted at an energy of 400 keV to a range of fluences: 0.6, 1, 2, 3, 4, and 6 $\times 10^{17}$ cm^{-2}, at room temperature. Half of each sample was kept as an as-implanted reference; the other was annealed at 1100 °C in flowing high-purity N_2 for 1 hour in a conventional quartz-tube furnace. This is a standard thermal treatment used to produce luminescent nanocrystals, and remove implantation damage.

3.3.2 PL, PDS and Spectrophotometry

The optical properties of the samples were studied with photoluminescence (PL) measurements, photothermal deflection spectroscopy (PDS) and spectrophotometry.

Photoluminescence (PL) measurements were performed at room temperature, using the 488 nm line of an Ar^+ ion laser as the excitation source. Emitted light was analyzed using a single grating monochromator (TRIAX-320) and detected with a liquid-nitrogen cooled front-illuminated open-electrode CCD array (EEV CCD30-11).

Optical absorption was measured with PDS and spectrophotometry. A Shimadzu UV-3101 UV-VIS NIR scanning spectrophotometer was used in transmission mode to measure over the wavelength range 200 to 3200 nm. The reference cell was left empty, with the background and substrate material (GE 124) measured separately and included in the analysis. For PDS measurements, each sample was immersed in CCl_4 and a probe laser (He-Ne) used to measure the thermally induced (by monochromatic light) refractive index change of the liquid in the vicinity of the sample surface over the wavelength range 400 - 1600 nm. Using SRIM,[7] the distribution of the implanted Si layer was calculated to have a FWHM of approximately 300 nm. The relatively small thickness of this layer is advantageous for PDS, as it allows absorption coefficients up to the 10^4 cm^{-1} range to be measured whilst satisfying the requirement of good thermal uniformity throughout the absorbing layer.

3.4 Experimental Results

3.4.1 Photoluminescence

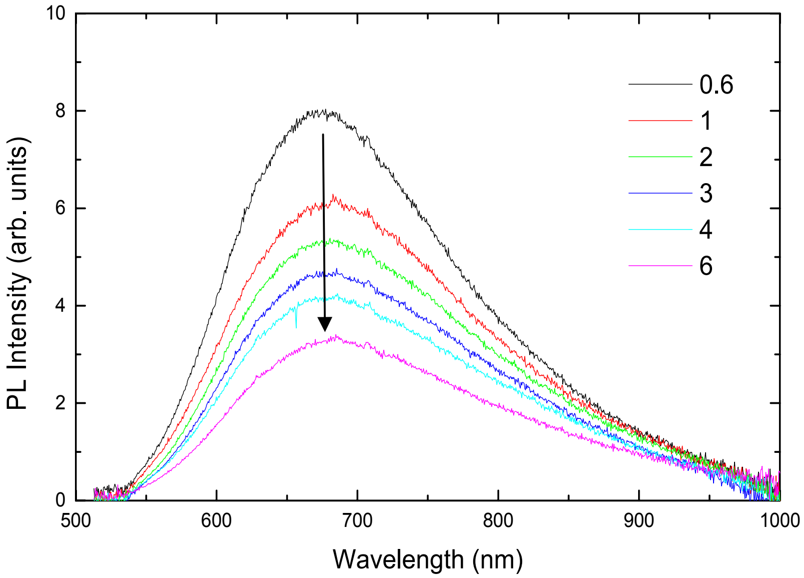

Figure 3-1: PL spectra of samples after 400 keV Si implantation. The implant fluence is indicated in units of 10^{17} cm^{-2}. The defect PL decreases with increasing fluence.

Figure 3-1 shows the PL spectra of the samples after ion implantation, for the range of fluences 0.6 – 6 $\times 10^{17}$ Si/cm^2. The PL measured here is due solely to defects created in the samples, as the formation of nanocrystals requires annealing at high temperature (> 900 °C). The observed PL band peaked at around 670 nm is commonly attributed to oxygen-deficient defects formed in SiO_2 by the implantation process. The decrease in PL intensity with increasing fluence is believed to result from the alteration of radiative defects to emit outside the detected wavelength range and/or the introduction of new competing non-radiative defects, by the subsequent irradiation.[8]

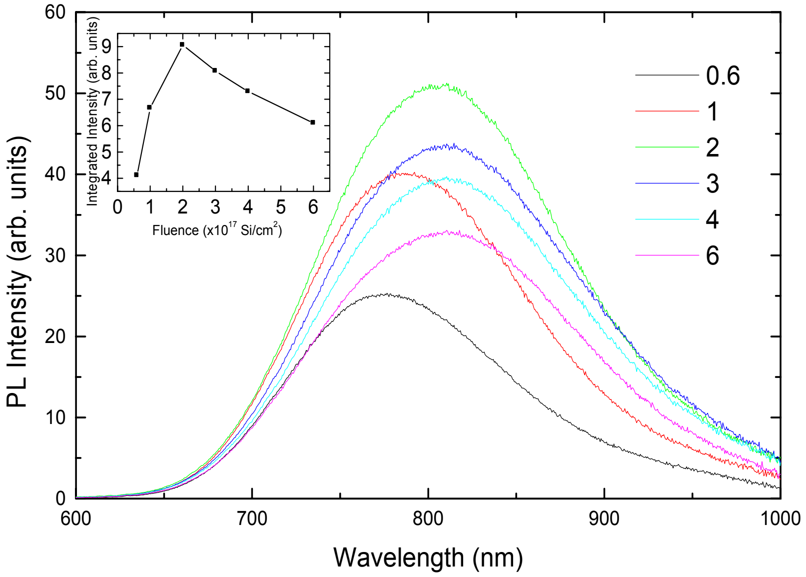

Figure 3-2: PL spectra of samples after 400 keV Si implantation and annealing at 1100 °C for 1 hour. The implant fluence is indicated in units of 10^{17} cm^{-2}. The inset shows the extracted integrated PL intensity versus implant fluence.

Figure 3-2 shows PL spectra after annealing at 1100 °C. This step is sufficient to form Si nanocrystals and the resulting PL spectra are characteristic of this. The PL intensity is highest for the fluence of 2×10^{17} Si/cm^2, which corresponds to approximately a 10 at. % Si peak excess. The PL intensity decreases for higher fluences. This is because at higher fluences the nanocrystal density and mean size increase.[9] Therefore, the interparticle spacing decreases giving rise to enhanced exciton migration between nanocrystals, the probability of larger nanocrystals containing defects also increases, and the oscillator strength decreases for larger nanocrystals. All of these effects are detrimental to radiative recombination. The first-listed effect is important because the probability for energy transfer between nanocrystals becomes more probable. For example, this can occur via dipole-dipole interactions (d^{-6}) or quantum tunneling. Since only a small fraction of Si nanocrystals is optically active due to defects, the exchange of excitons between crystals causes a reduction in emission intensity.

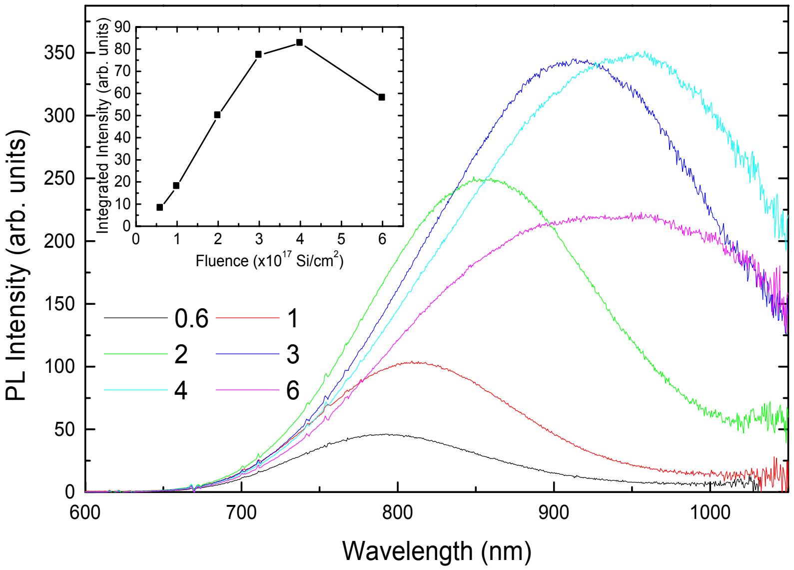

Figure 3-3: PL spectra of samples after 400 keV Si implantation, annealing at 1100 °C for 1 hour, and hydrogen passivation at 500 °C for 1 hour in forming gas. The implant fluence is indicated in units of 10^{17} cm^{-2}. The inset shows the extracted integrated PL intensity versus implant fluence.

Figure 3-3 shows the PL from nanocrystals after a standard passivation anneal (500 °C in 5 % H_2 in N_2 for 1 hour). As expected, the PL intensity of each sample is increased through passivation. This is due to the inactivation of non-radiative recombination centers (see Chapter 5). The fact that the peak intensity now occurs at a higher fluence (4×10^{17} Si/cm^2) than the unpassivated series supports the role of non-radiative defects in limiting PL emission.

Figure 3-4(a) shows the peak intensity position of the nanocrystal PL. Since the emission wavelength (energy) corresponds to the size of the nanocrystal (quantum confinement effect), a red-shift corresponds to an increase in the mean size of optically-active nanocrystals. Hydrogen passivation causes a red shift of the peak position for all fluences. This is caused by a disproportionate increase in the emission from larger nanocrystals after passivation. It has previously been attributed to the fact that larger nanocrystals have a larger surface area, and thus are more likely to contain defects.[10] It should be made clear that this measure is only surveying the optically active nanocrystals. The mean size of nanocrystals does not increase in size after passivation, but simply more of the larger nanocrystals (already present, but defective) are now emitting.

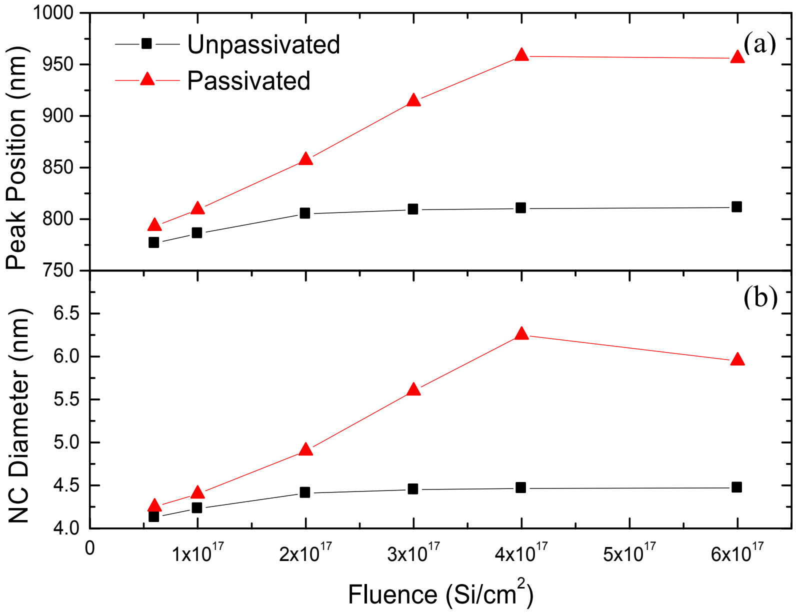

Figure 3-4: (a) Peak intensity wavelength and (b) corresponding 'effective' nanocrystal diameter calculated from data shown in Figure 3-2 and Figure 3-3.

In Figure 3-4(a), a red-shift of the peak position is seen with increasing fluence, before and after passivation. This agrees with previous work that report that larger nanocrystals are formed at higher fluences, under these annealing conditions.[9] A recent model predicts that the red-shift of the PL peak position corresponds to an increase from 4 to 6 nm in diameter with increasing fluence, after passivation and only a small change from 4 to 4.5 nm before passivation (see Figure 3-4(b)).[11] This size discrepancy is due to the fact that we are only surveying optically-active nanocrystals with PL. As stated above, hydrogen passivation at 500 °C does not affect the physical size distribution of the nanocrystals. Further support for this argument comes from transmittance measurements where hydrogen passivation was found to have no effect on the optical absorption spectra of Si nanocrystals (not shown).

3.4.2 Transmittance Measurements

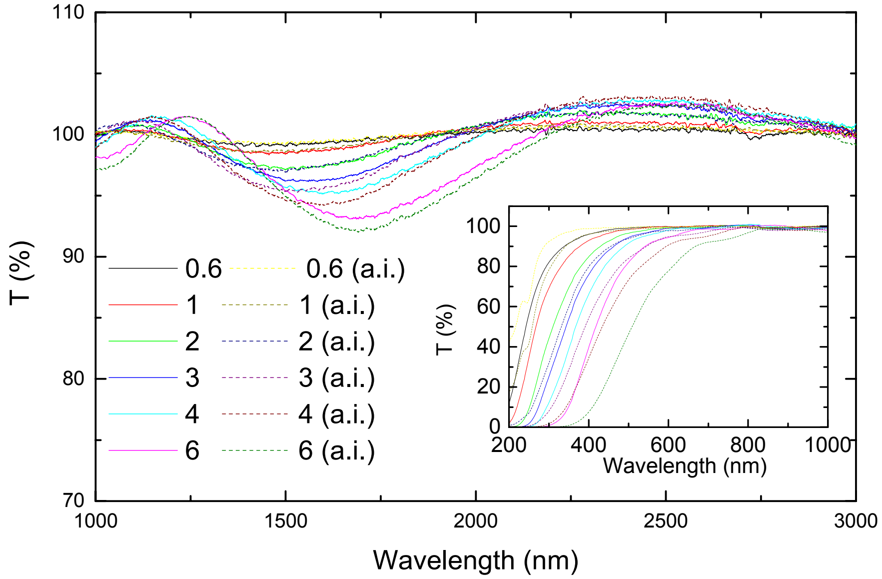

Figure 3-5: Transmittance spectra of samples before (as-implanted) and after annealing at 1100 °C for 1 hour. Inset shows short wavelength attenuation. The legend shows the implant fluences in 10^{17} Si/cm^2, with dashed lines referring to as-implanted samples.

Figure 3-5 shows the transmittance spectra of the samples before and after annealing at 1100 °C measured with a conventional spectrophotometer. The transmittance of the fused silica substrate has been subtracted, leaving only the contribution due to the inclusion of the Si excess. In each case, the measured transmittance exhibits a complex dependence on wavelength. It can be seen that annealing and thus the presence of Si nanocrystals has little effect on the shape of the spectra at longer wavelengths (these differences can be simulated by the appropriate choice of dielectric function, see Figure 3-8). The inset, on the other hand, shows the shorter wavelengths where more significant differences are observed. This could be attributed to scattering, as Mie scattering has a strong wavelength (λ^{-4}) and particle radius (a^6) dependence (see §3.2.3). Mie absorption on the other hand has a weaker wavelength (λ^{-1}) and particle radius (a^3) dependence. However, the absorption coefficient of Si in this region is high (see Figure 3-6(a)). Therefore, extinction may still be dominated by absorption rather than scattering.

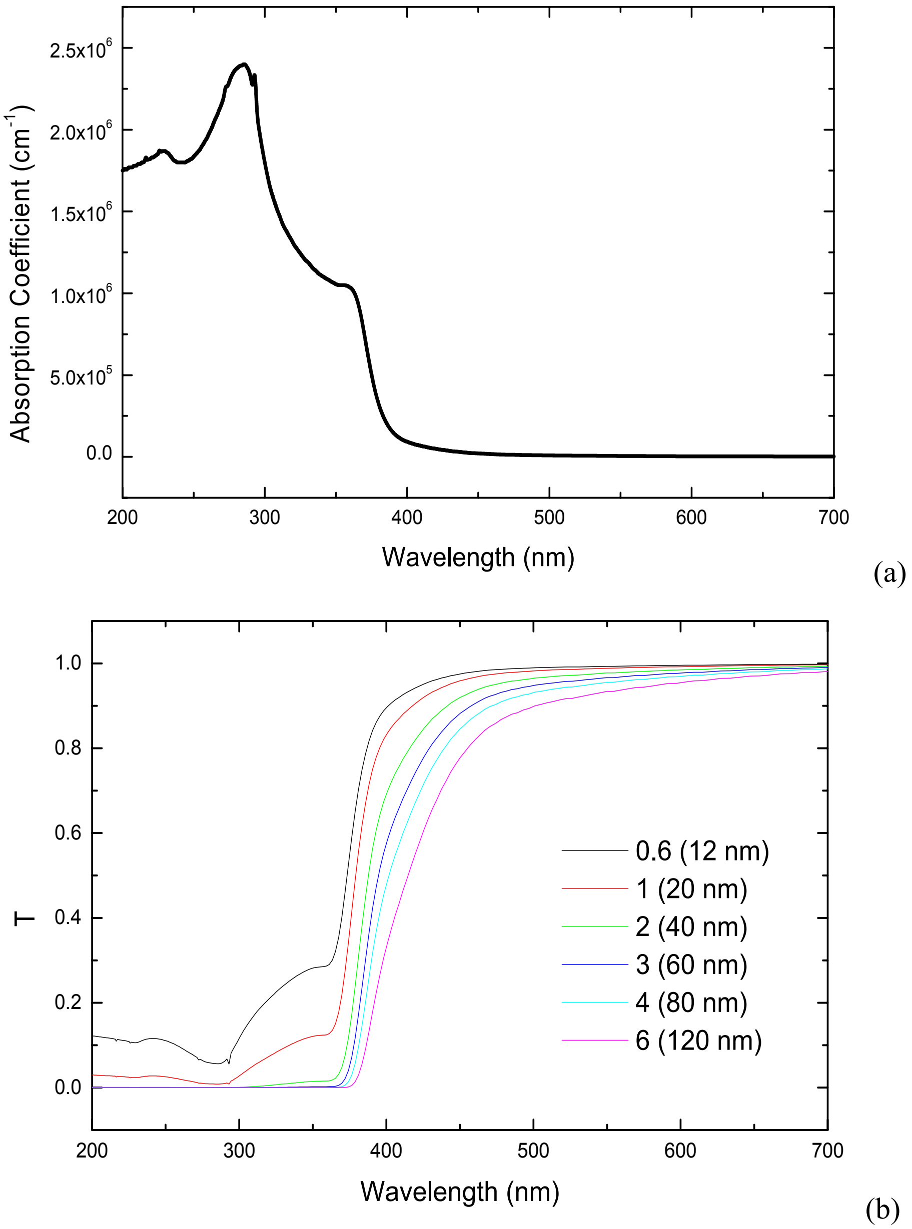

Figure 3-6: (a) Absorption coefficient of bulk Si in the short wavelength region.[12] Longer than 500 nm, absorption is insignificant. (b) Calculated transmittance based on equivalent thickness of Si. Implant fluence (×10^{17} Si/cm^2) is indicated on the graph along with the equivalent thickness used.

Figure 3-6(b) shows calculated transmittance ($T = e^{-\alpha \cdot t}$), solely based on the absorption coefficient (α) and the equivalent c-Si thickness (t) corresponding to each implantation fluence. This preliminary calculation illustrates that strong absorption of Si at short wavelengths is predicted (without taking scattering losses or interference effects into account). More complete calculations based on absorption of small particles are performed in

§3.4.3. However, the same qualitative conclusions are reached. [The Si thicknesses used are calculated from $t = \frac{\phi}{\rho_{Si}}$, where ϕ is the fluence and ρ_{Si} is the atomic density of Si (5×10^{22} cm^{-3}). For example, the highest fluence of 6×10^{17} cm^{-2} corresponds to a 120 nm thick slab of bulk Si.]

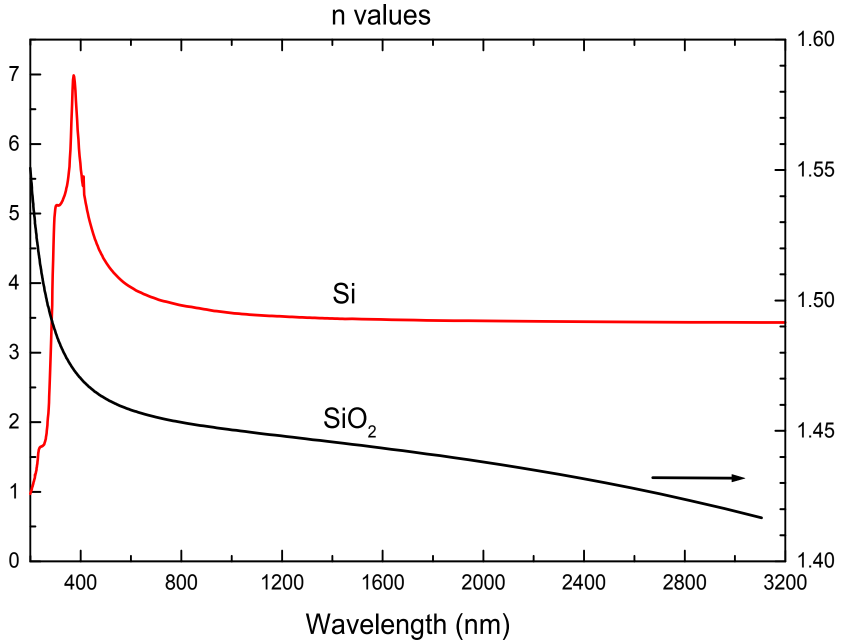

Figure 3-7: Refractive index (n) values for crystalline silicon[12] and amorphous SiO_2[13] used in simulations shown in Figure 3-8(b).

For simulating the interference effects on the transmittance, absorption was not taken into account. Figure 3-7(a) shows wavelength dependent refractive index (n) values used for the materials in the simulations. These values are used in the Maxwell-Garnett and Bruggeman dielectric functions, as well as the Mietab[6] calculations in §3.4.3 (absorption was included in Mie calculations).

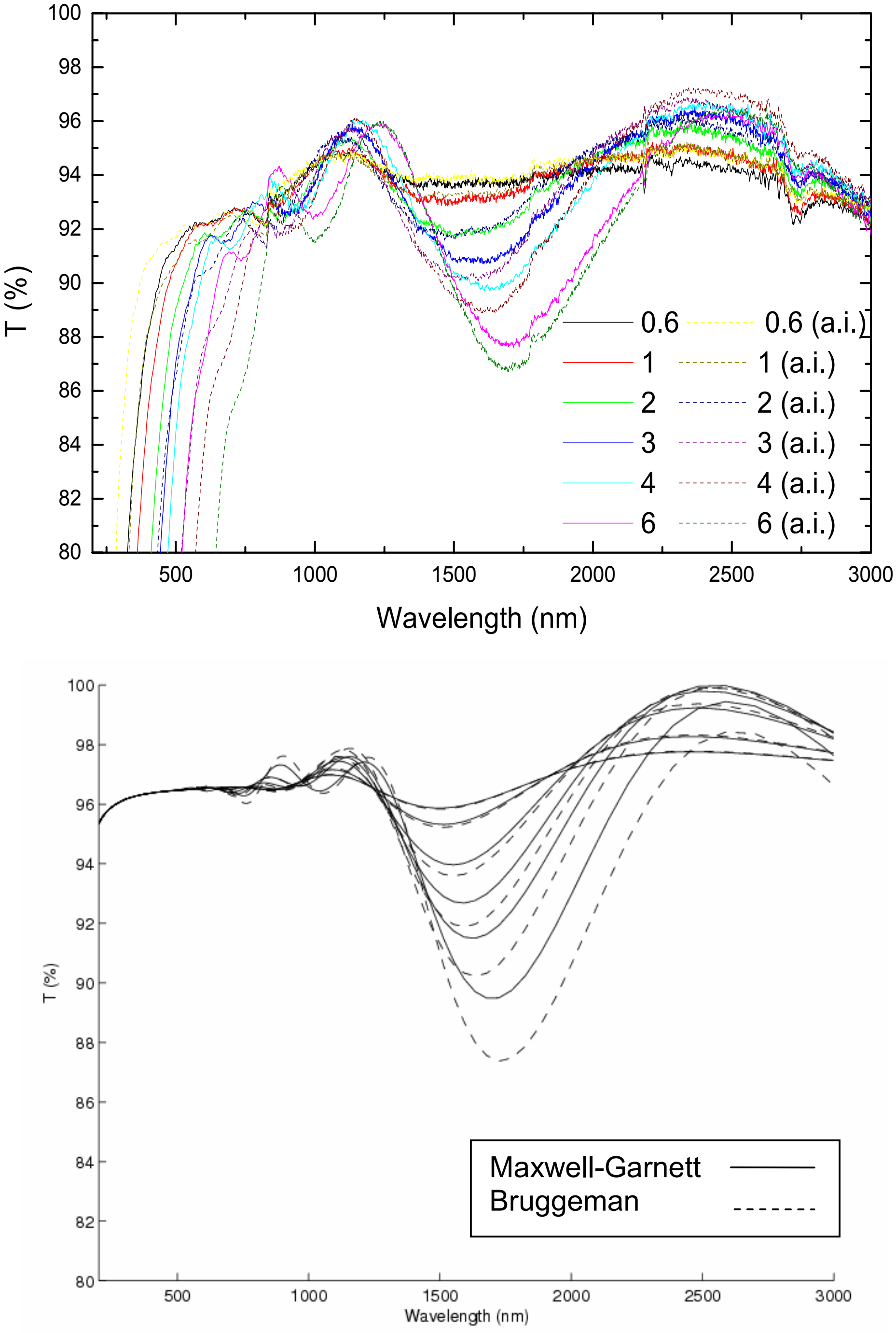

(a)

(b)

Figure 3-8: Comparison of (a) experimental and (b) theoretical transmittance spectra. (a) has data from samples before (as-implanted) and after annealing. (b) shows both the Maxwell-Garnett (solid) and Bruggeman (dashed) dielectric functions for the range of fluences ($\times 10^{17}$ Si/cm^2) shown in (a).

Figure 3-8(a) again shows the transmittance spectra presented in Figure 3-5, this time with the contribution due to the fused silica substrate included. Figure 3-8(b) shows simulations of these samples using a Gaussian implantation profile (with projected range and straggle from

SRIM 2000 simulations), the Maxwell-Garnett and Bruggeman dielectric functions and the matrix method using the refractive index values shown in Figure 3-7. Comparing the two figures, it can be seen that for wavelengths longer than 700 nm the experimental spectra are well reproduced by this model. The differences between the as-implanted and annealed samples can be reproduced by choosing the appropriate dielectric function. As expected, the Bruggeman function better describes the as-implanted samples, as it does not strictly apply to particulate medium, whereas the Maxwell-Garnett better describes the annealed samples. However, at wavelengths shorter than 700 nm, small particle scattering and absorption become significant and the model, which only considers interference effects, is inadequate. In the next section these additional effects are considered.

3.4.3 Small Particle Effects

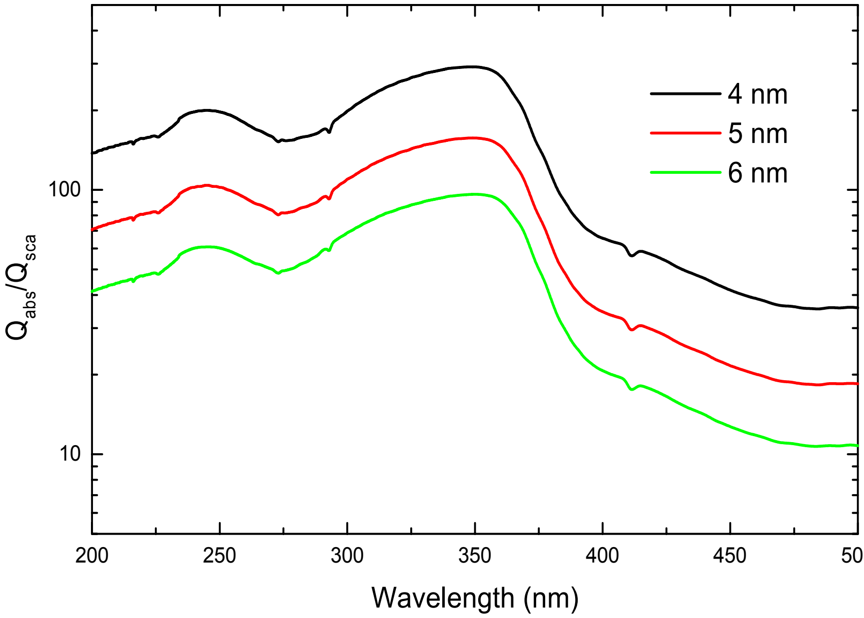

Figure 3-9: Ratio of calculated absorption cross-section over calculated scattering cross-section for spherical Si particles of 4, 5 and 6 nm diameters embedded in SiO_2.

As detailed earlier, the extinction efficiency is the sum of the absorption and scattering efficiencies. Figure 3-9 shows the ratio of the absorption cross-section over scattering efficiencies for spherical Si particles of 4, 5 and 6 nm diameters embedded in SiO_2 calculated according to Mie theory. [Modeling of PL spectra indicates that the mean sizes of the nanocrystals are in this size range (see Figure 3-4(b))]. This shows that for short wavelengths, absorption is the dominating contribution (1 to 2 orders of magnitude higher than scattering) to the extinction efficiency.

Figure 3-10 shows the extinction at short wavelengths measured by spectrophotometry and PDS, along with the extinction cross-section calculated from Mie theory for a range of Si particle diameters embedded in SiO_2. The samples shown here are after annealing has been performed to form nanocrystals. Because PDS measures absorption indirectly through a photothermal effect, it is insensitive to scattering and reflection losses.[14] The extinction measured with both techniques scales with implantation fluence since small particle absorption dominates the extinction in this wavelength range. Increasing the fluence has two effects: a larger amount of Si is present to absorb and scatter light; and the mean size of the nanocrystals is larger (see Figure 3-4(b)) and thus will have a bigger absorption and scattering cross-section (see Figure 3-10(c)).

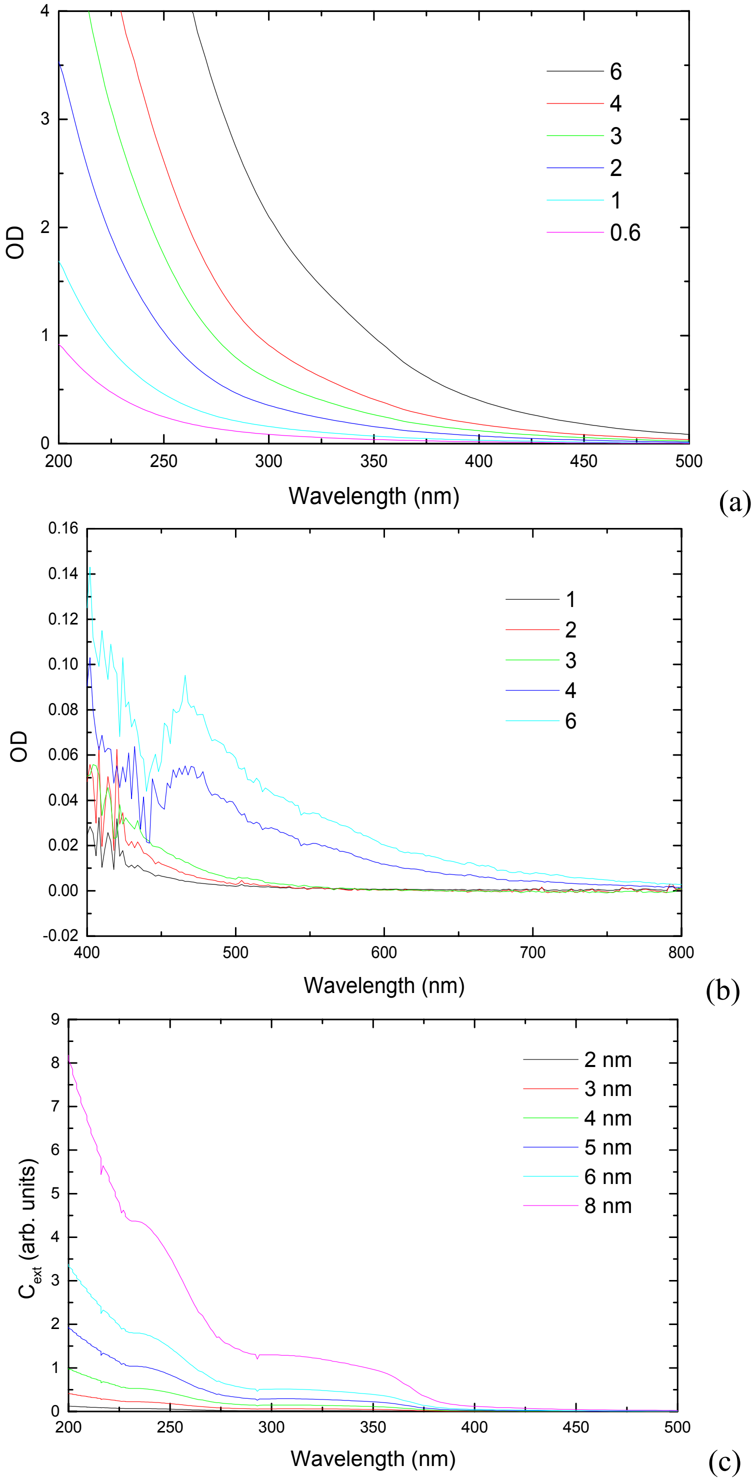

Figure 3-10: Extinction from (a) spectrophotometry (b) PDS, and (c) the calculated scattering and absorption according to Mie theory for different nanocrystal diameters. Absorption is the dominating contribution (see Figure 3-9). In (a) and (b) the implantation fluences are indicated in units of 10^{17} Si/cm^2. N.B. (b) is over a different wavelength range to (a) and (c).

3.4.4 Electronic Structure

A useful parameter for comparing nanocrystal composites is the Tauc optical gap. Amorphous and indirect semiconductors have often been analyzed with the Tauc relation:

$$(\alpha E)^{\gamma} = B(\hbar\omega - E_T) \qquad \textbf{(12)}$$

where α is the absorption coefficient, $\gamma = ½$, B is a constant, and E_T is the Tauc gap. Some authors have used this equation to determine E_T from the transmission spectra.[15] However, as above, wavelength-dependent interference and small particle effects complicate these spectra and must be accounted for.

3.4.4.1 Spectrophotometer

Figure 3-11 shows Tauc plots of the samples as well as that of bulk Si showing the indirect band gap of around 1.1 eV (x-axis intercept). In the case of the as-implanted material this is unexpected, as no bulk Si should be present. This is most likely due to defect-related absorption. Furthermore, the spectra, before and after annealing, are distorted by interference effects, so the actual intercept value is unclear. Therefore it can be seen, in this case, using the Tauc method to extract the band gap is not valid, without correcting for these effects.[2, 3] The PDS allows absorption to be measured without interference effects introduced by the sample structure, as is presented in the next section.

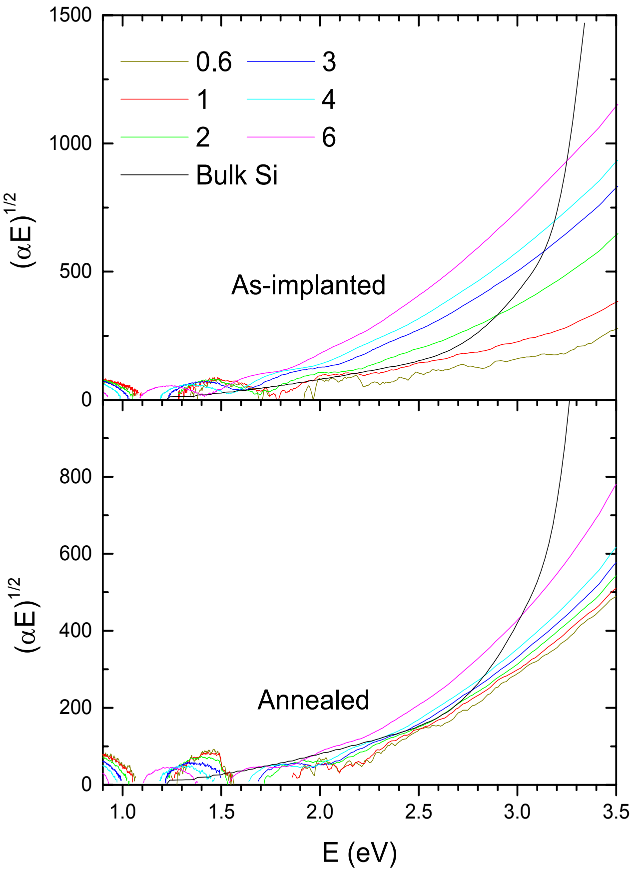

Figure 3-11: Tauc plots (for indirect band gap) of samples, before and after annealing. Bulk Si is also included as a comparison. The implantation fluence is indicated in 10^{17} cm^{-2}.

3.4.4.2 Photothermal Deflection Spectroscopy

Figure 3-12 shows a Tauc plot of the data from PDS measurements. It should be mentioned that the data measured with PDS are raw and were scaled to match the spectra measured with the spectrophotometer, in the 600 - 800 nm wavelength region. It can be seen that the Tauc plots closely follow the bulk Si values, implying that the indirect band gap is not significantly increased by quantum confinement. On face value, this is surprising, as the PL showed a shift in peak wavelength (energy) with implant fluence. However, the apparent absence of a quantum confinement induced blue-shift of the absorption edge is attributed to the broad size distribution of the nanocrystals.[3] The absorption spectrum is expected to be dominated by larger nanocrystals (those with diameters greater than the Bohr exciton radius in silicon (4.9 nm)), which have weak confinement. Furthermore, PL probes optically active nanocrystals, whereas PDS probes both active and defective nanocrystals. Thus, making steadfast conclusions based on apparent differences in results obtained by the two techniques is ill-advised.

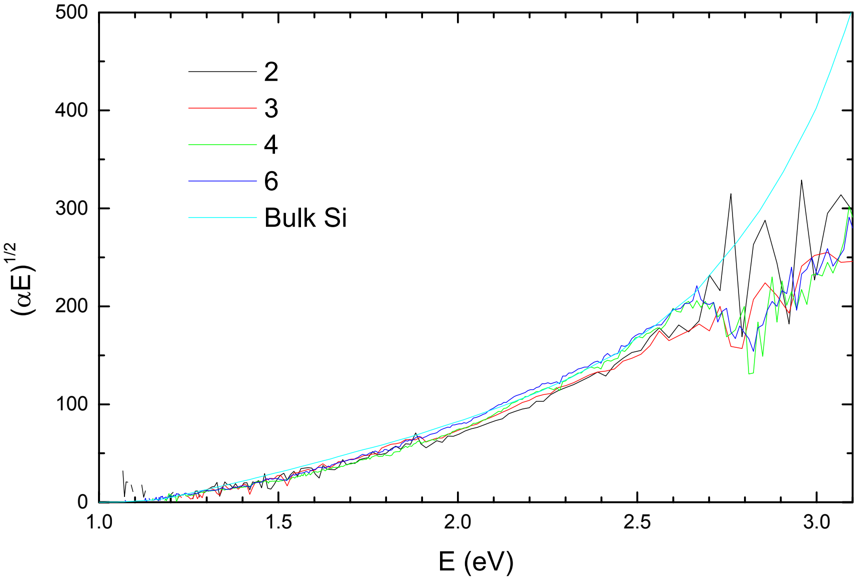

Figure 3-12: Tauc plot obtained from PDS measurements on samples, after annealing. The implantation fluence is indicated in 10^{17} Si/cm^2.

3.5 Concluding Remarks

The optical absorption spectra of silicon-implanted silica slides were measured with spectrophotometry and PDS. Tauc plots of PDS data of silicon nanocrystals showed little variance from bulk Si data. This is explained by the dominant absorption of large nanocrystals. In contrast, spectrophotometry data was complicated by features due to optical interference. This structure was shown to correlate with the transmittance of the samples as calculated from the modified refractive index profile and small particle absorption for each implant and can readily lead to misinterpretation of absorption spectra.[2]. Because of the high extinction coefficient of Si, small particle absorption, rather than scattering, was found to be the dominant contributor to the extinction cross-section at short-wavelengths.

Lastly, from the results presented here, comparing the band gap of nanocrystals extracted from PL measurements to that extracted from optical absorption measurements is not advised. In particular, non-radiative recombination preferentially diminishes PL from larger nanocrystals, as evident from a large red-shift after passivation. However, passivation was found to have no effect on optical absorption measurements. Furthermore, PL probes optically-active nanocrystals whereas optical absorption also probes defective and nanocrystals with weak confinement.

3.6 References

[1] D. Kovalev, H. Heckler, G. Polisski, et al., Phys. Stat. Sol. B **215**, 871 (1999).

[2] R. G. Elliman, M. J. Leder, and B. Luther-Davies, Appl. Phys. Lett. **80**, 1325 (2002).

[3] A. Dowd, R. G. Elliman, and B. Luther-Davies, Appl. Phys. Lett. **79**, 2327 (2001).

[4] C. F. Bohren and D. R. Huffman, *Absorption and Scattering of Light by Small Particles* (Wiley, New York, 1983).

[5] E. Hecht, *Optics* (Addison-Wesley, San Francisco, 2002).

[6] A. Miller, *Mietab v. 7.24, Avaliable from:* http://physics.nmsu.edu/~amiller/mietab.html.

[7] J. F. Ziegler, J. P. Biersack, and U. Littmark, *The Stopping and Range of Ions in Solids* (Pergamon Press, New York, 1985).

[8] S. Cheylan, N. B. Manson, and R. G. Elliman, J. Lumin. **80**, 213 (1999).

[9] C. Bonafos, B. Colombeau, A. Altibelli, et al., Nucl. Instr. Meth. Phys. Res. B **178**, 17 (2001).

[10] S. Cheylan and R. G. Elliman, Appl. Phys. Lett. **78**, 1225 (2001).

[11] G. Ledoux, O. Guillois, D. Porterat, et al., Phys. Rev. B **62**, 15942 (2000).

[12] D. E. Aspnes, in *Properties of Crystalline Silicon*, edited by R. Hull (INSPEC, IEE, London, 1999), p. 683.

[13] F. Jenkins and H. White, *Fundamentals of Optics* (McGraw-Hill, New York, 1976).

[14] S. E. Bialkowski, *Photothermal Spectroscopy Methods for Chemical Analysis* (Wiley, New York, 1996).

[15] C. W. White, J. D. Budai, S. P. Withrow, et al., Nucl. Instr. Meth. Phys. Res. B **141**, 228 (1999).

CHAPTER
4

Annealing Environment

This chapter investigates the effect of annealing environment on the photoluminescence (PL) from silicon nanocrystals synthesized in fused silica by ion implantation and thermal annealing as a function of annealing temperature and time. The choice of annealing environment (Ar, N_2, or 5 % H_2 in N_2) is found to affect the shape and intensity of luminescence emission spectra, an effect that is attributed both to variations in nanocrystal size and the density of defect states at the nanocrystal/oxide interface.

4.1 Introduction

There has been extensive work over the past decade on the optical properties of porous Si and Si nanocrystals embedded in SiO_2, with a particular emphasis on the strong room-temperature luminescence observed from these materials.[1] Although the exact mechanism for light emission remains controversial, it is well established that the emission energy is dependent on nanocrystal size[2] and that non-radiative surface defects (including P_b-type defects) compete with radiative processes.[3] In this respect, SiO_2 is the ideal matrix for Si nanocrystals as it can passivate a large fraction of the dangling bonds that cause non-radiative quenching.[4] Hydrogen passivation (see Chapter 5) has been shown to have a further passivating effect on non-radiative defects at the Si/SiO_2 interface and consequently to cause a significant increase in the luminescence efficiency of silicon nanocrystals.[4-8]

Although the effect of annealing environment on nanocrystal luminescence has not been studied explicitly, it is well known that the choice of environment during thermal annealing of planar Si/SiO_2 interfaces can affect the interfacial defect density.[9] For example, Ar gas is generally considered as an inert annealing environment. Molecular nitrogen is also believed to be relatively inert for annealing temperatures < 1200 °C, though prolonged annealing at temperatures > 925 °C has been shown to result in the generation of fixed oxide charge after an initial reduction.[10] Moreover, nitrogen has been shown to be incorporated in Si/SiO_2 layers, predominantly at the interface, during high-temperature annealing in a N_2 environment.[11] Hydrogen also interacts with Si. For example, the exposure of a-Si:H films to atomic hydrogen leads to an etching of the film (strained Si-Si bonds) and eventually to its transformation into nanocrystalline material.[12] Clearly, the choice of environment during the formation of silicon nanocrystals embedded in SiO_2, though often ignored or assumed unimportant, may well have a significant effect on their luminescence.

4.2 Experimental Details

4.2.1 Sample Preparation

Fused silica plates, 1 mm thick, were implanted with 100 keV Si^- ions to a fluence of 8×10^{16} cm^{-2}, corresponding to an excess Si concentration of 10 at. % at the projected range of 150 nm.[13] The nucleation and growth of nanocrystals was achieved by annealing implanted samples at 1100 °C for either 1 hour or 16 hours (the former represents a typical annealing schedule, whereas the latter is known to create a steady-state size-distribution of nanocrystals).[14] Thermal annealing was performed in a quartz-tube furnace with a flowing environment of either high-purity (> 99.98 %) Ar, N_2, or 5 % H_2 in N_2 (forming gas - FG) (Sample set A). Portions of these samples were subsequently annealed for 1 hour at 500 °C in FG (Sample set B) or 750 °C in N_2 (Sample set C), the former to compare the effects of hydrogen passivation and the latter to compare unpassivated samples by removing hydrogen from the sample initially annealed in FG. These implant conditions were used for all the PL measurements shown in this chapter. For the Raman measurements, higher energy implants were performed to increase the Raman intensity, namely, 400 keV Si^+ ions implanted to fluences in the range from 2×10^{17} to 6×10^{17} cm^{-2}. The lowest fluence implant was chosen to yield approximately the same peak excess Si concentration as for the 100 keV implant used for PL measurements. As the nanocrystal size distribution is dependent on the initial Si excess[14] the size distributions for these two implants are expected to be similar.

4.2.2 PL and Raman

PL measurements were performed at room temperature using the 488 nm line of an Ar^+ ion laser as the excitation source. Emitted light was analyzed using a single-grating monochromator (TRIAX-320) and detected with a liquid-nitrogen cooled CCD array (EEV CCD30-11). All spectra were corrected for system response. Laser Raman spectra were recorded on a DILOR Super Labram spectrometer equipped with a liquid-nitrogen cooled CCD detector. The samples were illuminated with the 514.5 nm line of an Ar^+ ion laser with an Olympus 100× microscope objective used to focus the laser beam and collect the scattered light. (The samples annealed in N_2 exhibited a significant fluorescence background, whereas the samples annealed in Ar did not (see Figure 4-3(a)). In Figure 4-3(b), the fluorescence background was fitted with a standard polynomial and subtracted from the Raman spectra. The Raman spectrum of fused silica, measured under the same conditions, was subtracted from each spectrum.)

4.3 Experimental Results

Figure 4-1(a) and Figure 4-2(a) compare the effect of annealing environment on the PL of samples annealed at 1100 °C for 1 hour and 16 hours, respectively (Sample set A). Broad PL emission, characteristic of Si nanocrystals, is observed for all annealing environments. Although the spectra vary considerably in intensity after 1 hour, the peak positions are generally similar, implying a similar mean size for the nanocrystals. However, after the 16 hour anneal the PL spectrum from the sample annealed in Ar exhibits a significant red-shift relative to the samples annealed in the other two environments. It is also considerably lower in peak and integrated intensity. The higher PL intensity for the samples annealed in a FG environment is due to hydrogen passivation of non-radiative defects, most likely interfacial silicon dangling bonds (P_b-type defects).[4] (This is confirmed by the large reduction in intensity after hydrogen desorption, as shown in Figure 4-1(c) and Figure 4-2(c).) The sample annealed in N_2 is observed to have a higher PL intensity than that from the sample annealed in Ar, both after 1 and 16 hours.

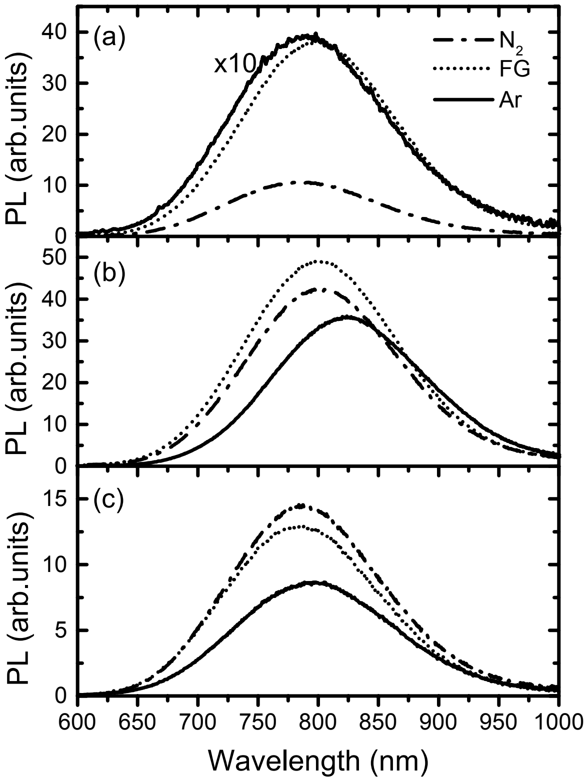

Figure 4-1: (a) PL spectra of samples annealed for 1 hour at 1100 °C in N_2, 5 % H_2 in N_2 (FG) or Ar. (b) PL of the samples from (a) after H-passivation (500 °C in FG for 1 hour). (c) PL of the samples from (a) after 750 °C in N_2 for 1 hour. The spectrum from the sample annealed in Ar in (a) has been multiplied by a factor of 10 for clarity. The PL intensities in this figure can be compared directly, as well as to Figure 4-2.

After hydrogen passivation (Sample set B), Figure 4-1(b) and Figure 4-2(b), the PL spectra from samples annealed in N_2 and FG environments are similar. In contrast, those from the samples annealed in Ar are red-shifted relative to the other two environments. This shift is also greater for the sample annealed for 16 hours in Ar (95 nm compared to N_2) than for the sample annealed for 1 hour in Ar (25nm). There are two important points to note from these comparisons: a) the observed red-shift suggests that the mean size of luminescent nancrystals is larger for samples annealed in Ar than for those annealed in N_2 or FG (the 25nm and 95nm shifts correspond to a 0.25 nm and 1 nm increase in mean diameter d_0, respectively);[2] and b) since the intensity enhancements and red-shifts due to passivation are much greater for samples annealed in Ar than for those annealed in N_2 or FG, nanocrystals formed in Ar are more likely to contain non-radiative defects.[3]

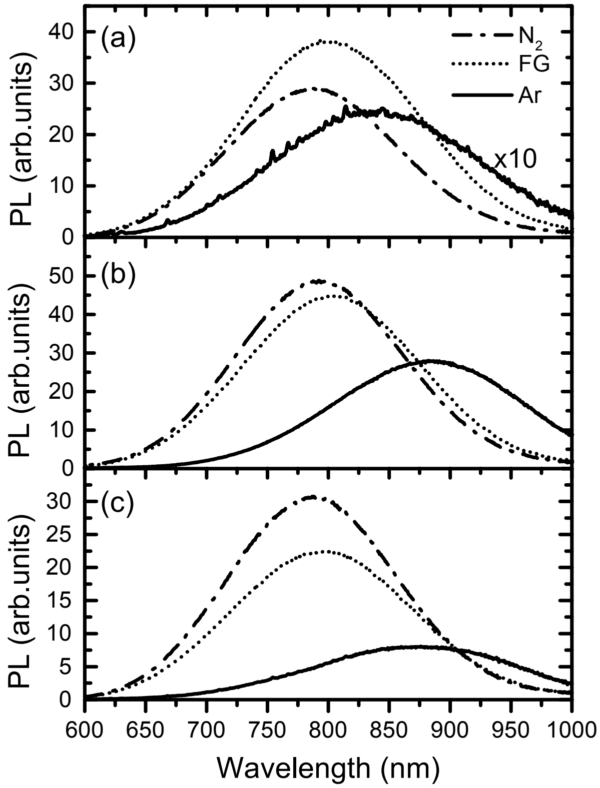

Figure 4-2: (a) PL spectra of samples annealed for 16 hours at 1100 °C in N_2, 5 % H_2 in N_2 (FG), or Ar. (b) PL of the samples from (a) after H-passivation (500 °C in FG for 1 hour). (c) PL of the samples from (a) after 750 °C in N_2 for 1 hour. The spectrum from the sample annealed in Ar in (a) has been multiplied by a factor of 10 for clarity. The PL intensities in this figure can be compared directly, as well as to Figure 4-1.

Figure 4-1(c) and Figure 4-2(c) show PL spectra from the samples initially annealed in different environments (for 1 hour and 16 hours, respectively) following an additional 750 °C anneal in N_2 for 1 hour (Sample set C). The samples initially annealed in FG yield slightly less emission than the samples annealed in N_2 after this step. This suggests that hydrogen has some effect on the growth process, possibly through etching strained Si-Si bonds.[12] Since the samples initially annealed in N_2 or Ar should contain negligible levels of hydrogen, the increase in their PL intensities after this lower temperature anneal (compare with Figure 4-1(a) and Figure 4-2(a)) is believed to primarily result from a reduction in non-radiative defects at the Si/SiO_2 interface. Significant growth of the nanocrystals is unlikely at 750 °C and this is supported by the absence of any red-shift in the emission.[15] However, this anneal is sufficient to relieve interfacial stress at the Si/SiO_2 interface. Since stress is known to affect the concentration and morphology of defects at the Si/SiO_2 interface,[16] any change in the level of stress may be expected to influence the luminescence. Thus, the increase in PL emission after the additional 750 °C anneal for samples initially annealed in N_2 and Ar is likely due to the relaxation of stress. That the effect is not due to additional N_2 incorporation is demonstrated by a comparable increase in emission for the Ar sample subsequently annealed in Ar at 750 °C (not shown), rather than in N_2.

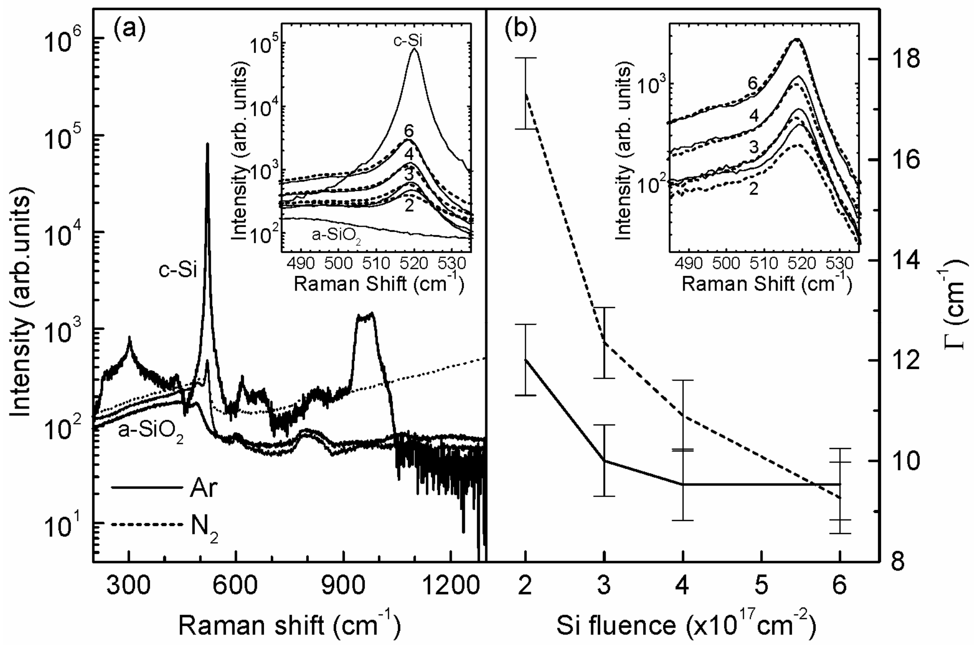

Figure 4-3: (a) Semi-logarithmic plot of the Raman spectra from a sample (Si implant fluence of $2x10^{17}$ cm^{-2}) annealed for 16 hours at 1100 °C in Ar or N_2, along with spectra obtained for bulk Si and fused silica. The inset shows a detailed view of the same data, along with the remaining implant fluences. (b) Raman linewidth as a function of Si implant fluence (extracted from the corrected Raman spectra shown in the inset). The Si implant fluences (in cm^{-2}) are indicated on the graph in units of 10^{17} Si.cm^{-2}.

The differences in PL shape and intensity resulting from the Ar environment have been, in part, attributed to differences in nanocrystal size. For example, PL modeling[2] indicates a mean size difference of 1 nm between samples annealed for 16 hours in Ar and N_2 (Figure 4-2(b)). In an attempt to verify this difference, Raman spectroscopy was undertaken on samples annealed in the different ambients. Figure 4-3(a) shows raw Raman spectra obtained from a Si implanted sample (2×10^{17} cm^{-2}) annealed at 1100 °C for 16 hours in Ar or N_2, along with spectra obtained for bulk Si and fused silica. The inset shows a detailed view of raw spectra from the full range of samples. Corrected spectra (background subtracted) are shown inset in Figure 4-3(b). It is evident from these spectra that samples annealed in N_2 have a smaller Raman shift, lower intensity, and larger linewidth, Γ, than samples annealed in Ar, consistent with the former containing smaller nanocrystals.[17] This is further highlighted by Figure 4-3(b) which compares the linewidth, Γ, extracted from the corrected Raman spectra, for samples annealed in N_2 and Ar. The difference between the samples decreases with increasing fluence and is most pronounced for the lowest fluence sample that is most similar in peak Si excess to the samples used for the PL study. However, the PL spectra for the full fluence range of Raman samples show differences between annealing in Ar or N_2 (see Figure 4-4); with the PL from samples annealed in Ar always red-shifted in comparison to the PL from those annealed in N_2. It must also be kept in mind that PL is only sensitive to luminescent nanocrystals whereas Raman spectroscopy is sensitive to all nanocrystals.

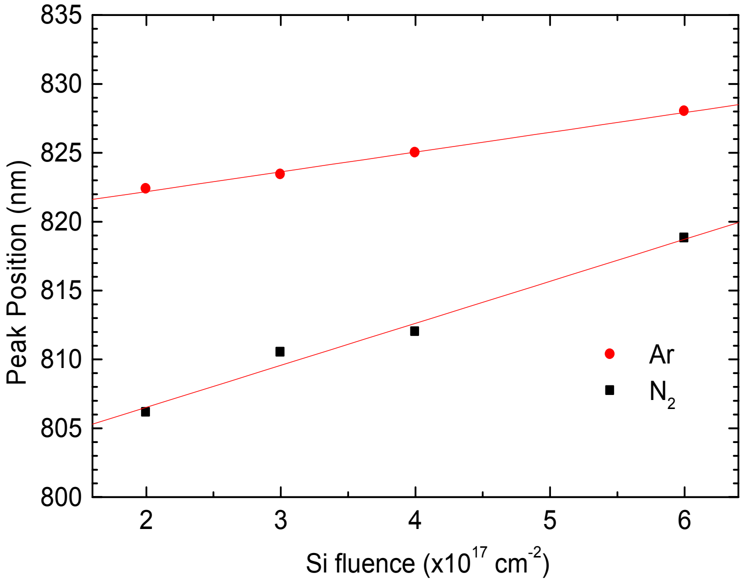

Figure 4-4: PL peak position versus implantation fluence (for samples used for Raman measurements) showing the apparent size difference for samples annealed in Ar or N_2 for 16 hours at 1100 °C.

The differences in Raman and PL spectra between samples annealed in N_2 or Ar suggest the incorporation of nitrogen within the oxide. (The large fluorescence background observed in the Raman spectra only for the N_2 annealed samples support this.) N_2 is relatively inert, with the direct nitridation of Si in pure N_2 requiring temperatures in the 1200 - 1300 °C range due to the high strength of the $N \equiv N$ bond (9.8 eV/molecule).[18] However, it has been observed that N_2 reacts with Si at moderate temperatures (760 - 1050 °C) in the presence of gas-phase impurities (H_2, O_2, CO_2) to form ultrathin (< 1.2 nm) oxynitride films near the Si/SiO_2

interface.[19] The presence of this interfacial nitrogen reduces the concentration of strained Si-O bonds, and suppresses the generation of interface states during electrical stressing of the Si/SiO_2 interface.[18] Nitridation of the nanocrystals, which would consume silicon, is consistent with the PL from the N_2 annealed samples being blue-shifted with respect to Ar annealed samples. It would also be expected to have an effect on the nanocrystal surface passivation.

4.4 Concluding Remarks

In conclusion, the choice of annealing environment was found to have a significant effect on the luminescence of Si nanocrystals. PL from samples annealed at 1100 °C in N_2 and FG (5 % H_2 in N_2) were found to be similar, after the effects of hydrogen passivation were taken into account. The Ar environment, on the other hand, produced significantly different PL; especially after extended annealing times (16 hours). These results are consistent with the common view that annealing in Ar is a simple process of thermal relaxation, while annealing in N_2 is a process of thermal relaxation that is compounded by the exchange of nitrogen with the oxide network. PL and Raman spectroscopy suggest that N_2-containing environments produce smaller nanocrystals, most likely through oxynitridation. This is further supported by PL data which indicates that annealing in N_2 also improves the degree of surface passivation.

References

1 D. Kovalev, H. Heckler, G. Polisski, and F. Koch, Phys. Status Solidi B **215,** 871 (1999).

2 G. Ledoux, O. Guillois, D. Porterat, C. Reynaud, F. Huisken, B. Kohn, and V. Paillard, Phys. Rev. B **62,** 15942 (2000).

[3] M. Lannoo, C. Delerue, and G. Allan, J. Lumin. **70,** 170 (1996).

[4] A. R. Wilkinson and R. G. Elliman, Phys. Rev. B **68,** 155302 (2003).

[5] K. S. Min, K. V. Shcheglov, C. M. Yang, H. A. Atwater, M. L. Brongersma, and A. Polman, Appl. Phys. Lett. **69,** 2033 (1996).

[6] E. Neufield, S. Wang, R. Apetz, C. Buchal, R. Carius, C. W. White, and D. K. Thomas, Thin Solid Films **294,** 238 (1997).

[7] S. P. Withrow, C. W. White, A. Meldrum, J. D. Budai, D. M. Hembree-Jr., and J. C. Barbour, J. Appl. Phys. **86,** 396 (1999).

[8] S. Cheylan and R. G. Elliman, Appl. Phys. Lett. **78,** 1912 (2001).

[9] Y. C. Cheng, Prog. Surf. Sci **8,** 181 (1977).

[10] M. Revitz, S. Raider, and R. Gdula, J. Vac. Sci. Technol. **16,** 345 (1979).

[11] S. Raider, R. Gdula, and J. Petrak, Appl. Phys. Lett. **27,** 150 (1975).

[12] S. Sriraman, S. Agarwal, E. Aydil, and D. Maroudas, Nature **418,** 62 (2002).

[13] J. F. Ziegler, J. P. Biersack, and U. Littmark, *The Stopping and Range of Ions in Solids* (Pergamon Press, New York, 1985).

[14] M. López, B. Garrido, C. Bonafos, A. Pérez-Rodríguez, J. Morane, and A. Claverie, Nucl. Instr. and Methods Phys. Res. B **178,** 89 (2001).

[15] G. H. Li, K. Ding, Y. Chen, H. X. Han, and Z. P. Wang, J. Appl. Phys. **88,** 1439 (2000).

[16] A. Stesmans, J. Appl. Phys. **92,** 1317 (2002).

[17] I. Campbell and P. Fauchet, Solid State Commun. **58,** 739 (1986).

[18] S. K. Ghandi, *VLSI fabrication principles: silicon and gallium arsenide*, 2nd ed. (John Wiley & Sons, NY, 1994).

[19] M. L. Green, T. Sorsch, L. C. Feldman, W. N. Lennard, E. P. Gusev, E. Garfunkel, H. C. Lu, and T. Gustafsson, Appl. Phys. Lett **71,** 2978 (1997).

CHAPTER

5

Kinetics of Passivation with H_2

Time-resolved photoluminescence (PL) measurements are used to study the passivation kinetics of luminescence-quenching defects, associated with Si nanocrystals in SiO$_2$, during isothermal and isochronal annealing in molecular hydrogen. The passivation of these defects is modeled using the Generalized Simple Thermal (GST) model of simultaneous passivation and desorption, proposed by Stesmans. Values for the reaction-rate parameters are determined and found to be in excellent agreement with values previously determined for paramagnetic Si dangling-bond defects (P$_b$-type centers) found at planar Si/SiO$_2$ interfaces; supporting the view that non-radiative recombination in Si nanocrystals is dominated by such defects.

5.1 Introduction

Thermal oxidation of Si creates interfacial defects as a result of strain. These can act as charge traps and thereby adversely affect the operation of metal-oxide-semiconductor (MOS) devices. The minimization of such defects is therefore a critical step in the fabrication of such devices. It has long been known that hydrogen participates in the passivation of electrically active defects.[1] In particular, P$_b$-type defects ($^{\bullet}$Si $\equiv$ Si$_3$), which are known to be a major source of charge trapping at the Si/SiO$_2$ interface, can be electrically inactivated through chemical reaction with hydrogen.[2] Consequently, a post-metallization anneal (PMA) in forming gas (5 % - 30 % H$_2$ in N$_2$) has become standard practice in device manufacturing.[1] Early work by Brower[3, 4] and more recent studies by Stesmans[5-8] have brought insight to the underlying kinetics of this process for planar interfaces.

Si nanocrystals embedded in SiO$_2$ exhibit strong room-temperature luminescence as a direct consequence of their small size.[9-13] As such, they offer the potential to combine electronic and optical functionality in Si-based devices. They are generally fabricated by the precipitation of excess Si in silicon-rich oxides (SRO), where the latter are produced either during deposition, using techniques such as plasma-enhanced chemical vapour deposition (PECVD), or subsequent to the growth of a stoichiometric SiO_2 layer by ion-implantation of Si. Precipitation typically requires temperatures in the range of 1000 - 1100 °C and produces nanocrystals with mean diameters in the range of 3 - 5 nm.[13] Importantly, the SiO_2 acts to passivate the surface of the Si nanocrystals; reducing the number of surface defects and enhancing the luminescence efficiency. Si nanocrystals prepared in this way are approximately spherical in shape and likely have a range of crystallographic surface orientations (larger nanocrystals might be expected to have {111} facets, as these are the minimum energy surfaces). Despite the different geometry, the same interface defects prevalent in Si-based MOS devices are thought also to occur at the Si nanocrystal/oxide interface.[14-16]

It has been shown that a single dangling bond defect is enough to quench the visible luminescence of a Si nanocrystal.[17] Consequently, hydrogen passivation of nanocrystals has been shown to considerably increase their luminescence efficiency by inactivating these defects.[18-24] Passivation is usually achieved by thermal annealing of the nanocrystals in forming gas, although ion implantation of hydrogen or deuterium with subsequent thermal treatment can be used to similar effect.[19] Despite the importance of the passivation process in achieving maximum luminescence, the kinetics of this process have not yet been fully explored.

5.2 Kinetics of Passivation and Desorption

Interfacial dangling bonds, of which the P_b defects are an important class, result from the lattice mismatch between Si and SiO_2.[5] They have been studied in detail by electron-spin resonance (ESR) and electrical methods,[25] though ESR is typically used to detect these paramagnetic defects. At the (111) Si/SiO_2 interface, only one type of defect is observed by ESR, known as the P_b center, whereas the technologically dominant (100) Si/SiO_2 contains P_{b0} and P_{b1} variants.[6] The P_{b0} defect is always encountered, whereas the appearance of the P_{b1} defect appears to require a minimum level of thermal interfacial relaxation.[26] Studies suggest that the P_b and P_{b0} variants are chemically identical and both have been identified as electrical interface traps.[5]

From early work by Brower[3, 4] on open (111) Si/SiO_2 structures, the thermal passivation of P_b defects in molecular H_2 and desorption in vacuum are modeled by basic chemical reactions in which the reaction is limited by the availability of "reactive" sites,

$$P_b + H_2 \xrightarrow{k_f} P_b H + H \quad \text{for passivation, and} \qquad \textbf{(1)}$$

$$P_b H \xrightarrow{k_d} P_b + H \quad \text{for desorption,} \qquad \textbf{(2)}$$

where the forward and desorption rate constants are given by the Arrhenius expressions $k_f = k_{f0}\exp(-E_f/kT)$ and $k_d = k_{d0}\exp(-E_d/kT)$, respectively. This model relies on the high-diffusivity of molecular H_2 in SiO_2, implying that the passivation process is reaction limited, not diffusion limited. Using square brackets to denote concentration, the rate equations for passivation and depassivation are then respectively given by

$$\frac{d[P_b]}{dt} = -k_f[H_2][P_b]\,, \qquad \textbf{(3)}$$

and

$$\frac{d[P_b]}{dt} = k_d[P_bH] = k_d(N_0 - [P_b])\,, \qquad \textbf{(4)}$$

which, for independent reactions, lead to the simple exponential decay solutions

$$\frac{[P_b]}{N_0} = \exp(-k_f[H_2]t)\,, \qquad \textbf{(5)}$$

and

$$\frac{[P_b]}{N_0} = 1 - \exp(-k_d t)\,, \qquad \textbf{(6)}$$

where $N_0 = [P_b] + [P_bH]$, the maximum number of defects. $[H_2]$ is the volume concentration of H_2 at the Si/SiO$_2$ interfaces, E_f and E_d are the respective activation energies for passivation and desorption, and k is Boltzmann's constant.

Later work by Stesmans revealed the existence of distinct spreads, σ_{Ef} and σ_{Ed}, in the activation energies E_f and E_d, respectively. The spreads are seen as a natural result of site-to-site variations in the P_b defect morphology induced by non-uniform interfacial stress, the resulting strain affecting the individual P_b-H bond strengths via weak orbital rearrangements of the unpaired Si sp^3 hybrids.[5] The magnitudes of the spreads are not unique as they depend on the thermal history of the SiO$_2$ structure.[5]

Including the spreads in Brower's model, a generalized consistent simple thermal (GST) model was attained by Stesmans,[6] which accurately described the kinetics of passivation and desorption, accounting for all experimental data for planar interfaces. By convoluting a Gaussian spread in activation energies with Brower's equations, Stesmans obtained

$$\frac{[P_b]}{N_0} = \frac{1}{\sqrt{2\pi}\sigma_{E_f}} \int_0^{\infty} \exp - \left[\frac{(E_{fi} - E_f)^2}{2\sigma_{E_f}^2} + t k_{f0} [H_2] \exp(-E_{fi}/kT) \right] dE_{fi}\,, \qquad \textbf{(7)}$$

and

$$\frac{[P_b]}{N_0} = 1 - \frac{1}{\sqrt{2\pi}\sigma_{E_d}} \int_0^{\infty} \exp - \left[\frac{(E_{di} - E_d)^2}{2\sigma_{E_d}^2} + t k_{d0} \exp(-E_{di}/kT) \right] dE_{di}\,, \qquad \textbf{(8)}$$

where $k_d = k_{d0}\exp(-E_{di}/kT)$ and $k_f = k_{f0}\exp(-E_{fi}/kT)$. E_f and E_d now represent mean activation energies.

In general, both reactions will proceed concurrently, so that during passivation in H_2 the reverse reaction (desorption) will occur if the temperature is high enough. As outlined by Stesmans,[6] by coupling Brower's equations (Equation (5) and Equation (6)) under the condition that $[H_2]$ at the interface is in continual equilibrium with the ambient $[H_2]$, the full interaction case for passivation in H_2 (starting from an exhaustively dissociated P_b system) is given by

$$\frac{[P_b]}{N_0} = \frac{1}{2\pi\sigma_{E_f}\sigma_{E_d}} \int_0^\infty \int_0^\infty \exp\left[-\frac{(E_{di}-E_d)^2}{2\sigma_{E_d}^2} - \frac{(E_{fi}-E_f)^2}{2\sigma_{E_f}^2} \right] \times \frac{1}{k_d + k_f[H_2]} \left\{ k_d + k_f[H_2]\exp[-(k_d + k_f[H_2])t] \right\} dE_{di}\, dE_{fi} \qquad \textbf{(9)}$$

where a Gaussian spread in activation in both the forward and desorption energies has been incorporated. The integration ranges can be reduced so they only include possible E_{di} and E_{fi} values.

The hydrogen concentration in the sample is calculated assuming that the H_2 diffuses very rapidly through the oxide, as shown by Shelby.[27] $[H_2]$ corresponds to the physical solubility of H_2 in vitreous silica so the amount of H_2 in solution at low pressures (P) is given by

$$[H_2] = C_0 = K(T)PV^{-1}, \qquad \textbf{(10)}$$

where V^{1} is the concentration of sites into which H_2 dissolves in vitreous silica (1.27×10^{21} sites/cm^3),[27] and $K(T)$ is specified by the expression[28]

$$K(T) = \left[\frac{h^2}{2\pi mkT}\right]^{\frac{3}{2}} \left[\frac{1}{kT}\right] \left[\frac{\exp(-h\nu/2kT)}{1-\exp(-h\nu/kT)}\right]^3 \exp(-\varepsilon/kT)\,. \qquad \textbf{(11)}$$

The attempt frequency, ν, corresponds to 4.1×10^{12} Hz for H_2 in vitreous SiO_2. The binding energy ε for a molecule of hydrogen of mass m to a SiO_2 surface site is -0.105 eV, and corresponds to the heat of adsorption at the surface.[27] The values for vitreous SiO_2 are assumed to be equivalent to those of thermally grown SiO_2.

5.3 Relating Nanocrystal Luminescence to Defect Density

Time-resolved PL can be used to extract the rise and decay lifetimes of the nanocrystal luminescence by modulating the excitation source. The luminescence decay is characterized by a stretched exponential shape,[29, 30] given by

$$I(t) = I_0 \exp\left[-\left(\frac{t}{\tau}\right)^{\beta}\right], \qquad \textbf{(12)}$$

where $I(t)$ and I_0 are the intensity as a function of time and at $t = 0$, respectively. τ and β are both wavelength dependent and are respectively the lifetime and a dispersion factor. The dispersion factor is basically a measure of the relaxation lifetimes involved in the luminescence decay process where a smaller β means a broader lifetime distribution.[31] $\beta = 1$ yields a simple exponential and corresponds to zero distribution in the lifetime. In practice, usually $\beta < 1$ meaning a distribution of relaxation lifetimes are involved due to charge transfer between nanocrystals and other nanocrystals or defects.

Once the excitation source is turned on, the luminescence rise time τ_{on} can be expressed as $\tau_{on}^{-1} = \sigma\phi + \tau^{-1}$.[32] Thus, if $\sigma\phi << \tau^{-1}$, then $\tau_{on} \approx \tau$ and we are in the low pump power regime, where σ is the nanocrystal excitation cross-section and ϕ is the photon flux. In this regime, the PL intensity of the emitting centres can be approximated by the following expression[33]

$$I = \sigma\phi \frac{\tau}{\tau_R} n^*, \qquad \textbf{(13)}$$

where τ_R is the radiative lifetime and n^* is the total number of Si nanocrystals that are able to emit. Equation (13) shows that, for constant excitation conditions, a variation of the luminescence yield can only be due to a change in τ or n^* or both, since τ_R and σ are independent of defect effects. This allows the extraction of a relative value of n^*, the number of emitting nanocrystals, from the PL intensity and lifetime.

A quick check of the experimental parameters employed in this study confirms the validity of the low pump approximation. (For Si nanocrystals with diameters in the range of 3 - 5 nm, σ has a value of $\approx 1\times10^{-16}$ cm^2.[32] The photon flux $\phi \approx 2.5\times10^{18}$ cm^{-2}s^{-1} (for a 10 mW laser at 488 nm with a spot size of 1 mm^2) giving $\sigma\phi \approx 2.5\times10^2$. $\tau^{-1} > 1\times10^4$ was measured for all samples. This was also directly verified by measuring the rise and decay lifetimes experimentally.)

It has been shown that a nanocrystal effectively becomes "dark" (stops luminescing) when it contains at least one defect. This is because in the visible PL range the non-radiative capture by neutral dangling bonds is much faster than radiative recombination.[17] Consequently, assuming a linear relationship between the number of defects and defective nanocrystals,

$$[P_b] \propto n_{dark} = n_{total} - n^*, \qquad \textbf{(14)}$$

and

$$N_0 \propto n_{total} - n^*_{ref}, \qquad \textbf{(15)}$$

where n_{total} is the total number of nanocrystals (a constant) and n_{dark} are the nanocrystals that contain at least one defect and therefore do not luminesce. n^*_{ref} is constant as it is the number of luminescing nanocrystals in the reference sample, which contains the maximum number of recoverable defects N_0. The reference sample is the unpassivated sample, so $[P_b]/N_0 \leq 1$. The proportionality constants for Equation (14) and Equation (15) will be the same, so using these equations we can write

$$\frac{N_0 - [P_b]}{N_0} \propto n^* - n^*_{ref}, \qquad \textbf{(16)}$$

and so

$$n^* - n^*_{ref} \propto 1 - \frac{[P_b]}{N_0}. \qquad \textbf{(17)}$$

It is convenient to express the number of emitting nanocrystals relative to the reference sample, from Equation (13),

$$\frac{n^*}{n^*_{ref}} = \frac{I}{I_{ref}} \frac{\tau_{ref}}{\tau}, \qquad \textbf{(18)}$$

since $\sigma\phi$ is kept constant and τ_R is independent of defect effects.

We now have a procedure to relate the luminescence intensity and lifetime to the relative defect density. This allows the application of the Stesmans' GST model to extract the chemical kinetics of the hydrogen passivation process of Si nanocrystals in SiO_2, through time-resolved PL measurements. It should be reiterated that whereas ESR specifically probes for paramagnetic P_b defects, the PL measurements are not defect specific. Therefore, the reaction-rate parameters extracted by this technique are mean values corresponding to all the luminescence-quenching defects that can be passivated by hydrogen. This said, the quenching of nanocrystals luminescence is thought to be dominated by defects at the interface, where P_b defects are found.

5.4 Experimental Details

5.4.1 Sample Preparation

Si nanocrystals were synthesized by ion implantation of Si^+ into 1.25 µm SiO_2 layers grown by wet thermal oxidation at 1100 °C on B-doped (0.1 - 0.3 Ωcm) Czochralski (100) Si. The samples were implanted at an energy of 400 keV to a fluence of 2×10^{17} cm^{-2}, at room temperature. This results in a Si concentration profile with a peak excess of close to 10 at. % at a projected range of 630 nm and a straggle of 140 nm, calculated using SRIM.[34] The as-implanted samples, placed in a quartz boat, were annealed at 1100 °C in high-purity Ar (99.997 %) for 1 hour in a conventional quartz-tube furnace. This is a standard thermal treatment used to produce luminescent nanocrystals, with the high-temperature required to remove implantation damage (such as non-bridging oxygen-hole centres and oxygen vacancies)[35] and precipitate the crystals. The sample at this stage contains the maximum number of recoverable defects and was used as the reference sample. After one hour, a large number of defects is created as the nanocrystals precipitate, with longer annealing times reducing their density.[16]

Hydrogen passivation anneals were performed in high-purity (99.98 %) forming gas (5 % H_2 in N_2). Samples were annealed either isochronally or isothermally. Isochronal anneals were performed for 1 hour in the temperature range of 100 °C to 800 °C. Isothermal anneals were performed at four set temperatures (nominally 300, 350, 400, and 500 °C) for times ranging from 1 minute to 16 hours. A rapid thermal processor (AET Thermal RX) was used for annealing times ≤ 10 minutes, with the conventional tube-furnace used for all longer anneals. At the completion of each anneal, the sample was withdrawn to the cool zone of the furnace and cooled to room-temperature in the forming gas ambient.

Hydrogen desorption was performed in a N_2 ambient (99.99 %) on samples previously annealed in forming gas at 500 °C for 1 hour. The initial passivation treatment establishes the starting condition for the desorption process. 1 hour isochronal anneals were performed at temperatures in the range of 200 to 800 °C.

It should be noted that the conditions used in this work for hydrogen passivation and desorption are similar, but not identical, to those used by other authors. For the values shown in Table 5-1, hydrogen passivation was carried out in 1.1 atm H_2 (99.9999 %) and desorption was performed in vacuum. Nonetheless, N_2 is effectively inert at these temperatures (see Chapter 7) and the partial pressure of H_2 is taken into account in the modeling.

5.4.2 PL and Time-resolved PL

Photoluminescence (PL) measurements were performed at room temperature, using the 488 nm line of an Ar^+ ion laser as the excitation source. Emitted light was analyzed using a single grating monochromator (TRIAX-320) and detected with a liquid-nitrogen cooled front-illuminated open-electrode CCD array (EEV CCD30-11).

Time-resolved PL measurements were performed by modulating the laser beam with an acousto-optic modulator (Brimrose TEM-85-10). A room-temperature photomultiplier (Hamamatsu R928) was used to detect the light from the exit port of the monochromator with the grating centred at 800 nm (band pass of 40 nm). The signal from the photomultiplier was collected using a digital storage oscilloscope. Emission decay lifetimes were extracted by the least-squares fitting of a stretched exponential (Equation (12)). The timing resolution of the system is $< 1\mu s$.

5.5 Experimental Results

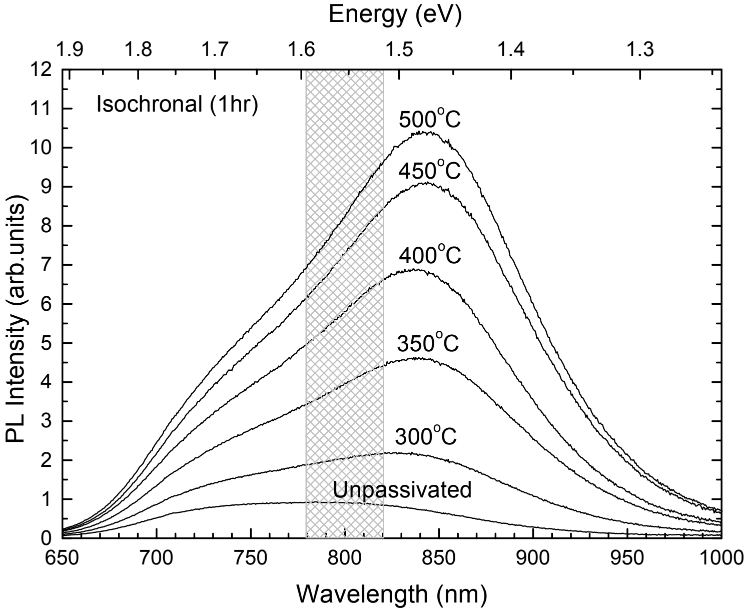

Figure 5-1: Typical nanocrystal PL spectra of the reference sample (unpassivated) after annealing for 1 hour in 5 % H_2 in N_2 at different temperatures. The annealing temperatures are indicated on the figure. The shaded box indicates the approximate detection window used for time-resolved PL measurements.

Figure 5-1 shows the effect of H-passivation on the nanocrystal PL, at a range of annealing temperatures in forming gas. The increase in PL intensity is due to the passivation of non-radiative defects at the nanocrystal/oxide interface. The shaded region represents the approximate detection window used in time-resolved PL measurements (equal to the band-pass of the monochromator centred at 800 nm). The choice of this window is arbitrary, as the trend of increasing intensity with improved passivation was found to be comparable across the whole PL spectrum.

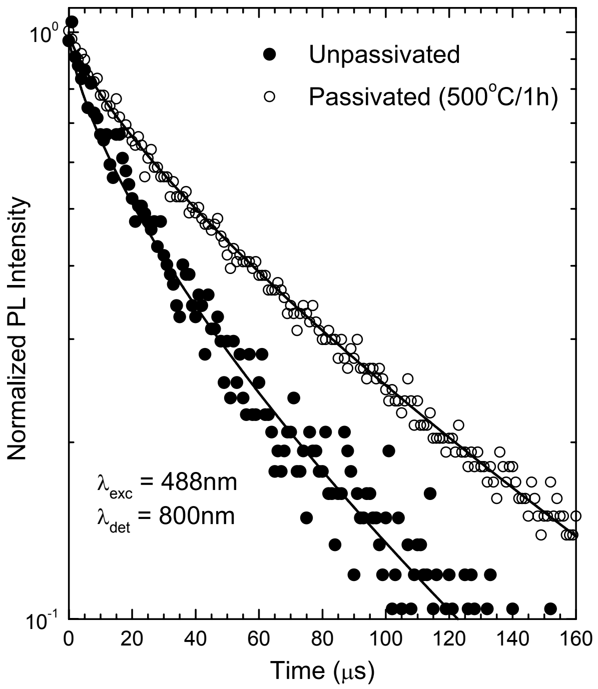

Figure 5-2: Typical normalized decay-time measurements of the PL signal at 800 nm for the reference sample before and after annealing in forming gas at 500 °C for 1 hour. The solid lines are stretched exponential fits (Equation (12)). Data was taken at room temperature.

Figure 5-2 shows a semi-logarithmic plot of the luminescence decay-time measurements for the reference sample before and after passivation at 500 °C for 1 hour in forming gas. The decay curves are clearly non-linear, and thus not well described by a simple exponential. As expected, they are well characterized by a stretched exponential shape. Fitting the PL decay curves with Equation (12) allows the extraction of τ and β as a function of the passivation and desorption anneal schedule. These values are shown in Figure 5-3 and Figure 5-4, respectively.

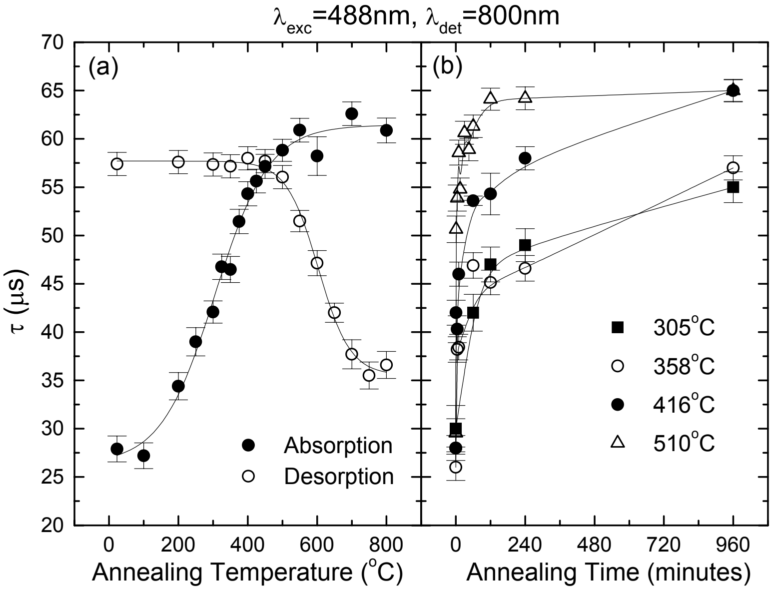

Figure 5-3: Plots of the luminescence decay lifetime for (a) the isochronal (t =1 hour) study, and (b) the isothermal study. Data is extracted from time-resolved PL measurements fitted with Equation (12). The solid lines are provided as a guide to the eye only.

The measured luminescence decay lifetime can be approximated by $\tau^{-1} = \tau_R^{-1} + \tau_{NR}^{-1}$, where τ_R is the nanocrystal radiative lifetime and τ_{NR} is the non-radiative lifetime (associated with defects and/or exciton energy migration). Consequently, as defects, which act as fast non-radiative recombination states, are passivated (eliminated), τ_{NR} increases and τ approaches τ_R. The nanocrystals also become more isolated due to the concomitant reduction in exciton migration channels (other nanocrystals or defects[36]). The complete model of this process is unclear, as the source and mechanism of luminescence from Si nanocrystals is still under debate. However, a reduction of fast-recombination sites, whether defects at the interface or within the oxide, is consistent with the observed increase in τ and β as the extent of passivation increases.

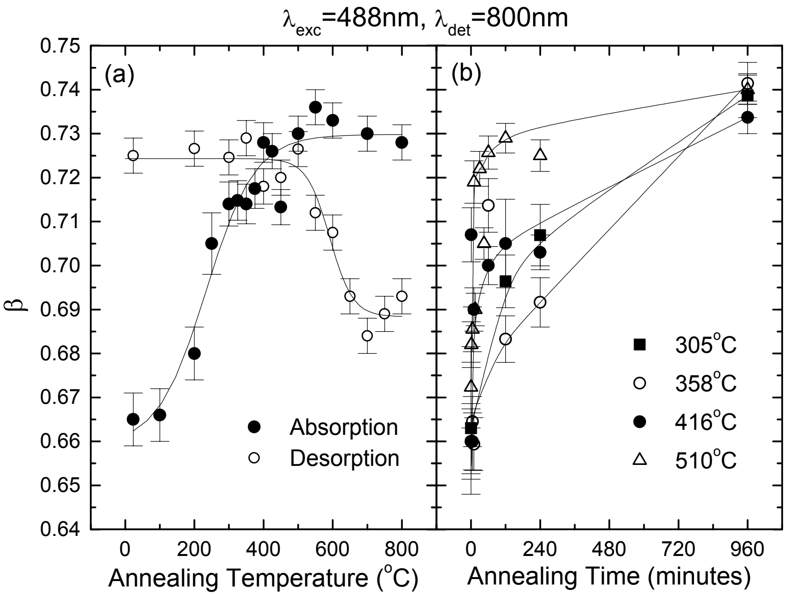

Figure 5-4: Plots of the dispersion factor for (a) the isochronal study, and (b) the isothermal study. Data is extracted from time-resolved PL measurements fitted with Equation (12). The solid lines are provided as a guide to the eye only.

The fitting of Equation (12) also enables the extraction of the intensity and lifetime enhancement for each sample, I/I_{ref} and τ/τ_{ref} respectively, due to hydrogen passivation. These quantities, along with Equation (18), then allow the corresponding enhancement of emitting nanocrystals to be determined. The results for the isochronal absorption and desorption studies are shown in Figure 5-5, and the isothermal absorption study in Figure 5-7.

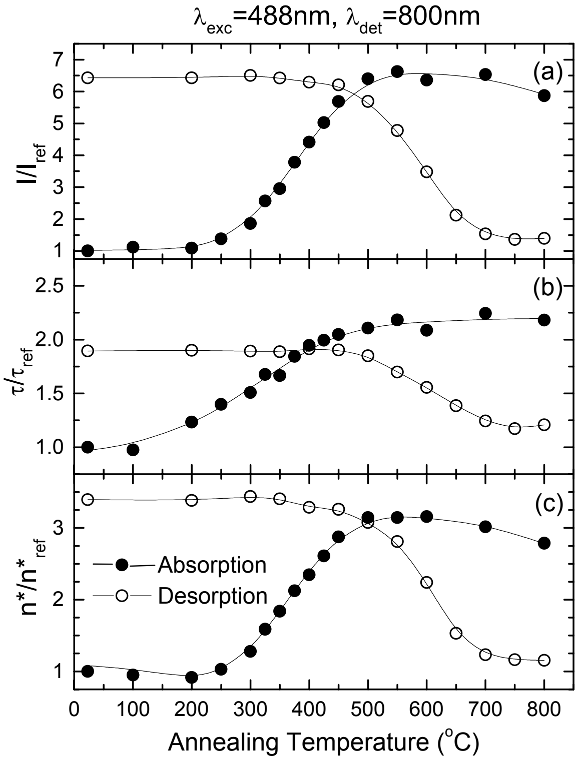

Figure 5-5: Plots of relative (a) intensity, (b) lifetime, and (c) emitting nanocrystals (from Equation (18)) versus annealing temperature, during H-passivation for 1 hour in 5 % H_2. Data is from time-resolved PL measurements. The lines are provided as a guide to the eye only.

In Figure 5-5, a factor of ≈ 6 increase is seen in intensity with optimum passivation, which is accounted for by a doubling of lifetime and a tripling of the number of luminescing nanocrystals (using Equation (13)). The action of simultaneous desorption limits the level of maximum passivation, as hydrogen is dissociated from the defects above about 450 °C.

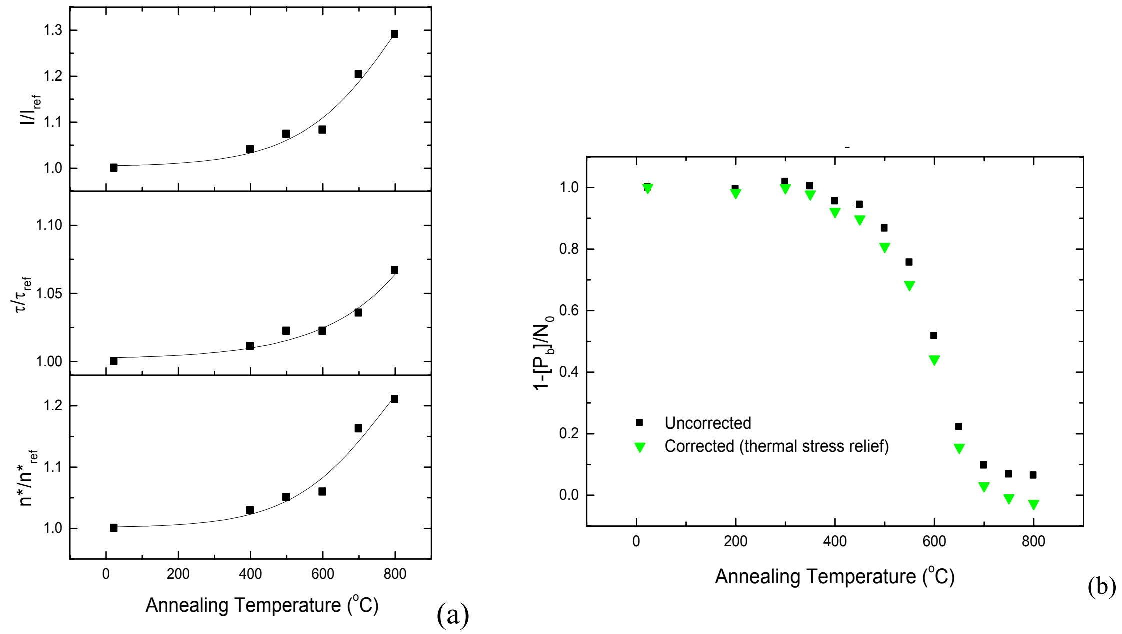

Figure 5-6: Shows thermal stress release effect on (a) PL intensity, lifetime, and number of luminescing nanocrystals, and (b) relative defect concenctration. Desorption anneals were 1 hour in N_2 at the indicated temperatures.

The hydrogen desorption study also shows that at high temperatures, where all hydrogen should be lost from the sample, the luminescence intensity and lifetime do not return completely to their pre-passivation values (see Figure 5-5). This effect was investigated and found to be due not to any residual strongly bound hydrogen but simply a thermal effect. The reference sample (unpassivated) was taken and annealed for 1 hour in N_2 at several temperatures. As shown in Figure 5-6(a), all three quantities increase as the annealing temperature increases. This is most likely to be due to the release of stress (as seen in Chapter 4), as P_b defects are reported to be stable below 850 °C.[3] The stress is generated after the anneal to form the nanocrystals, where the samples cool from 1100 °C to room temperature. The large difference in coefficients of thermal expansion for Si and SiO_2 causes a build up of stress dependent on the rate of cooling. Figure 5-6(b) shows the change in the desorption curve when this effect is taken into account. It is clear from this figure that the difference between these curves, though not linear, is small and does not change the overall position and shape of the curve significantly.

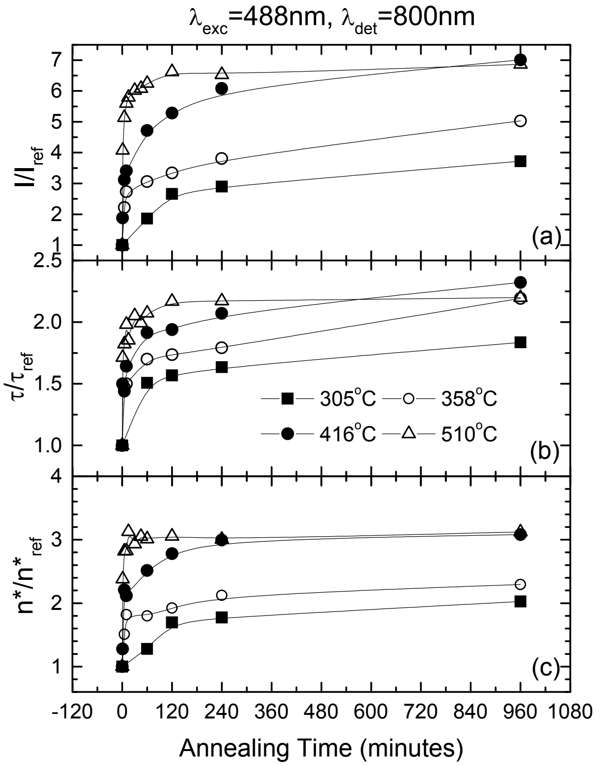

Figure 5-7: Plots of relative (a) intensity, (b) lifetime, and (c) emitting nanocrystals (from Equation (18)) versus annealing time, during H-passivation at 500 °C in 5 % H_2. Data extracted from time-resolved PL measurements. The lines are provided as a guide to the eye only.

In Figure 5-7, the isothermal data shows the same trend of increasing intensity and lifetime with improved passivation as was seen in the isochronal case (Figure 5-5). As expected, the samples annealed at higher temperatures approach optimum passivation more quickly. However, due to competition from the desorption reaction, samples annealed for 1 hour at higher temperatures will be less well passivated than those annealed at the optimum temperature around 500 °C. Similarly, samples annealed at lower temperatures require much greater annealing time to achieve similar levels of passivation. (This is highlighted by the data in Figure 5-7(c), which shows that the degree of passivation achieved after 1 hour at 510 °C will not be achieved at 305 °C even after several days annealing. That said, increasing

$[H_2]$ in the sample through annealing in pure H_2 and/or at increased pressure would reduce this time.)

5.6 Modeling the Kinetics

A global least-squares fit (of all data shown in Figure 5-8) was used to determine the parameters shown in Table 5-1, for this work. For convenience, the values obtained by others for molecular hydrogen passivation and desorption of paramagnetic P_b defects for planar (111) and (100) Si/SiO$_2$ interfaces are also included. A global fit of data over a large range is important to give uniqueness to the fit. For example, a fit of isochronal data alone can be described equally well by a range of parameter sets. The full-interaction GST model (Equation (9)) was used to model the passivation kinetics (simultaneous passivation and desorption), whereas the simpler case of pure desorption was modeled using Equation (8). The proportionality constant (for Equation (17)) between experimental data and the model was also left as a fitting parameter.

Table 5-1: Kinetic parameters for thermal passivation in H_2 (this work in 5 % H_2 in N_2) and desorption in vacuum (this work in N_2) of P_b-type defects at the Si/SiO$_2$ interface.

		E_f (eV)	σ_{Ef} (eV)	k_{f0} (10^{-8}cm^{3}s^{-1})	E_d (eV)	σ_{Ed} (eV)	k_{d0} (10^{13}s^{-1})
This work	P_b-type	1.68±0.04	0.18±0.02	9±5	2.9±0.05	0.29±0.03	2±1
(111) Si/SiO$_2$	P_b:	1.51±0.04[a]	0.060±0.004[a]	9.8(+8/-5)[a]	2.83±0.03[a]	0.09±0.03[a]	1.6±0.5[a]
(100) Si/SiO$_2$	P_{b0}: P_{b1}:	1.51±0.03[b] 1.57±0.03[b]	0.14±0.02[b] 0.15±0.03[b]	143±60[b] 143±60[b]	2.86±0.04[c] 2.91±0.03[c]	0.17[c,d]	2[c,e] 2[c,e]

[a] Ref. [6]
[b] Ref. [8]
[c] Ref. [37]
[d] Stathis suggested an overall σ_{Ed} value of 0.17 eV for P_{b0} and P_{b1} combined.
[e] This parameter (k_{d0}) was fixed at a value of 2×10^{13} s^{-1} based on physical insight (frequency of the Si-H wagging mode).

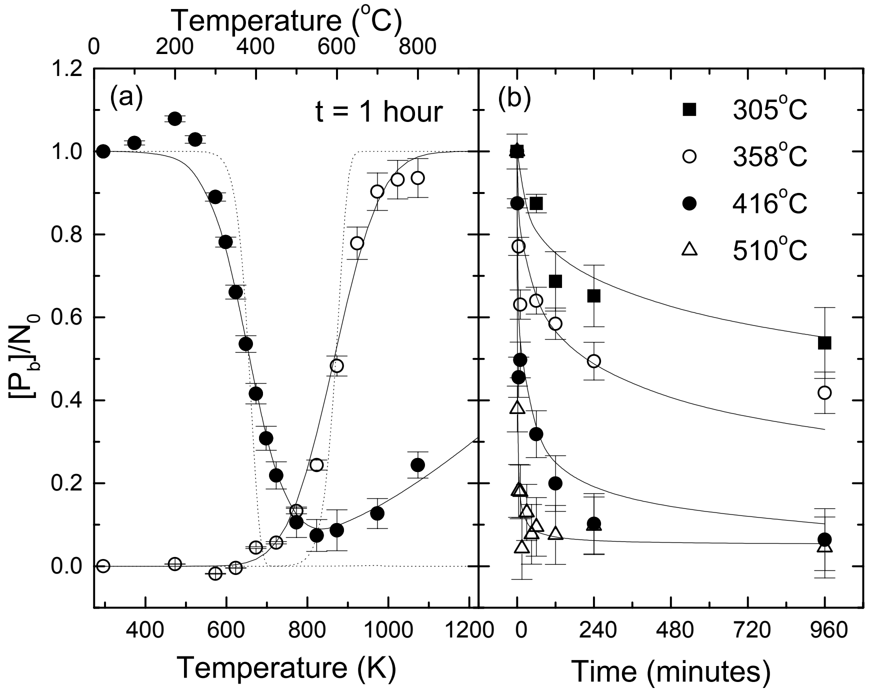

Figure 5-8: Plots relative P_b defect concentration versus (a) annealing temperature of hydrogen passivation (solid circles) and desorption (open circles) and (b) annealing time, during hydrogen passivation at 305 °C, 358 °C, 416 °C and 510 °C. The solid lines represent the global least-squares fit of the GST model (Equation (8) (for desorption only) and Equation (9)) to experimental data derived from time-resolved PL measurements through Equation (17)and Equation (18). The dotted lines are Brower's simple thermal model for passivation and desorption (Equation (5) and Equation (6)).

The values obtained in this work are in general agreement with those measured for (100) and (111) planar interfaces. This supports the view that similar defects and processes are involved in both cases. It can be noted, however, that the activation energy for the passivation reaction and the spread of activation energies for the desorption reaction both appear slightly higher than the values determined for planar interfaces. There are several possible reasons for this variation, the most obvious being: (a) the difference in interface geometry because of the approximately spherical shape of the nanocrystals; and (b) differences in the range of luminescence-killing defects involved. For example, Gheorghita *et al.*[38] identified the R defect at the (111) Si/SiO_2 interface, which was also found to be passivated by H_2 albeit with a very different activation energy and rate constant. However, Stesmans found for (111) Si/SiO_2 that $\sigma_{Ef}/E_f \approx \sigma_{Ed}/E_d$ and $\sigma_{Ed}/\sigma_{Ef} = 1.5$.[5] This is similar to that found in this work, with

$\sigma_{Ef}/E_f \approx \sigma_{Ed}/E_d \approx 10$ % and $\sigma_{Ed}/\sigma_{Ef} = 1.6$. Stesmans related σ_{Ef} and σ_{Ed} to interfacial stress, which affects the spread in P_b defect morphology. This suggests that σ_{Ef} and σ_{Ed} found in this work relate to a higher mean interfacial stress than is generally found at planar interfaces.

To gain confidence in the extracted parameters, the consistency of these parameters can be compared to the underlying physical insight. A simple model from Brower[3] predicts a k_{f0} on the order of 9.7×10^{-8} cm^3 s^{-1}. The value obtained in this work agrees well with this value and that obtained here and by Stesmans for (111) Si/SiO_2. It has been determined that the low-frequency Si-H wagging mode (Si ≡ S - H), at 1.86×10^{13} s^{-1},[39] controls thermal interfacial Si-H breaking.[7] The value of $(2 \pm 1)\times10^{13}$ s^{-1} obtained in this work also agrees well with this value.

The net effect of Equation (1) and Equation (2) is the dissociation of the H_2 molecule, with both steps resulting in emission of a hydrogen atom. Therefore, the value for H_2 dissociation in vacuum (4.52 eV at 298 K)[40] can be compared to the sum of the forward and desorption activation energies E_f and E_d, respectively. Stesmans found for (111) Si/SiO_2 a net apparent activation energy of 4.34 ± 0.06 eV and slightly higher for (100) Si/SiO_2. In this work, a net apparent activation energy of 4.58 ± 0.07 eV was found in this work, which agrees well with the value for dissociation in vacuum.

5.7 Concluding Remarks

Using time-resolved PL, the hydrogen passivation kinetics of Si nanocrystals embedded in SiO_2 has been studied both isothermally and isochronally, providing a sufficient set of data to extract the reaction-rate parameters with some confidence. The GST model proposed by Stesmans was found to well describe the passivation process of Si nanocrystals in SiO_2. The reaction-rate parameters were found to be $E_f = 1.68$ eV, $\sigma_{Ef} = 0.18$ eV, $k_{f0} = 9\times10^{-8}$ cm^{3}s^{-1} for hydrogen passivation and $E_d = 2.9$ eV, $\sigma_{Ed} = 0.29$ eV, $k_{d0} = 2\times10^{13}$ s^{-1} for hydrogen desorption. The similarity of these values to those found for P_b defects at planar Si/SiO$_2$ interfaces supports the view that non-radiative recombination is dominated by such defects. The modeling has also highlighted that the simultaneous desorption limits the level of passivation attainable. If the passivation temperature is too high, the desorption reaction dominates. This means that a one-step anneal to both precipitate and passivate the nanocrystals at 1100 °C in forming gas will not achieve the same quality of passivation as a two-step anneal (at 1100 °C) and passivation (at 500 °C) sequence. Moreover, for high temperature annealing the final level of passivation will depend on the cooling rate. On the other hand, using low passivation temperatures to avoid desorption will require extended annealing times. Finally, this work has shown that nanocrystals provide a useful model system for studying such processes using PL. However, since PL is unable to unambiguously identify specific defects, it cannot replace, but instead complements the more complex ESR.

5.8 References

[1] Y. C. Cheng, Prog. Surf. Sci **8**, 181 (1977).

[2] E. H. Poindexter and P. J. Caplan, Prog. Surf. Sci **14**, 201 (1983).

[3] K. L. Brower, Phys. Rev. B **38**, 9657 (1988).

[4] K. L. Brower, Phys. Rev. B **42**, 3444 (1990).

[5] A. Stesmans, J. Appl. Phys. **92**, 1317 (2002).

[6] A. Stesmans, J. Appl. Phys. **88**, 489 (2000).

[7] A. Stesmans, Phys. Rev. B **61**, 8393 (2000).

[8] A. Stesmans, Solid State Commun. **97**, 255 (1996).

[9] T. Shimizu-Iwayama, N. Kurumado, D. E. Hole, et al., J. Appl. Phys. **83**, 6018 (1998).

[10] D. Kovalev, H. Heckler, G. Polisski, et al., Phys. Status Solidi B **215**, 871 (1999).

[11] M. L. Brongersma, A. Polman, K. S. Min, et al., J. Appl. Phys. **86**, 759 (1999).

[12] F. Iacona, G. Franzò, and C. Spinella, J. Appl. Phys. **87**, 1295 (2000).

[13] B. G. Fernandez, M. López, C. Garcia, et al., J. Appl. Phys. **91**, 798 (2002).

[14] M. S. Brandt and M. Stutzmann, Appl. Phys. Lett. **61**, 2569 (1992).

[15] H. J. V. Bardeleben, M. Chamarro, A. Grosman, et al., J. Lumin. **57** (1993).

[16] M. López, B. Garrido, C. García, et al., Appl. Phys. Lett. **80**, 1637 (2002).

[17] M. Lannoo, C. Delerue, and G. Allan, J. Lumin. **70**, 170 (1996).

[18] E. Neufield, S. Wang, R. Apetz, et al., Thin Solid Films **294**, 238 (1997).

[19] K. S. Min, K. V. Shcheglov, C. M. Yang, et al., Appl. Phys. Lett. **69**, 2033 (1996).

[20] S. Cheylan and R. G. Elliman, Nucl. Instr. and Meth. B **148**, 986 (1999).

[21] S. P. Withrow, C. W. White, A. Meldrum, et al., J. Appl. Phys. **86**, 396 (1999).

[22] S. Cheylan and R. G. Elliman, Appl. Phys. Lett. **78**, 1225 (2001).

[23] S. Cheylan and R. G. Elliman, Appl. Phys. Lett. **78**, 1912 (2001).

[24] S. Cheylan and R. G. Elliman, Nucl. Instr. and Meth. B **175-177**, 422 (2001).

[25] E. H. Poindexter, Semicond. Sci. Technol. **4**, 961 (1989).

[26] A. Stesmans and V. V. Afanas'ev, Appl. Phys. Lett. **77**, 1469 (2000).

[27] J. E. Shelby, J. Appl. Phys. **48**, 3387 (1977).

[28] J. F. Shackelford, P. L. Studt, and R. M. Fulrath, J. Appl. Phys. **43**, 1619 (1972).

[29] J. Linnros, A. Galeckas, N. Lalic, et al., Thin Solid Films **297**, 167 (1997).

[30] L. Pavesi and M. Cescini, Phys. Rev. B **48**, 17625 (1993).

[31] G. Schlegel, J. Bohnenberger, I. Potapova, et al., Phys. Rev. Lett. **88** (2002).

[32] F. Priolo, G. Franzò, D. Pacifici, et al., J. Appl. Phys. **89**, 264 (2001).

[33] D. Pacifici, E. C. Moreira, G. Franzò, et al., Phys. Rev. B **65**, 144109 (2002).

[34] J. F. Ziegler, J. P. Biersack, and U. Littmark, *The Stopping and Range of Ions in Solids* (Pergamon Press, New York, 1985).

[35] M. Y. Valahk, V. A. Yukhimchuk, V. Y. Bratus', et al., J. Appl. Phys. **85**, 168 (1999).

[36] I. Sychugov, R. Juhasz, J. Linnros, et al., Phys. Rev. B **71**, 115331 (2005).

[37] J. H. Stathis, J. Appl. Phys. **77**, 6205 (1995).

[38] L. Gheorghita and E. Ogryzlo, J. Appl. Phys. **87**, 7999 (2000).

[39] B. B. Stefanos, A. B. Gurevich, M. K. Weldon, et al., Phys. Rev. Lett. **81**, 3908 (1998).

[40] J. A. Kerr, in *CRC Handbook of Chemistry and Physics*, edited by D. R. Lide (CRC, Boca Raton, 1992), p. 9-131.

CHAPTER
6

Kinetics of Passivation with H

In this chapter, continuous and time-resolved photoluminescence measurements are undertaken to determine the passivation kinetics of luminescence-quenching defects during isothermal and isochronal annealing in atomic hydrogen. The kinetics are compared to those for standard passivation in molecular hydrogen (Chapter 5) and found to be significantly different. Atomic hydrogen is generated using the *alneal* process, through reactions between a deposited Al layer and H_2O or –OH radicals in the SiO_2. The passivation and desorption kinetics are shown to be consistent with the existence of two classes of non-radiative defects: one that reacts with both atomic and molecular hydrogen, and the other that reacts only with atomic hydrogen. A model incorporating a Gaussian spread in activation energies is presented for atomic hydrogen passivation and desorption.

6.1 Introduction

The control of electronic traps located at the Si/SiO_2 interface is crucial to the performance of metal-oxide-silicon (MOS) devices. The inherently high concentration of traps is reduced by reacting them with hydrogen,[1] usually via annealing in forming gas or a post-metallization anneal (PMA). These traps have been studied with physical, electrical, optical, and theoretical methods with the generally accepted model being a trivalently bonded silicon atom with an unpaired electron.[2]

A PMA using Al has long been known to passivate interface traps. Balk proposed that atomic hydrogen is produced at the Al/SiO_2 interface, which then diffuses to the Si/SiO_2 interface and reacts with the interface trap.[3] A significant amount of hydrogen is produced by Al reacting with trace water or hydroxyl at the interface. A thin layer of Al oxide is produced as well as atomic hydrogen. In most cases, the water is in the form of hydroxyl groups strongly bound to surface silicon atoms.[1] This so-called *alneal* process is commonly used in solar cell fabrication to reduce the surface recombination velocity.[4] As shown in this chapter, atomic hydrogen can provide higher levels of passivation for Si nanocrystals than molecular hydrogen.[5] Furthermore, equivalent levels of passivation can be achieved with lower thermal budget. The benefit of this is the passivation step will have less thermal effect on the existing sample structure.

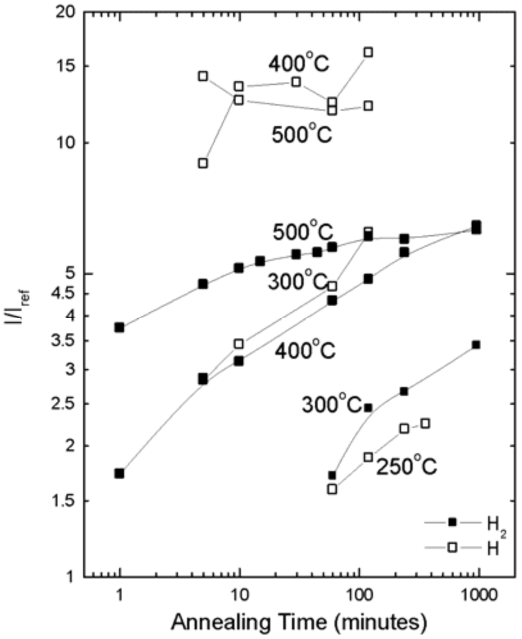

Figure 6-1: Shows PL intensity measured at a detection wavelength of 800 nm, from TRPL. The passivation kinetics are different for the two processes. Higher levels of passivation can be obtained through an *alneal*, at lower thermal budget. The lines are a guide to the eye only.

Figure 6-1 shows the PL intensity enhancement gained from annealing in molecular hydrogen and using the *alneal* process. The samples are annealed for 1 hour at the temperatures indicated on the figure. The reference intensity (I_{ref}) is the PL intensity of the sample before any passivation. Deducing the reason for the significantly improved passivation of Si nanocrystals by atomic hydrogen over molecular hydrogen is one aim of this chapter. In addition to the P_b center, work by Gheorghita *et al.,*[6] using a radio frequency probe to monitor the steady-state photogenerated charge carriers in Si, revealed two further classes of defects at (111) Si/SiO_2 interfaces; one that can be passivated with H_2 (labeled *R*) (see Figure 6-2), and one that cannot. It is therefore possible, that through annealing in either atomic or molecular hydrogen that the effect of these defects on the luminescence can be distinguished.

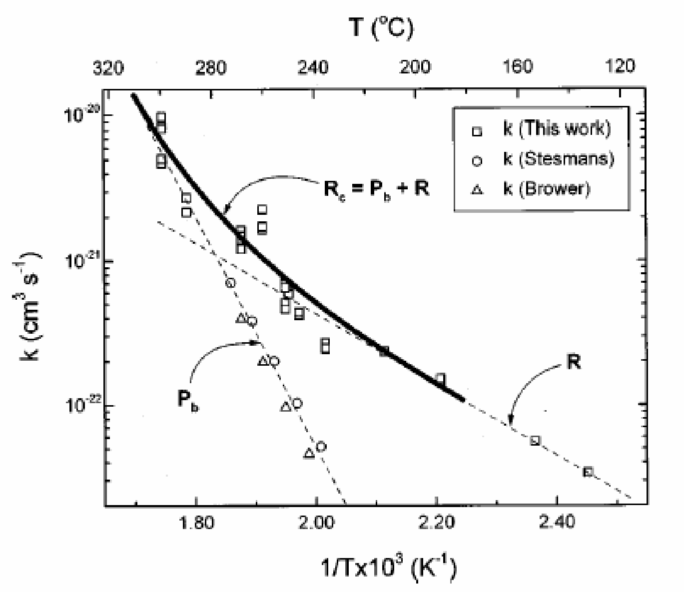

Figure 6-2: Arrhenius plot of the rate constants obtained by Stesmans, Brower, and Gheorghita *et al.*[6]

6.2 Kinetics of Passivation and Desorption

6.2.1 Molecular Hydrogen

This section briefly refers to passivation of defects by annealing in H_2 where in Chapter 5 the Generalized Simple Thermal (GST) model proposed by Stesmans[7] was found to well describe the hydrogen passivation process of Si nanocrystals in SiO_2. The similarity of the reaction-rate parameters to those found for P_b defects at planar Si/SiO_2 interfaces supports the view that non-radiative recombination is dominated by such defects.[8]

For convenience, some pertinent theory will be briefly repeated here, along with a revised method for calculating the integrals. For passivation in molecular hydrogen, the solution to the full interaction case, where the simultaneous action of passivation and desorption is considered,

$$\frac{[Si^\bullet]}{N_0}=\frac{1}{2\pi\sigma_{E_f}\sigma_{E_d}}\int_0^\infty\int_0^\infty \exp\left[-\frac{(E_{di}-E_d)^2}{2\sigma_{E_d}^2}-\frac{(E_{fi}-E_f)^2}{2\sigma_{E_f}^2}\right]$$

$$\times\frac{1}{k_d+k_f[H_2]}\left\{k_d+k_f[H_2]\exp[-(k_d+k_f[H_2])t]\right\}dE_{di}dE_{fi}\,, \qquad (1)$$

where $k_f=k_{f0}\exp\left(-E_{fi}/k_BT\right)$ and $k_d=k_{d0}\exp\left(-E_{di}/k_BT\right)$. $[H_2]$ is the hydrogen concentration and corresponds to the physical solubility of H$_2$ in silica. N_0 is $[Si^\bullet]_0$ (starting concentration of Si dangling bond defects) and equals $[Si^\bullet]+[SiH]$, the maximum number of defects. E_f and E_d now represent mean activation energies. σ_{E_f} and σ_{E_d} represent the standard deviations of the Gaussian spreads. However, as these integrals must be solved numerically they were replaced by summations for computational efficiency, as proposed by Gheorghita *et al.*[6] For integer *n*, the integral is approximated with a sum of $2n+1$ rate constants, determined by a Gaussian distribution of $2n+1$ activation energies, differing in steps of $\frac{\sigma}{2}$ between $\frac{\pm n\sigma}{2}$, centred around the mean activation energy. In the full interaction case (Equation (1)) we have two spreads, which can be approximated by

$$\frac{[Si^\bullet]}{N_0}\approx\frac{1}{A^2}\times \qquad (2)$$

$$\sum_{j=-n}^{j=+n}\sum_{k=-n}^{k=+n}\exp\left(\frac{-j^2-k^2}{8}\right)\frac{1}{k_{dk}+k_{fj}[H_2]}\left\{k_{dk}+k_{fj}[H_2]\exp[-(k_{dk}+k_{fj}[H_2])t]\right\}$$

where A is a normalization constant equal to $\sum_{j=-n}^{j=+n}\exp\left(\frac{-j^2}{8}\right)$,

$k_{fj}=k_{f_0}\exp\left(-(E_f+\frac{j\sigma_{E_f}}{2})/k_BT\right)$ and $k_{dk}=k_{d_0}\exp\left(-(E_d+\frac{k\sigma_{E_d}}{2})/k_BT\right)$. In this work, a value of $n=10$ was used, corresponding to a summation of 11 rate constants between $\pm 5\sigma$.

6.2.2 Atomic Hydrogen

This form of passivation is achieved by exposing the sample to atomic hydrogen. Reed *et al.* [1, 9] found that a two reaction model was required to model the passivation of interface traps by *alnealing*. They proposed two models, one to describe the passivation of defects on $\langle 100 \rangle$ Si, and the other for the $\langle 111 \rangle$ orientation. $\langle 111 \rangle$ is the predominant Si orientation expected at the nanocrystal surface as it is energetically favourable, so the latter model was used. This is known as the consumptive model and consists of two reactions

$$Si^{\bullet} + H \xrightarrow{k_1} SiH\,, \qquad \textbf{(3)}$$

$$2H \xrightarrow{k_2} H_2\,. \qquad \textbf{(4)}$$

In Reaction (3), the interface trap combines with hydrogen to form a passivated SiH group. Reaction (4) describes hydrogen dimerization, which occurs in the oxide bulk.

Trap production occurs through thermal dissociation, as in the molecular case, and so it is not limited by the hydrogen concentration. The desorption reaction can be written

$$SiH \xrightarrow{k_{-1}} Si^{\bullet} + H\ . \qquad \textbf{(5)}$$

As reactions (3), (4), and (5) will proceed concurrently, one can write

$$[SiH] = [SiH]_0 + [Si^{\bullet}]_0 - [Si^{\bullet}], \qquad \textbf{(6)}$$

where the subscript denotes initial values at $t = 0$ and the square brackets denote concentration. From Ref. [9], the coupled differential equations for $[Si^{\bullet}]$ and $[H]$ are

$$\frac{d}{dt}[Si^{\bullet}] = -k_1[Si^{\bullet}][H] + k_{-1}\left([Si^{\bullet}]_0 + [SiH]_0 - [Si^{\bullet}]\right), \qquad \textbf{(7)}$$

$$\frac{d}{dt}[H] = \frac{d}{dt}[Si^{\bullet}] - 2k_2[H]^2\,. \qquad \textbf{(8)}$$

These equations need to be solved numerically. For a given initial trap density, there are four parameters to determine: the three rate constants k_1, k_2 and k_{-1}, and the initial hydrogen concentration $[H]_0$. Each is described by an Arrhenius expression: $k_1 = k_{1_0} \exp(-E_1 / kT)$; $k_2 = k_{2_0} \exp(-E_2 / kT)$; $k_{-1} = k_{-1_0} \exp(-E_{-1} / kT)$; and $[H]_0 = k_{[H]_0} \exp(-E_{[H]_0} / kT)$. The number of parameters to be determined is reduced to three, because k_1 and k_2 are not independent.[1] This is because Reactions (3) and (4) are expected to have essentially no intermediate energy barrier,[10] and so the reaction rate is limited by the supply of hydrogen. For a diffusion-limited reaction, from bimolecular reaction rate theory[1]

$$k_1 = 2\eta k_2, \qquad \textbf{(9)}$$

where η is a constant dependant on the reaction radii. Since

$$k_1 = 2\pi \rho_1 D_H, \qquad \textbf{(10)}$$

and

$$k_2 = 4\pi \rho_2 D_H, \qquad \textbf{(11)}$$

$$\eta = \frac{\rho_1}{4\rho_2} = \frac{r_H + r_{Si\bullet}}{4(r_H + r_H)}. \qquad \textbf{(12)}$$

where ρ_1 and ρ_2 are the reaction radii, r_H is the radius of a hydrogen atom, $r_{Si\bullet}$ is the capture radius of an interface trap. η was determined by Reed *et al.* to be 0.55. In this chapter, a slightly smaller value of 0.5 was used for simplicity, so that $k_1 = k_2$ (see Equation (9)). [Assuming $r_H = 0.05$ nm, this gives a reasonable value for $r_{Si\bullet}$ of 0.15 nm.] D_H is the diffusion coefficient of atomic hydrogen in SiO$_2$ and can be written as

$$D_H = D_0 \exp\left(\frac{-E_a}{k_B T}\right). \qquad \textbf{(13)}$$

Griscom obtained experimental values of $D_0 \sim 10^{-4} cm^2 s^{-1}$ and E_a~0.2 eV,[11] consistent with recent theoretical calculations.[12] Burte *et al.* experimentally obtained an activation energy of

0.28 ± 0.05 eV.[13] Therefore, with these numbers and Equations (10) and (11), k_1 and k_2 should be $\sim 10^{-11} cm^3 s^{-1}$. Assuming the reaction proceeds as $Al + OH \rightarrow AlO + H$ (the oxide is denoted as AlO because the composition is not known), an estimate of the average starting hydrogen concentration can be obtained from the oxide atomic surface concentration,

$$[H]_0 = [OH]/T_{ox} \qquad \textbf{(14)}$$

where $[OH]$ is the hydroxyl surface concentration, and T_{ox} is the thickness of the oxide layer. $[OH]$ is approximately one-third of the total atomic surface concentration ($\approx 10^{15}$ cm^{-2}), since the hydroxyl groups only bond to surface silicon atoms.[1] Thus, for a 1 micron oxide, $[H]_0 \sim 10^{18}$ - 10^{19} cm^{-3}.

6.2.3 Extension to Atomic Hydrogen Model

A Si dangling bond defect is proposed to be passivated in both the atomic hydrogen and molecular hydrogen case. Therefore, as a spread in activation energy was revealed for the molecular case, it is likely that one is present for the atomic case. Introducing a Gaussian spread (summation of $2n+1$ rate constants) into both the passivation and desorption reactions for the atomic case yields

$$\frac{[Si^\bullet]}{N_0} \approx \frac{1}{A^2} \sum_{j=-n}^{j=+n} \sum_{k=-n}^{k=+n} \exp\left(\frac{-j^2 - k^2}{8}\right) f , \qquad \textbf{(15)}$$

where f is the solution to the full interaction case (Equations (7) and (8)), and where $k_{1j} = k_{1_0} \exp\left(-(E_1 + \frac{j\sigma_{E_1}}{2})/k_B T\right)$ and $k_{-1k} = k_{-1_0} \exp\left(-(E_{-1} + \frac{k\sigma_{E_{-1}}}{2})/k_B T\right)$ are substituted for k_1 and k_{-1}. However, since passivation by atomic hydrogen is expected to be diffusion limited, the effect of defect morphology on the reactivity should not be significant $(\sigma_{E_1} \approx 0)$. On the other hand, the desorption reaction, which is reaction limited, is still expected to have a spread in activation energy. As such

$$\frac{[Si^{\bullet}]}{N_0} \approx \frac{1}{A}\sum_{k=-n}^{k=+n} \exp\left(-\frac{k^2}{8}\right) f, \qquad (16)$$

where f is the solution to the full interaction case (Equations (7) and (8)), and where $k_{-1k} = k_{-1_0} \exp\left(-(E_{-1} + \frac{k\sigma_{E_{-1}}}{2}) / k_B T\right)$ is substituted for k_{-1}.

6.3 Relating PL to Defect Concentration

The intensity and decay of luminescence from Si nanocrystals was measured using time-resolved PL and used as measure of relative defect concentration, as per the method outlined in §5.3. The details will not be repeated here.

6.4 Experimental Details

6.4.1 Sample Preparation

In this study, 400 keV Si^+ ions were implanted into 1.25 μm SiO_2 layers grown on B-doped (0.1 - 0.3 Ωcm) Czochralski (100) Si by wet thermal oxidation at 1100 °C. The samples were implanted to a fluence of 2×10^{17} cm^{-2} at room-temperature, corresponding to a peak excess Si concentration of 10 at. % at a mean projected range of 630 nm, calculated using SRIM.[14] Nucleation and growth of nanocrystals was achieved by annealing the implanted samples in a quartz-tube furnace at 1100 °C for 1 hour in flowing high-purity Ar.

Molecular hydrogen passivation was achieved by thermal annealing in flowing high-purity forming gas (5 % H_2 in N_2). A rapid thermal processor (AET Thermal RX) was used for annealing times ≤ 10 minutes, with longer anneals performed in a conventional tube furnace.

The *alneal* process consisted of thermally evaporating a 100 nm layer of Al onto the oxide surface prior to thermal annealing in N_2 or forming gas. Samples were annealed at temperatures in the range of 200 to 600 °C. The Al layer was subsequently removed by etching in 90 °C H_3PO_4 (85 %) for 1 minute. The etching step was previously found to have no effect on the PL.[5]

The hydrogen desorption anneals were performed in a N_2 environment, after the samples were first passivated with either H_2 or H. Specifically, 500 °C for 1 hour in forming gas or 400 °C for 30 minutes in N_2 after the evaporation of a 100 nm Al layer.

6.4.2 PL and Time-resolved PL

PL measurements were performed at room temperature, using either the 488 nm line of an Ar^+ ion laser or the 532 nm line of a diode pumped solid state laser (frequency-doubled Nd:YAG) as the excitation source. Emitted light was analyzed using a single-grating monochromator (TRIAX-320) and detected with a liquid-nitrogen cooled front-illuminated open-electrode CCD array (EEV CCD30-11). All spectra were corrected for system response.

Time-resolved PL (TRPL) measurements were performed by modulating the laser beam with an acousto-optic modulator (Brimrose TEM-85-10). A room-temperature multialkali photomultiplier (Hamamatsu R928) was used to detect the light from the exit port of the monochromator with the grating centered at 800 nm (band pass of 40 nm). The signal from the photomultiplier was collected using a digital storage oscilloscope. The timing resolution of the system is $< 1\mu s$.

6.5 Experimental Results

6.5.1 Hydrogen Passivation

6.5.1.1 Molecular versus Atomic Hydrogen

Figure 6-3 shows the effect of hydrogen passivation on the nanocrystal PL. There is a significant increase in the PL intensity after annealing in forming gas at 500 °C for 1 hour. These annealing conditions have previously been shown to be optimal for maximizing the PL intensity (see Chapter 5). Extending the annealing time to 16 hours only results in a small increase in intensity over the 1 hour anneal. In contrast, by simply evaporating a layer of Al on the oxide surface before annealing in forming gas, a significant increase in intensity and lifetime (see Figure 6-4) can be achieved.

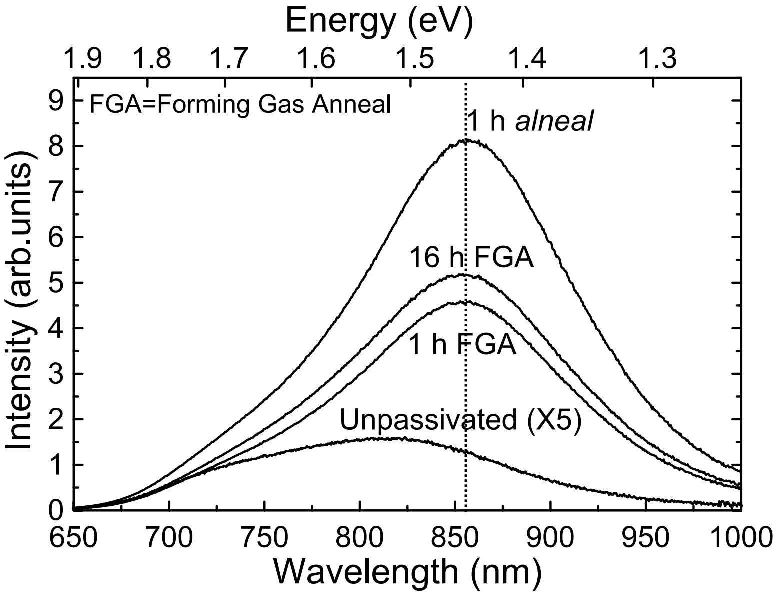

Figure 6-3: PL spectra of Si nanocrystals showing the effect of hydrogen passivation. The passivation anneals were performed at 500 °C. The unpassivated spectrum is multiplied by a factor of 5 for clarity.

Despite the increase in the level of passivation, Figure 6-3 shows that there is no significant red-shift relative to that of samples annealed in forming gas, as indicated by the dotted vertical line. This is in contrast to the initial red-shift relative to the unpassivated sample observed for both the forming gas and *alneal* samples. Such behaviour suggests that passivation may involve more than one class of defects.

TRPL was used to extract the luminescence rise and decay lifetimes by modulating the excitation source. The nanocrystal luminescence decay is characterized by a stretched exponential shape. τ and β are both wavelength dependent and are respectively the lifetime and a dispersion factor whose value is a measure of the interaction strength among Si nanocrystals.

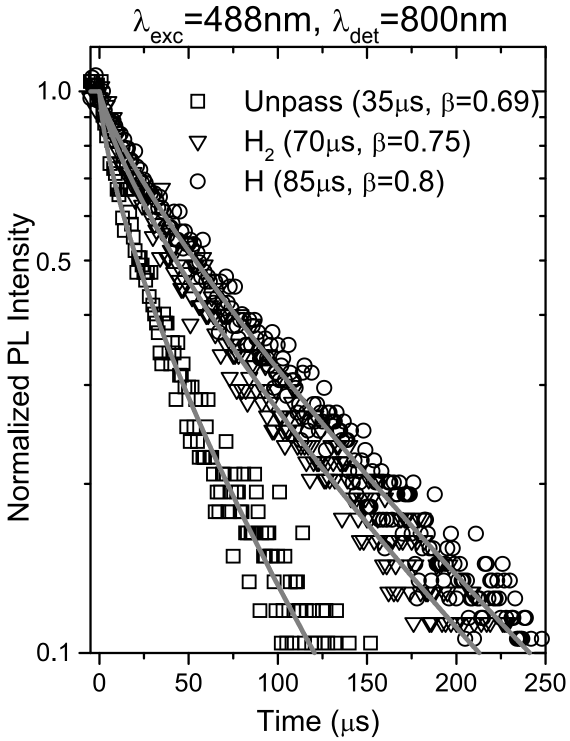

Figure 6-4: PL decay traces from time-resolved PL measurements with stretched exponential fits. The values determined for τ and β are indicated on the figure.

Figure 6-4 shows results from the TRPL measurements. Both τ and β were found to increase with improved passivation. τ can be approximated by $\tau^{-1} = \tau_R^{-1} + \tau_{NR}^{-1}$, where τ_R is the nanocrystal radiative lifetime and τ_{NR} is the non-radiative lifetime. The non-radiative contribution is associated with defects and/or exciton energy migration with other nanocrystals or defects (such as the process involved in luminescence on-off blinking[15]). Consequently, as defects, which act as fast non-radiative recombination states, are inactivated, τ_{NR} increases and τ approaches τ_R. Furthermore, the distribution of lifetimes decreases due to the reduction in exciton migration. This is consistent with the observed increase in τ and β as the degree of passivation improves.

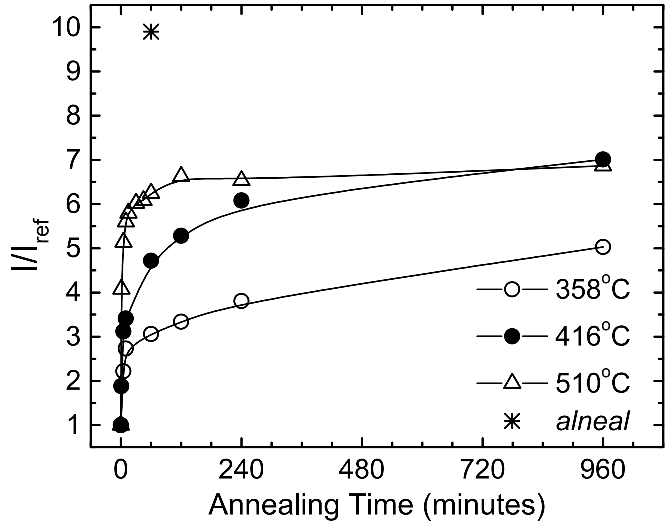

Figure 6-5: PL intensity at 800 nm relative to the reference sample (unpassivated), for samples annealed in forming gas at 358 °C, 416 °C and 510 °C, and after the *alneal* process. The solid lines are provided as a guide to the eye only.

Figure 6-5 shows the PL intensity normalized to the unpassivated sample from isothermal annealing sequences at three temperatures in forming gas. Along with this data is that obtained from the 1 hour *alneal* process. The intensity is taken from the time-resolved PL measurements at 800 nm. This shows that the level of passivation obtainable after a 1 hour *alneal* is not obtainable via annealing in forming gas alone, even after 16 hours.

From the enhancements in intensity and lifetime, we can estimate the increase in the number of luminescent nanocrystals. In the low pump power regime, the PL intensity of the emitting centers can be approximated by $I = \sigma\phi\frac{\tau}{\tau_R}n^*$ where σ is the nanocrystal excitation cross-section, ϕ is the photon flux, τ_R is the radiative lifetime and n^* is the total number of Si nanocrystals that are able to emit. This equation shows that, for constant excitation conditions, a variation in the luminescence yield can only be due to a change in τ or n^* or both, since τ_R and σ are independent of defect effects. This allows the extraction of the relative n^* from the PL intensity and lifetime. The enhancements in intensity and lifetime at 800 nm from the *alneal* compared to forming gas alone are factors of 1.6 and 1.2, respectively. This corresponds to a 30 % increase in the number of luminescent nanocrystals over the optimized 1 hour forming gas anneal. This enhancement, and the fact that similar levels of passivation cannot be achieved with molecular hydrogen, even after 16 hours anneals, implies that a fraction of the non-radiative defects are unable to react with molecular hydrogen. However, electron spin resonance (ESR) measurements suggest that the structure of the residual defects is the same before and after passivation, only the defect density is affected.[7, 16] The difference in reactivity may therefore simply result from different atomic configurations in the vicinity of the defects, with some defects 'sterically protected' from the H_2 molecule but able to react with the smaller H atom.

6.5.1.2 Alneal Kinetic Data

Figure 6-6 shows the effect of annealing environment (FG or N_2) on the passivation kinetics of samples coated with thin Al layer. At 300 °C, passivation by H_2 will proceed slowly (< 20 % passivated after an hour – see Chapter 5). Consequently, the data shows little difference between samples *alnealed* in FG and N_2. The differences here are attributed to experimental uncertainty. Aside from the Al being evaporated on different days, the samples were subjected to identical preparation conditions. The difference is most likely caused by variation in the concentration of –OH radicals in the oxide (and thus hydrogen) available for reaction with the Al layer, due to changes in the ambient humidity.

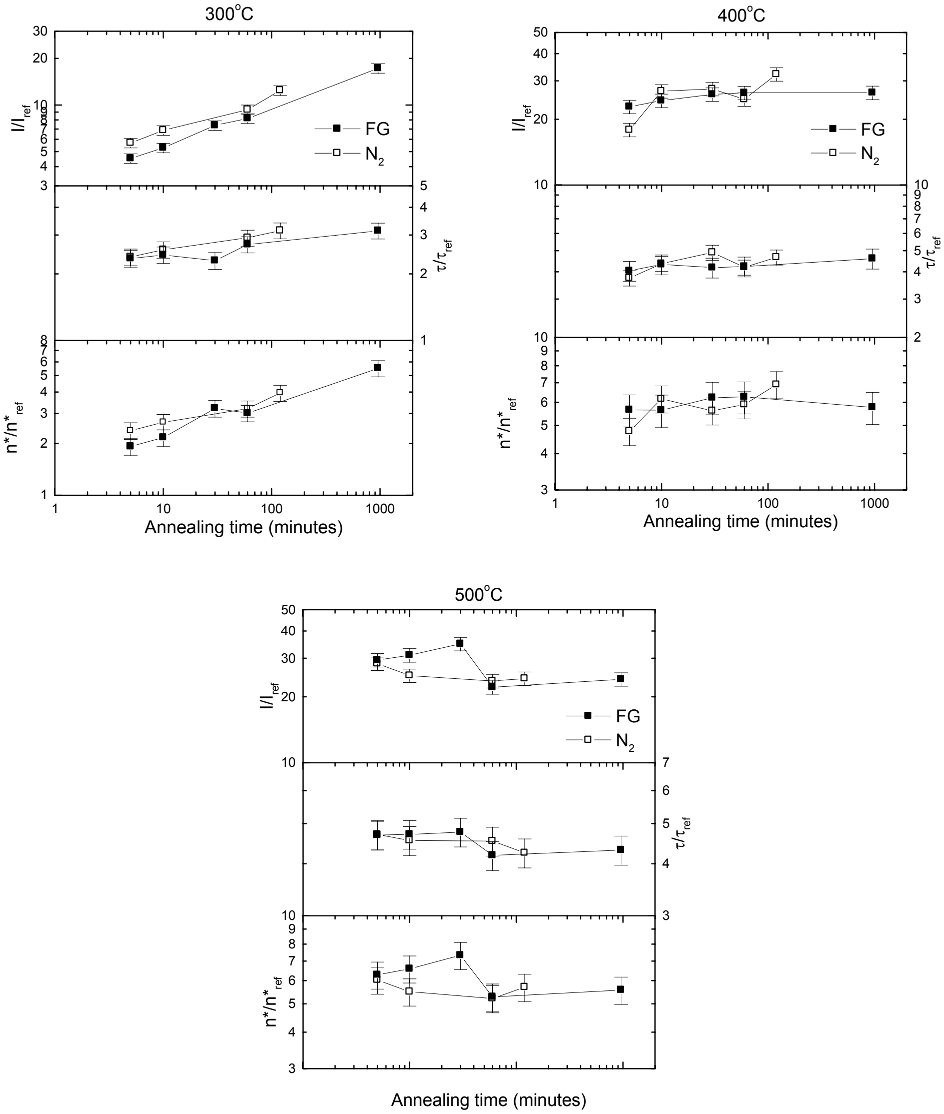

Figure 6-6: Enhancement due to the *alneal* process (1 hour at indicated temperatures) in relative PL intensity, relative PL lifetime and relative number of luminescing nanocrystals determined from TRPL.

At 400 and 500 °C, passivation by H_2 should be significant. However in Figure 6-6, there is little difference seen between annealing the samples in N_2 or FG, even at 500 °C, where the optimum passivation attainable in FG without metallization is achieved. This shows, as reported previously,[1] hydrogen is not required in the annealing environment. The main source of hydrogen is from the *alneal* reaction. Furthermore, the presence of the Al layer appears to lessen the extent of the annealing by H_2 from the environment, indicating that atomic hydrogen passivation is preferential. In other words, the two passivation processes are not simply superimposed, as they would be in a simple competition for the available defects.

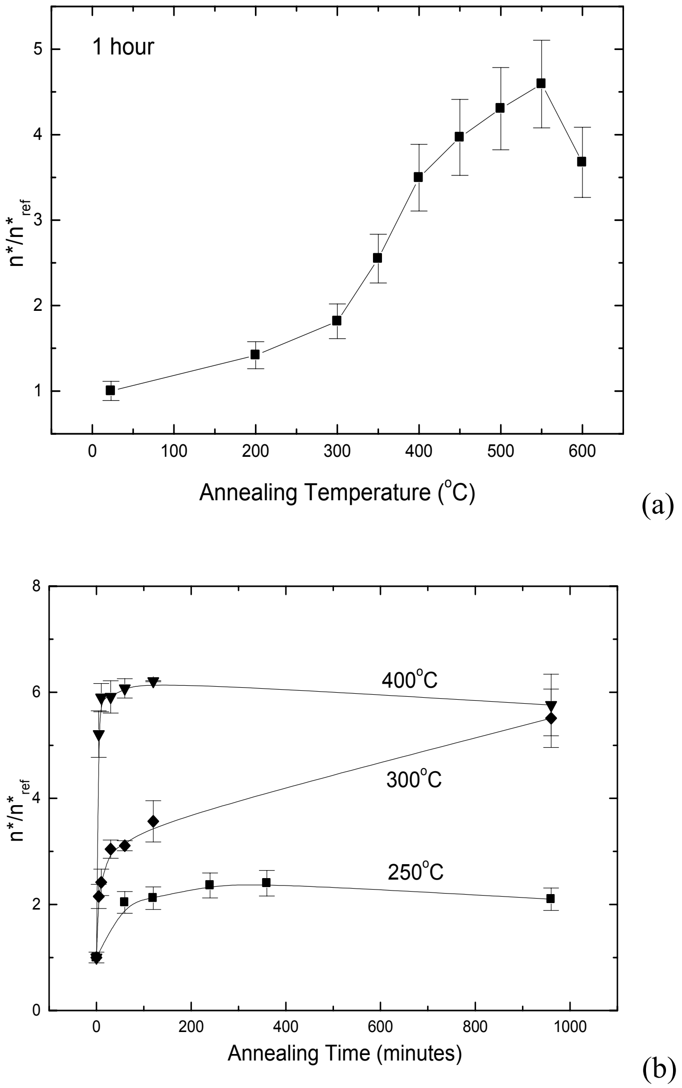

Figure 6-7: Plots of relative number of emitting nanocrystals for *alneals* in N_2. This quantity can be related to the relative defect concentration, which can then be modeled. Data are from TRPL measurements. (a) shows the isochronal data (1 hour), and (b) shows isothermal data.

Figure 6-7 shows the experimental results from time-resolved photoluminescence studies of isochronal (1 hour) and isothermal sets of *alnealed* samples. Figure 6-7(b) shows aggregated data from Figure 6-6 along with an additional isothermal set at 250 °C. This data, which is the enhancement due to passivation of the number of luminescing nanocrystals, can be related to the relative defect concentration and this data is used for modeling the kinetics in §6.6.1.

6.5.2 Hydrogen Desorption

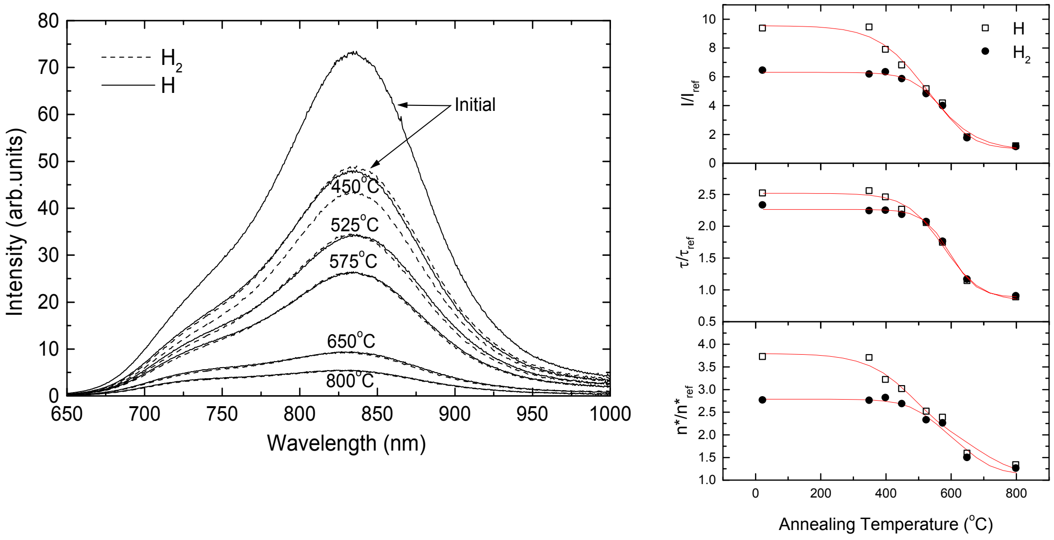

(a)

(b)

Figure 6-8: (a) Nanocrystal PL spectra and (b) TRPL data, initially after passivation in forming gas, and after passivation by *alneal* and after desorption anneals (1 hour) at the temperatures indicated.

A comparison of the depassivation rate for samples passivated in molecular and atomic hydrogen suggests that hydrogen desorbs from the sites passivated by atomic hydrogen more readily than from those passivated by molecular hydrogen. This is illustrated by the data of Figure 6-8(a). For example, after annealing at 525 °C for 1 hour in N_2, the PL intensity from samples passivated in atomic and molecular hydrogen have dropped to a similar level, even though the initial intensity was much higher in the atomic hydrogen case. In other words, the desorption kinetics at 525 °C and above are the same for FG annealed and *alnealed* samples, whereas for temperatures of 450 °C and below, they are different. Figure 6-8(b) shows the TRPL data for these same samples.

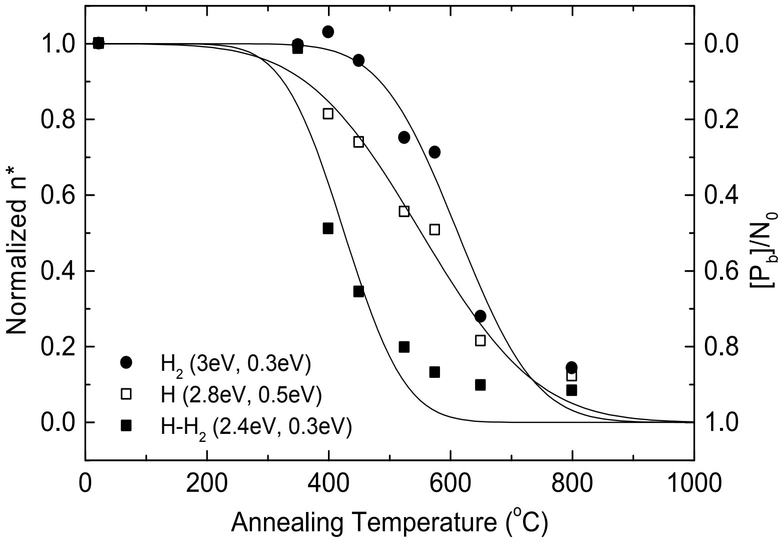

Figure 6-9: Normalized number of emitting nanocrystals, derived from time-resolved PL measurements shown in Figure 6-8(b). The solid lines are fits of the GST model. The desorption activation energy and spread in activation energy for each curve are indicated on the graph.

This difference is further highlighted in Figure 6-9, which shows the normalized number of emitting nanocrystals as a function of temperature during desorption of hydrogen from samples initially passivated in atomic and molecular hydrogen. This quantity is derived from the simple relation: $\frac{n^*}{n^*_{ref}} = \frac{I}{I_{ref}} \frac{\tau_{ref}}{\tau}$. On the assumption that atomic hydrogen passivates both the defects passivated by molecular hydrogen as well as a second class of defects that do not react with molecular hydrogen, the difference between these two curves (before normalization) can be used to isolate the latter contribution. Such analysis is included in Figure 6-9, together with simulations of the two contributions that give desorption activation energies of 3 eV and 2.4 eV for the two defect subsets. The pre-exponential factor for the desorption rate constant was fixed at 2×10^{13} s^{-1} for these fits (the frequency of the Si-H wagging mode[17]).

Confidence in the validity of using PL as a measure of hydrogen/defect concentration is further justified by Heavy-Ion Elastic Recoil Detection (HI-ERD) measurements on PECVD deposited Si-rich SiO_2.[18] These films contain large concentrations of hydrogen (often > 20 at. %), as SiH_4 gas is used as the source of Si in the deposition. The bonding configuration of hydrogen in these samples is unknown, but the similarity of the reaction-rate parameters for these films (Figure 6-10) and desorption from passivated nanocrystals (Figure 6-9) is reassuring. This HI-ERD data set represents the average kinetics (of all bonding configurations) for hydrogen desorption from the sample.

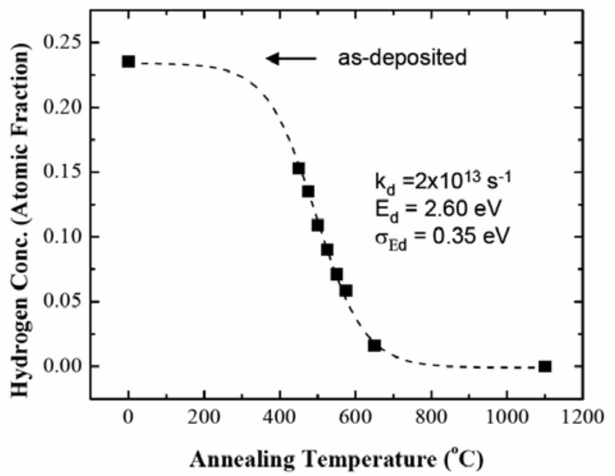

Figure 6-10: Hydrogen concentration of PECVD deposited Si-rich SiO_2, determined from Heavy-Ion Elastic Recoil Detection (HI-ERD) analysis, as a function of annealing temperature.[18] The dashed line shows a fit to the hydrogen desorption equation. The extracted parameters are also shown inset.

Earlier studies have revealed a correlation between the concentration of ESR active P_b defects and molecular hydrogen passivation suggesting that this class of defect is a dominant non-radiative recombination center.[7] However, the results of the present study show that annealing in atomic hydrogen can significantly increase the level of passivation above that achievable with molecular hydrogen. This observation, along with the differences in desorption kinetics (Figure 6-8 and Figure 6-9), supports a model in which more than one class of non-radiative defect is active. Indeed, such a scenario is consistent with work by Gheorghita *et al.*[6] that provided alternative evidence for two classes of defects at the (111)

Si/SiO_2 interface in addition to the P_b defect: one that can be passivated with H_2, and one that cannot.

6.6 Modeling the Passivation Kinetics

6.6.1 Results

Figure 6-11 shows the global least-squares fit of the data. The extracted parameters are shown in Table 6-1 long with those obtained for passivation of planar Si/SiO_2 interfaces by Reed *et al.*[1] Several parameters were fixed at physically reasonable values. The consistency of these numbers with previous work and physical reality are discussed in the next sections.

Table 6-1: Kinetic parameters for thermal passivation in H (*alneal*) and desorption in N_2 of defects at the Si/SiO_2 interface. (For <111> orientation). The underlined parameters were fixed at physically reasonable values or values obtained from the desorption data.

	E_1 (eV)	σ_{E_1} (eV)	k_{1_0} (cm^3s^{-1})	E_{-1} (eV)	$\sigma_{E_{-1}}$ (eV)	k_{-1_0} (s^{-1})	$E_{[H]_0}$ (eV)	$k_{[H]_0}$ (cm^{-3})
Reed *et al.*	0.75	0	1.4×10^{-12}	1.56	0	4.3×10^{6}	0.46	3.3×10^{23}
This work	0.3	0	1×10^{-11}	2.8	0.4	2×10^{13}	1.0	8×10^{18} (a) 1.6×10^{17} (b)

(a) This is the value determined for the isothermal data shown in Figure 6-11(a).
(b) This is the value determined for the isochronal data shown in Figure 6-11(b).

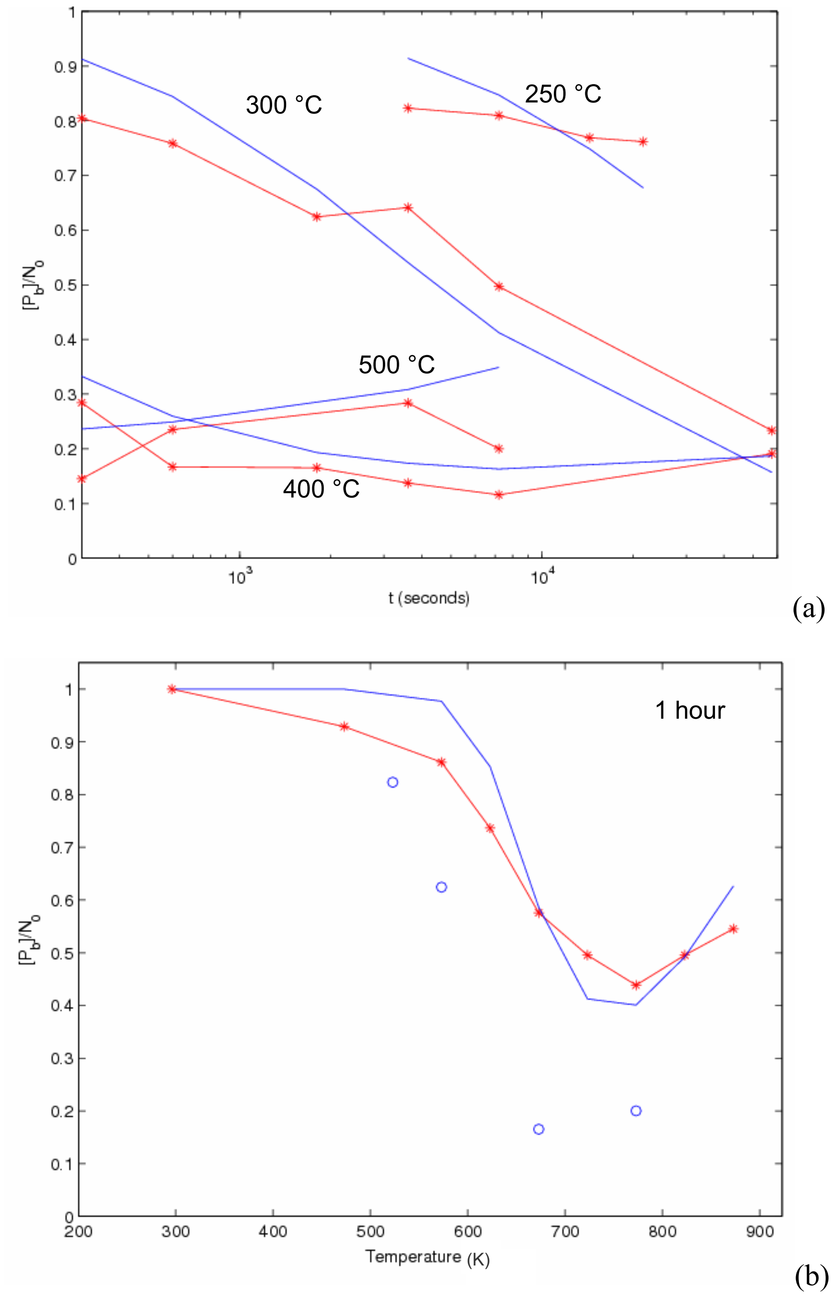

Figure 6-11: Plots of relative P_b concentration versus (a) annealing time and (b) annealing temperature of atomic hydrogen passivation. The solid lines represent the least squares fit of the model to experimental data (joined data points) derived from time-resolved PL measurements. The open circles in (b) is the 1 hour experimental data from (a) plotted again.

6.6.2 Discussion

The proposed model fits the experimental data reasonably well with the values found in Table 6-1 Several parameter values were fixed during the fit. The desorption reaction parameters were fixed at values determined on separate desorption data, as outlined in §6.5.2. The spread in the passivation activation energy was fixed at 0, since the reaction is thought to be diffusion limited and thus the effect of defect morphology should be insignificant. This also means the attempt frequency (for k_1, k_2) should be ~$1\text{x}10^{-11}$ cm^3s^{-1}, from bimolecular theory. The determined E_1 = 0.3 eV agrees with the reported values of atomic hydrogen diffusion in SiO_2.[11-13]

For the hydrogen concentration attempt frequency, there are two values listed in Table 6-1. This is because samples undergoing nominally identical heat treatments showed differences when both data sets are compared (see Figure 6-11(b), where both data sets are displayed). This is expected to be due to differing amounts of hydrogen present in the oxide due to variations in ambient humidity when the Al was deposited. The overall temperature dependence of the passivation reaction is described by $\sim k_1[H]_0$.[1] This evaluates to $k_1[H]_0 = 8\times10^7\exp(-1.3/kT)$ and $k_1[H]_0 = 1.6\times10^6\exp(-1.3/kT)$ for the two different hydrogen concentrations. The initial concentrations of hydrogen are feasible when compared to the estimations based on Equation (14).

The activation energy for the *alneal* reaction was determined to be 1 eV. The proposed reaction is $2Al + 3OH \rightarrow Al_2O_3 + 3H$, assuming stoichiometric alumina is produced. Using the values shown in Table 6-2, reaction is calculated to be exothermic by 1.1 eV [$\Delta_r H^0 = \sum \Delta_f H^0_{prod} - \sum \Delta_f H^0_{react}$ = -1.1 eV]. However, without knowing the transition state the activation energy cannot be determined. What can be said is that the proposed model for passivation by atomic hydrogen adequately describes the experimental results. Due to the nature of fitting procedures, it is unwise to place too much credence on the exactness of the values determined when comparisons to physical reality cannot be made.

Table 6-2: Standard enthalpies of formation at 298.15K.[19]

Substance	State	$\Delta_f H^0$ (kJ/mol)
Al_2O_3	Amorphous	-1603.5 [20]
H	Gaseous	218.0
OH	Gaseous	39.0
Al	Crystalline	0.0

6.6.3 Reed and Plummer's Results:[1]

Although the extended model (see §6.2.3) fits the data, the parameters found in this work for the passivation kinetics of Si nanocrystals do not agree completely with the results previously found for planar interfaces and atomic hydrogen (see Table 6-1). However, differences are not unexpected due to the inclusion of a spread in the desorption activation energy. Furthermore, the values previously determined by Reed *et al.* are, on the whole, not reconciled with physically predicted values. First, the reverse reactions (k_{-1}) have pre-exponential factors many orders of magnitude lower than predicted for the frequency of the Si-H wagging mode (2×10^{13} s^{-1}). The activation energies are also lower than expected, with many references reporting desorption energies at values closer to 3 eV.[21] On the other hand, the pre-exponential factors for k_1 and k_2 have values that are relatively close to 10^{-11} cm^3s^{-1}, as predicted by bimolecular theory. However, the activation energies are several times higher than the predicted diffusion activation energy. Since the annealing rate is governed by $k_2[H]_0$, it is possible that the $[H]_0$ activation energy is underestimated, which could then account for the higher activation energy found for k_2. Last, an upper limit on the hydrogen concentration of $[H]_0 = 10^{20}$ cm^{-3} was derived for their sample structures. However, the pre-exponential factor determined for $[H]_0$ is three orders of magnitude higher.

6.7 Concluding Remarks

Time-resolved photoluminescence was used to study the passivation and desorption kinetics of non-radiative defects in silicon nanocrystals annealed in molecular and atomic hydrogen. Annealing in atomic hydrogen was shown to result in greater levels of passivation than were achievable with molecular hydrogen under optimal conditions. This suggested the presence of at least two classes of non-radiative defect: one that reacts with both atomic and molecular hydrogen, and a second that reacts only with atomic hydrogen. This interpretation was supported by hydrogen desorption data that showed a lower activation energy for desorption from sites passivated with atomic hydrogen (E_a = 2.4 eV) than for those passivated with molecular hydrogen (E_a = 3.0 eV).

The defect passivation kinetics were modeled using a modification of a model originally developed by Reed *et al.* for atomic hydrogen passivation of defects Si/SiO_2 planar interfaces. After the addition of a Gaussian spread in activation energy, the model was found to adequately describe the passivation kinetics. Furthermore, the reaction-rate parameters extracted are physically reasonable.

6.8 References

[1] M. L. Reed and J. D. Plummer, J. Appl. Phys. **63**, 5776 (1988).

[2] E. H. Poindexter and P. J. Caplan, Prog. Surf. Sci **14**, 201 (1983).

[3] P. Balk, in *Proceedings of the Electrochemical Society Fall Meeting* (Electrochemical Society, Buffalo, NY, 1965), p. 29.

[4] M. J. Kerr and A. Cuevas, Semicond. Sci. Technol. **17**, 35 (2002).

[5] A. R. Wilkinson and R. G. Elliman, Appl. Phys. Lett. **83**, 5512 (2003).

[6] L. Gheorghita and E. Ogryzlo, J. Appl. Phys. **87**, 7999 (2000).

[7] A. Stesmans, J. Appl. Phys. **88**, 489 (2000).

[8] A. R. Wilkinson and R. G. Elliman, Phys. Rev. B **68**, 155302 (2003).

[9] M. L. Reed and J. D. Plummer, Appl. Phys. Lett. **51**, 514 (1987).

[10] K. L. Brower and S. M. Meyers, Appl. Phys. Lett. **57**, 162 (1990).

[11] D. L. Griscom, J. Appl. Phys. **58**, 2524 (1985).

[12] B. Tuttle, Phys. Rev. B **61**, 4417 (2000).

[13] E. P. Burte and P. Matthies, IEEE Trans. Nucl. Sci. **35**, 1113 (1988).

[14] J. F. Ziegler, J. P. Biersack, and U. Littmark, *The Stopping and Range of Ions in Solids* (Pergamon Press, New York, 1985).

[15] I. Sychugov, R. Juhasz, J. Linnros, et al., Phys. Rev. B **71**, 115331 (2005).

[16] M. López, B. Garrido, C. García, et al., Appl. Phys. Lett. **80**, 1637 (2002).

[17] B. B. Stefanos, A. B. Gurevich, M. K. Weldon, et al., Phys. Rev. Lett. **81**, 3908 (1998).

[18] R. G. Elliman, T.D.M. Weijers-Dall, M. G. Spooner, et al., accepted to Nucl. Instr. and Meth. B (2005).

[19] *CRC Handbook of Chemistry and Physics* (Chemical Rubber, Boca Raton, Florida, 1992).

[20] J. M. Wu, Materials Letters **48**, 324 (2001).

[21] A. Stesmans, Phys. Rev. B **61**, 8393 (2000).

CHAPTER

7

The Effect of Annealing Temperature and Hydrogen Passivation on the Sensitization of Erbium in Silicon-rich Silica

This chapter reports on the effect of annealing temperature and hydrogen passivation on the excitation cross-section and photoluminescence of erbium in silicon-rich silica. Samples are prepared by co-implantation of Si and Er into SiO_2 followed by a single thermal anneal at temperatures ranging from 800 to 1100 °C, and with or without hydrogen passivation performed at 500 °C. Using time-resolved photoluminescence, the effective erbium excitation cross-section is shown to increase by a factor of 3, while the number of optically active erbium ions decreases by a factor of 4 with increasing annealing temperature. Hydrogen passivation is shown to increase the luminescence intensity and to shorten the luminescence lifetime at 1.54 μm only in the presence of Si nanocrystals. The implications of these results for realizing a silicon-based optical amplifier are also discussed.

7.1 Introduction

Erbium (Er)-doped Si-rich SiO_2 layers have shown promise as an efficient room temperature emitter at 1.54 μm. The Si nanocrystal mediated energy transfer offers an effective excitation cross section of $\sim 10^{-16}$ cm^2 over a broad energy range, much higher than the direct, resonant excitation cross section for Er in SiO_2 (10^{-21} - 10^{-19} cm^2).[1] There are many reports exploring the preparation conditions for optimum light emission at 1.54 μm.[2, 3] Of particular interest was the observation of high luminescence intensity from Er^{3+} ions at low annealing temperatures (800 °C) in silicon-rich oxide samples fabricated by plasma-enhanced chemical vapor deposition (PECVD).[4] At this temperature amorphous Si nanoclusters are formed rather than Si nanocrystals, thereby suggesting that well-defined nanocrystals are not required for effective sensitization. Also of interest is the observation that hydrogen passivation has a significant effect on the light emission from Si nanocrystals by inactivating non-radiative recombination channels.[5] It might therefore be expected that hydrogen passivation will affect the energy transfer between nanocrystals and Er. Indeed, an increase in Er photoluminescence (PL) has been reported after hydrogen passivation of PECVD samples.[6]

The motivation for the present investigation is the possibility of realizing a silicon-based optical amplifier operating at 1.54 μm. Although signal enhancement has been reported for Er-doped Si-rich oxides[7] this is inconsistent with the results of other groups, which have reported only induced absorption.[8, 9] In recent experiments, it was demonstrated that a reduction of losses (or induced absorption due to confined carriers within the nanocrystals) could be achieved for samples annealed at temperatures below that required for the formation of well-defined Si nanocrystals.[9] Although a semi-permanent absorption was observed in such samples, it is believed that this can be practically reduced by optimizing the sample preparation conditions. Indeed, reduced losses and a concomitant increase in Er PL intensity in samples annealed at temperatures below 1000 °C offers one of the most promising paths towards the observation of net gain. However, before any practical implementation is discussed, it is important to understand the effect of the preparation conditions on the nanocrystal-Er interaction. Specifically the energy transfer rate, the excitation cross section, and the number of optically active Er^{3+} ions.

Previous studies have examined the excitation cross section of Si nanocrystals,[10] and the cross section of Er in SiO_2[11] and c-Si[12] under optical pumping. The effective excitation cross section of Er in Si-rich oxide has also been studied as a function of annealing temperature for samples prepared by reactive magnetron sputtering.[13] Here we investigate the effective excitation cross section of Er in Si-rich SiO_2, the relative number of optically active Er ions and the effective energy transfer rate for samples prepared by ion implantation, annealed at different temperatures, with and without hydrogen passivation.

7.2 Experimental Details

7.2.1 Sample Preparation

SiO_2 layers of 1.25 μm thickness were grown on B-doped Cz (100) silicon and co-implanted with Si^- and Er^+ ions. The implant conditions were 100 keV Si^- to a fluence of 10^{17} Si/cm^2 and 500 keV Er^+ to a fluence of 10^{15} Er/cm^2, at room temperature. The peak concentration of Er was ~10^{20} cm^{-3}, with the energies chosen so that the peak of each implantation profile overlapped, calculated using SRIM.[14] Samples were subsequently annealed for 1 h in flowing N_2 in the temperature range from 800 to 1100 °C. Hydrogen passivation anneals were performed in flowing forming gas (5 % H_2 in N_2) for 1 h at 500 °C.

7.2.2 PL and Time-resolved PL

PL measurements were performed at room temperature, using the 488 nm line of an Ar^+ ion laser as the excitation source. The excitation power was controlled using a graded neutral density filter and a calibrated power meter (Newport). The spot size was kept constant (~3 mm diameter), with the area calculated with image processing software from digital images of the laser spot at the sample. The laser beam was mechanically chopped at a frequency of 20 Hz. The luminescence signal was collected by two plano-convex lenses and focused onto the aperture of a single grating monochromator (TRIAX-320).

The Er photoluminescence spectra were detected by a liquid-nitrogen cooled Ge detector (Applied Detector Corporation) using standard lock-in techniques, while time-resolved measurements were directly recorded by a digital oscilloscope. The overall time resolution of the system was ~0.2 ms.

The nanocrystal photoluminescence spectra were detected with a liquid-nitrogen cooled CCD for continuous PL measurements. Time-resolved PL measurements were performed by modulating the laser beam with an AOM (typically at 400 Hz). A room-temperature multi-alkali PMT was used to detect the light from the exit port of the monochromator with the grating centred at 800 nm. The signal from the PMT was collected using a digital storage oscilloscope.

7.3 Power Dependence Theory

The excitation cross-section of Si nanocrystals and the effective excitation of Er can be determined through power dependence measurements. The PL intensity is in general given by,[1]

$$I_{PL} \propto \frac{N^*}{\tau_R}, \qquad (1)$$

where N^* is the concentration of excited emitters and τ_R the radiative lifetime.

The rate equation for nanocrystal excitation is

$$\frac{dN^*}{dt} = \sigma\phi(N - N^*) - \frac{N^*}{\tau}, \qquad (2)$$

σ being the excitation cross section, ϕ the photon flux, N the total number of nanocrystals, and τ the decay lifetime, where $\frac{1}{\tau} = \frac{1}{\tau_{NR}} + \frac{1}{\tau_R}$ (τ_{NR} is the non-radiative lifetime). Under steady-state pumping ($\frac{dN^*}{dt} = 0$), Equation (2) yields

$$N^* = N\frac{\sigma\phi\tau}{\sigma\phi\tau + 1}. \qquad (3)$$

Combining this with Equation (1) gives

$$I_{PL} \propto \frac{N}{\tau_R}\frac{\sigma\phi\tau}{\sigma\phi\tau + 1}. \qquad (4)$$

For pulsed-excitation, according to Equations (1) and (2), if a pumping laser pulse is turned on at $t=0$ the PL intensity will increase by the following law

$$I(t) = I_0\left\{1 - \exp\left[-\left(\sigma\phi + \frac{1}{\tau}\right)t\right]\right\}, \qquad (5)$$

with I_0 being the steady state PL intensity. Therefore, the rise time can be written as

$$\frac{1}{\tau_{on}} = \sigma\phi + \frac{1}{\tau}. \qquad (6)$$

Therefore, the nanocrystal excitation cross section can be determined experimentally by varying the excitation photon flux, according to Equations (4) or (6).

The effective excitation cross-section of Er can be determined in steady-state measurements, from Kenyon *et al.*[15]

$$N^*_{RE} = \frac{(1-C_{dir})N_{RE}\eta\phi\left(\dfrac{\sigma_{eff}}{\sigma\tau\phi+1}\right) + C_{dir}\sigma_{Er}N_{RE}}{(1-C_{dir})\phi\left(\dfrac{\sigma_{eff}}{\sigma\tau\phi+1}\right) + C_{dir}\sigma_{Er}\phi + \dfrac{1}{\tau_{off}}} \times\left(1 - \exp\left\{-\left[(1-C_{dir})\phi\left(\frac{\sigma_{eff}}{\sigma\tau\phi+1}\right) + C_{dir}\sigma_{Er}\phi + \frac{1}{\tau_{off}}\right]t\right\}\right) \qquad (7)$$

where C_{dir} is proportion of direct Er excitation ($0 \le C_{dir} \le 1$), N^*_{RE} is the concentration of excited Er ions, N_{RE} is the concentration of Er ions, η is the quantum efficiency of Er being excited into the metastable state, σ_{Er} is the direct optical excitation cross section, σ_{eff} is the effective Er excitation cross section, σ is the nanocrystal excitation cross section, τ is the nanocrystal exciton lifetime, and τ_{off} is the decay lifetime for the Er^{3+} metastable state. With $C_{dir}=0$ (nanocrystal mediated excitation only), the intensity can be written as

$$I_{PL} \propto \frac{N_{RE}\eta}{\tau_R^{RE}} \frac{\phi\left(\dfrac{\sigma_{eff}\tau_d^{RE}}{\sigma\tau\phi+1}\right)}{\phi\left(\dfrac{\sigma_{eff}\tau_d^{RE}}{\sigma\tau\phi+1}\right)+1}, \qquad (8)$$

and for pulsed excitation,

$$\frac{1}{\tau_{on}} = (1-C_{dir})\phi\left(\frac{\sigma_{eff}}{\sigma\tau\phi+1}\right) + C_{dir}\sigma_{Er}\phi + \frac{1}{\tau_d^{RE}}, \qquad (9)$$

with $C_{dir}=0$

$$\frac{1}{\tau_{on}} = \phi\left(\frac{\sigma_{eff}}{\sigma\tau\phi+1}\right)+\frac{1}{\tau_d^{RE}}. \qquad (10)$$

7.4 Experimental Results

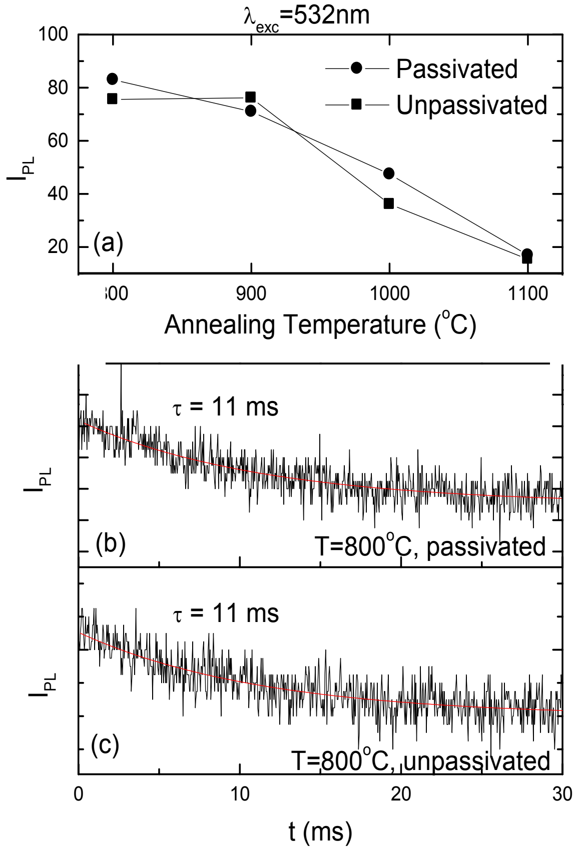

Figure 7-1: Er PL intensity (arbitrary units) as a function of annealing temperature after and before passivation (a) and decay lifetime of sample annealed at 800 °C after (b) and before (c) passivation, measured at room temperature. The PL decay lifetime (~11 ms) and intensity are not significantly affected by hydrogen passivation. The sample contains 1×10^{20} Er/cm^3 in stoichiometric SiO$_2$, and was excited directly at 532 nm.

Figure 7-2 shows the PL intensity and decay lifetime at 1.54 μm as a function of the annealing temperature before and after hydrogen passivation for an excitation photon flux of 2.1×10^{18} cm^{-2}s^{-1}. Also shown inset is the PL intensity for the same Er implant in SiO$_2$, excited with a 532 nm source to induce some direct excitation of the Er. In both cases the PL intensity is observed to decrease with increasing annealing temperature (see Figure 7-2(a)). This is attributed to a reduction in the concentration of optically active Er due to precipitation. [We note that our samples contain a high Er concentration (10^{20} cm^{-3}) where precipitation has been previously observed for annealing temperatures above 900 °C in SiO_2.][11] Figure 7-2(a) also shows a small enhancement in the Er PL intensity after hydrogen passivation. This is consistent with previous reports where such behavior was attributed to a reduction in the concentration of non-radiative defects.[6] Hydrogen passivation was not found to have any significant effect on the Er PL intensity of lifetime of the Er only samples (see Figure 7-1).

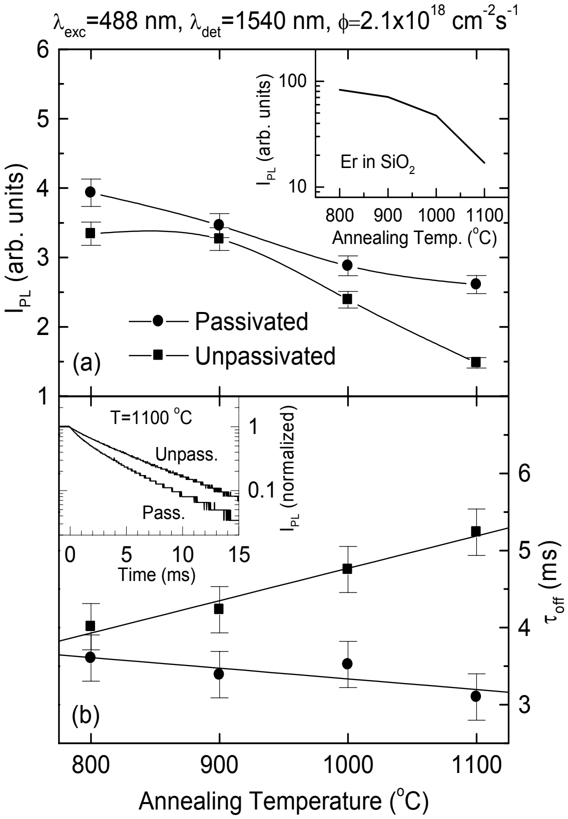

Figure 7-2: Er luminescence intensity (a) and decay lifetime (b) before and after hydrogen passivation measured at 1.54 μm. The inset in (a) shows the case of Er only in SiO_2, i.e. direct excitation at 532 nm (reproduced from Figure 7-1(a)). The solid lines are included as a guide to the eye only. The inset in (b) shows typical PL decay curves after normalization, before and after passivation, for the sample annealed at 1100 °C.

Figure 7-2(b) shows the effective decay lifetime of Er^{3+} ions obtained from stretched-exponential fits to the PL decay curves (typical PL decay curves are shown in the inset). For passivated samples the decay lifetime was found to be shortened relative to that for unpassivated samples. This shortening is in contrast to the effect of passivation on the Si nanocrystal emission where the lifetime is found to increase due to the suppression of non-radiative recombination.[5] Indeed, even in the presence of erbium, the Si nanocrystal lifetime measured at 800 nm was found to increase from 22 µs to 37 µs for a sample annealed at 1100 °C (see Figure 7-3). However, based on the volume fraction of Si in SiO_2 one would expect about 15% of the Er to be incorporated within[16] or segregated by the nanocrystals.[17] For this fraction of the Er lying within or near defective nanocrystals, the emission is likely to be suppressed by fast non-radiative recombination. Hydrogen passivation of these defective nanocrystals would then be expected to increase the emission from the Er. The lifetime of the emission from the Er either completely within nanocrystals or at the nanocrystal/SiO_2 interface would be shorter than that for Er incorporated in stoichiometric SiO_2 (somewhere between the lifetime of Er in Si and Er in SiO_2). Therefore after hydrogen passivation, the contribution of this fraction of Er would both increase the intensity and shorten the lifetime of the Er PL measured overall. This model is further supported by the fact that passivation has a greater effect at higher annealing temperatures where the volume fraction of nanocrystals is larger.

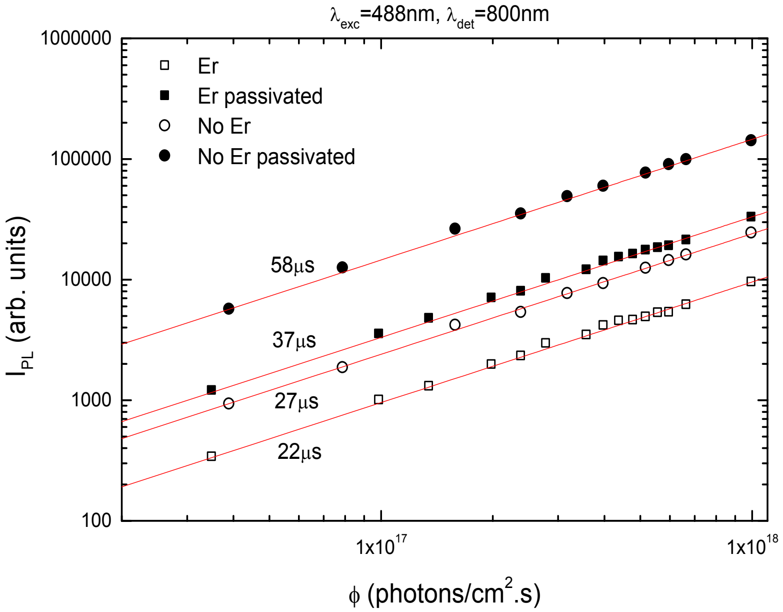

Figure 7-3: Variation of nanocrystal PL intensity measured at 800 nm with excitation photon flux. The PL decay lifetimes are also indicated on the figure.

Kenyon *et al.*[15] have shown that the effective Er excitation cross section (σ_{eff}) can be related to the lifetime data through,

$$\frac{1}{\tau_{on}} = \phi\left(\frac{\sigma_{eff}}{\sigma\tau\phi+1}\right)+\frac{1}{\tau_{off}} \tag{11}$$

where ϕ is the photon flux, τ_{on} and τ_{off} are the rise and decay lifetimes of the Er luminescence, σ_{eff} and σ are the effective Er and nanocrystal excitation cross sections, and τ is the decay lifetime of the nanocrystal luminescence (exciton lifetime). σ_{eff} can be written as

$$\sigma_{eff} = \sigma\tau R_{transfer} = \sigma\tau\frac{kN\Lambda}{\tau_{tr}} \tag{12}$$

where $R_{transfer}$ is the effective transfer rate, N is the nanocrystal concentration, Λ is the interaction volume, k is the average number of excitons per nanocrystal, and τ_{tr} is the transfer time. This is assuming the contribution from direct Er excitation is insignificant at 488 nm, which was confirmed experimentally. The formulation described in Equation (11) includes upconversion, whereby an Er ion in the metastable state is excited to higher energy states by transfer from excitons and therefore does not contribute to the emission process.

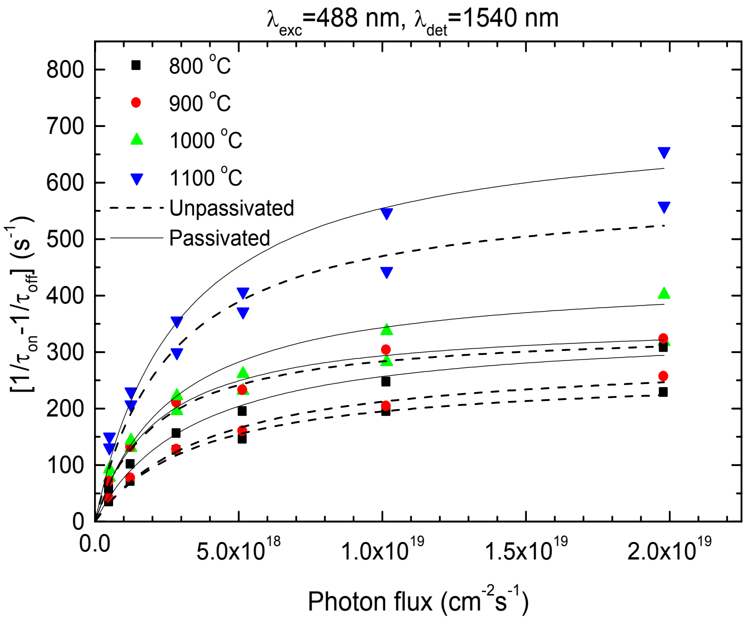

Figure 7-4: Variation of the difference in excitation and decay rates of 1.54 μm emission as a function of the incident photon flux (ϕ), for different annealing temperatures before and after hydrogen passivation. The lines are least squares fits of Equation (11).

Figure 7-4 shows the pump power dependence of the luminescence intensity before and after passivation. In this figure, $\left(\frac{1}{\tau_{on}} - \frac{1}{\tau_{off}}\right)$ is plotted versus photon flux along with least-squares fits of Equation (11). The response is non-linear, most-likely due to the saturation of optically active Er ions or other competing processes such as upconversion.[2] From Equation (12) and these fits it is possible to estimate σ_{eff} and $R_{transfer}$, which are plotted in Figure 7-5(a) and Figure 7-5(b), respectively.

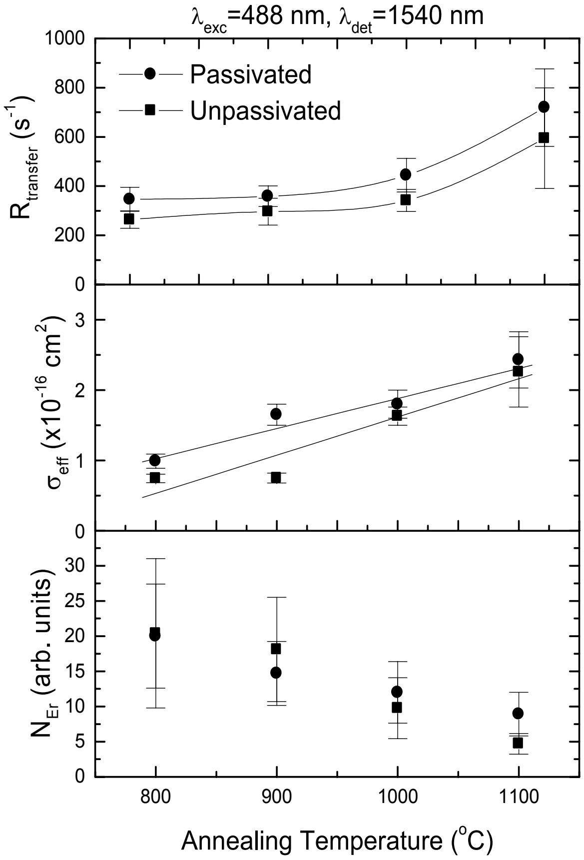

Figure 7-5: The effective transfer rate, $R_{transfer}$ (a), effective excitation cross-section, σ_{eff} (b), relative number of optically active erbium concentration (c) versus annealing temperature, before and after hydrogen passivation.

The relative number of optically active Er ions can then be extracted from the data in Figure 7-2, Figure 7-5(a), and Figure 7-5(b) using the following equation:

$$I_{PL} \propto \frac{N_{Er}\eta}{\tau_R}\frac{\sigma_{eff}\tau_{off}\phi}{\sigma\tau\phi+1}\left(\frac{\sigma_{eff}\tau_{off}\phi}{\sigma\tau\phi+1}+1\right)^{-1} \qquad (13)$$

where N_{Er} is the concentration of optically active Er, τ_R is the radiative lifetime of excited Er and η is the quantum efficiency of the filling of the Er metastable state.[15] The results are shown in Figure 7-5(c).

The data presented in Figure 7-5 show an increase in both the effective transfer rate and excitation cross section, and a decrease in the fraction of optically active Er with increasing annealing temperature. The effective transfer rate and excitation cross section are further increased by hydrogen passivation. In other words, higher annealing temperatures and passivation are desirable for efficient energy transfer. However the accompanied precipitation of Er reduces the number of optically active ions for high annealing temperatures. (Samples containing 10^{19} Er/cm^3 were also measured and did not show a decrease in intensity with annealing temperature. However, the PL intensity was considerably lower than for the higher Er concentration at low annealing temperatures.) Moreover losses caused by induced absorption (due to confined carriers within the nanocrystals) also increase with annealing temperature.[9] Process optimisation therefore requires a compromise between the optically active Er concentration, efficient Er excitation, and excited state absorption.

Finally, the specific implications of this work for achieving optical gain are discussed. The gain coefficient, γ [cm^{-1}], can be expressed as:

$$\gamma = \Delta N \times \sigma = \frac{\Delta N \lambda^4}{4\pi^2 n^2 c \tau_{sp} \Delta\lambda} \qquad (14)$$

where σ is the transition cross section, ΔN is the number of optically active erbium in its excited state, λ is the emission wavelength, n is the refractive index in the medium, c is the speed of light, τ_{sp} is the spontaneous emission lifetime and $\Delta\lambda$ is the emission linewidth.[18] For the case of Er^{3+} in silica fibers one can assume the following parameters: $\lambda = 1.54\mu$m, $n = 1.46$, $\tau_{sp} = 10$ ms, $\Delta\lambda = 35$ nm (inhomogeneous and homogeneous broadening), and $\Delta N = 2\times10^{19}$ cm^{-3}. Using these values one obtains ~0.13 cm^{-1}, corresponding to a 0.6 dB gain value in a 1 cm fiber. Because the losses in silica fibers at 1.54 μm are small, large gain values can be achieved by increasing the length of the active region. However, the losses will be greater in waveguides containing nanocrystals, due to Mie scattering, nanocrystal absorption and confined carrier absorption. Assuming losses of the order of 10 dB in a 1 cm waveguide (γ = 2.3 cm^{-1}) ,[19] while considering now n = 1.6 and τ_{sp} = 5 ms in the presence of nanocrystals, and assuming the same $\Delta\lambda$ (experimentally confirmed) we require $\Delta N = 2.2\times10^{20}$ cm^{-3} (Equation (14)). This value is the minimum concentration (assuming 50 % ions in the excited state) to achieve positive gain. Thus requiring the total number of optically active erbium ions to be $N = 4.4\times10^{20}$ cm^{-3}, assuming all incorporated ions are optically active. In light of the results in Figure 7-5, achieving a high N while balancing other demands for low loss propagation is not straightforward.

7.5 Concluding Remarks

In conclusion, experimental data has been presented on the effect of annealing temperature and hydrogenation on the sensitization of Er in Si-rich SiO_2. The effective excitation cross section was found to increase by a factor of 3 over the annealing range (800 - 1100 °C). However, the PL intensity was shown to decrease, which was attributed to the precipitation of Er due to the Er high concentration (10^{20} cm^{-3} peak). Hydrogen passivation was found to effect the Er PL in the presence of Si nanocrystals, by increasing the intensity and shortening the lifetime. The lifetime shortening was attributed to the fraction of Er inside nanocrystals or at the nanocrystal interface contributing significantly to the PL only after passivation. Ultimately process optimization requires a compromise between optically active Er concentration, efficient Er excitation, and excited state absorption.

7.6 References

[1] F. Priolo, G. Franzò, D. Pacifici, et al., J. Appl. Phys. **89**, 264 (2001).

[2] D. Pacifici, G. Franzò, F. Iacona, et al., Mat. Sci. Eng. B **105**, 197 (2003).

[3] A. Polman and F. C. J. M. van Veggel, J. Opt. Soc. Am. B **21**, 871 (2004).

[4] G. Franzò, S. Boninelli, D. Pacifici, et al., Appl. Phys. Lett. **82**, 3871 (2003).

[5] A. R. Wilkinson and R. G. Elliman, Phys. Rev. B **68**, 155302 (2003).

[6] C. Y. Chen, W. D. Chen, S. F. Song, et al., J. Crys. Growth **253**, 10 (2003).

[7] J. H. Shin, H.-S. Han, and S.-Y. Seo, in *Proceedings of the Nato Advanced Research Workshop on Towards the First Silicon Laser*, edited by L. Pavesi, S. Gaponenko and L. D. Negro, Trento, Italy, 2002), p. 401.

[8] P. G. Kik and A. Polman, J. Appl. Phys. **91**, 534 (2002).

[9] M. Forcales, N. Smith, and R. G. Elliman, submitted to App. Phys. Lett. (2005).

[10] D. Kovalev, H. Heckler, G. Polisski, et al., Phys. Stat. Sol. B **215**, 871 (1999).

[11] A. Polman, J. Appl. Phys. **82**, 1 (1997).

[12] O. B. Gusev, M. S. Bresler, P. E. Pak, et al., Phys. Rev. B **64**, 075302 (2001).

[13] F. Gourbilleau, M. Levalois, C. Dufour, et al., J. Appl. Phys. **95**, 3717 (2004).

[14] J. F. Ziegler, J. P. Biersack, and U. Littmark, *The Stopping and Range of Ions in Solids* (Pergamon, New York, 1985).

[15] A. J. Kenyon, C. E. Chryssou, C. W. Pitt, et al., J. Appl. Phys. **91**, 367 (2002).

[16] A. J. Kenyon, S. S. Bhamber, and C. W. Pitt, Mat. Sci. Eng. B **105**, 230 (2003).

[17] A. Polman, J. S. Custer, E. Snoeks, et al., Appl. Phys. Lett. **62**, 507 (1993).

[18] B. E. A. Saleh and M. C. Teich, *Fundamentals of Photonics* (Wiley, 1991).

[19] P. Pellegrino, B. Garrido, C. Garcia, et al., J. Appl. Phys. **97**, 074312 (2005).

CHAPTER

8

Concluding Remarks

8.1 Conclusions

This thesis examined the optical properties of nanoscale silicon and the sensitization of Er with Si. Predominantly, the role of defects in limiting the luminescence of Si nanocrystals, and the removal of these defects by hydrogen passivation were investigated.

The electronic structure of Si nanocrystals, determined from Tauc plots of PDS data (in the wavelength range of 400 to 1600 nm), showed little variance from bulk Si structure. This is explained by the absorption of large nanocrystals dominating the absorption spectra, due to the broad size distribution in our samples. Absorption data from spectrophotometry was complicated by features due to optical interference. This structure was shown to correlate with the transmittance of the samples as calculated from the modified refractive index profile and small particle absorption for each implant. The Bruggeman dielectric function was found to best describe as-implanted Si-rich SiO_2, whilst after the formation of Si nanocrystals (annealed at 1100 °C for 1 hour) the Maxwell-Garnett function was found to be most appropriate. Large attenuation in the absorption spectra was found at short wavelengths, with both transmittance and PDS measurements. This was found to be due to the high extinction coefficient of Si, which causes a large amount of small particle absorption. Calculations showed Mie scattering is insignificant for Si nanocrystals in SiO_2 when compared to the absorption. This is further supported by the fact that the PDS technique is insensitive to scattering losses.

The choice of annealing environment was found to have a significant effect on the luminescence of Si nanocrystals. PL from samples annealed at 1100 °C in N_2 and FG (5 % H_2 in N_2) were found to be similar, after the effects of hydrogen passivation were taken into account. The Ar environment, on the other hand, produced significantly different PL;

especially after extended annealing times (16 hours). These results are consistent with the common view that annealing in Ar is a simple process of thermal relaxation, while annealing in N_2 is a process of thermal relaxation that is compounded by the exchange of nitrogen with the oxide network. PL and Raman spectroscopy suggest that N_2-containing environments produce smaller nanocrystals, most likely through oxynitridation. This was further supported by PL data which indicates that annealing in N_2 also improves the degree of surface passivation.

The hydrogen passivation kinetics of Si nanocrystals embedded in SiO_2 were studied both isothermally and isochronally with time-resolved PL. This provided a sufficient set of data to extract the reaction-rate parameters with some confidence. The GST model proposed by Stesmans was found to well describe the passivation process of Si nanocrystals in SiO_2. The reaction-rate parameters were found to be $E_f = 1.68$ eV, $\sigma_{Ef} = 0.18$ eV, $k_{f0} = 9\times10^{-8}$ cm^{3}s^{-1} for hydrogen passivation and $E_d = 2.9$ eV, $\sigma_{Ed} = 0.29$ eV, $k_{d0} = 2\times10^{13}$ s^{-1} for hydrogen desorption. The similarity of these values to those found for P_b defects at planar Si/SiO_2 interfaces supports the view that non-radiative recombination is dominated by such defects. The modeling has also highlighted that the simultaneous desorption limits the level of passivation attainable. If the passivation temperature is too high, the desorption reaction dominates. This means that a one-step anneal to both precipitate and passivate the nanocrystals at 1100 °C in forming gas will not achieve the same quality of passivation as a two-step anneal (at 1100 °C) and passivation (at 500 °C) sequence. Moreover, for high temperature annealing the final level of passivation will depend on the cooling rate. On the other hand, using low passivation temperatures to avoid desorption will require extended annealing times. Finally, this work has shown that nanocrystals provide a useful model system for studying such processes using PL. However, since PL is unable to unambiguously identify specific defects, it cannot replace, but instead complements the more complex ESR.

The passivation and desorption kinetics of non-radiative defects in silicon nanocrystals annealed in molecular and atomic hydrogen were studied using time-resolved PL. Annealing in atomic hydrogen was shown to result in greater levels of passivation than were achievable with molecular hydrogen under optimal conditions. This suggested the presence of at least two classes of non-radiative defect: one that reacts with both atomic and molecular hydrogen, and a second that reacts only with atomic hydrogen. This interpretation was supported by hydrogen desorption data that showed a lower activation energy for desorption from sites passivated with atomic hydrogen (E_a = 2.4 eV) than for those passivated with molecular hydrogen (E_a = 3.0 eV). The defect passivation kinetics were modeled by modification of a model developed by Reed *et al.* for atomic hydrogen passivation of defects Si/SiO_2 planar interfaces. After the addition of a Gaussian spread in activation energy, the model was found to adequately describe the passivation kinetics. The reaction-rate parameters extracted were found to be physically reasonable.

The effect of annealing temperature and hydrogenation on the sensitization of Er in Si-rich SiO_2 was demonstrated. The effective excitation cross section was found to increase by a factor of 3 over the annealing range (800 - 1100 °C). However, the PL intensity was shown to decrease, which was attributed to the precipitation of Er due to the Er high concentration (10^{20} cm^{-3} peak). Hydrogen passivation was found to affect the Er PL in the presence of Si nanocrystals, by increasing the intensity and shortening the lifetime. The lifetime shortening was attributed to the fraction of Er inside nanocrystals or at the nanocrystal interface contributing significantly to the PL only after passivation. Ultimately process optimization requires a compromise between optically active Er concentration, efficient Er excitation, and excited state absorption.

8.2 Future Work

Despite the intense research effort directed at porous and nanocrystalline Si over the past fifteen years, an enormous range of questions remain unanswered. As such, there is much scope for increasing the understanding of the electronic and optical properties of current and novel silicon nanostructures. This is significant because, although there is a general understanding of the PL mechanism in nanostructured Si, the exact mechanism has been intensively debated and several models proposed. Detailed studies are, however, hampered by the broad luminescence band resulting from inhomogeneous broadening, omnipresent in ensembles of nanocrystals. Although certain improvement can be achieved by size selection methods, single-dot spectroscopy techniques are needed to reveal the PL mechanism. These methods are widely applied to study individual nanocrystals of III–V and II–VI semiconductors but have only scarcely been used to study light emission from silicon. A recent and exciting development in the area of silicon nanostructures was the fabrication and characterisation of single silicon nanocrystals. These were fabricated through electron-beam lithography and reactive ion etching resulting in Si nanopillars that were subsequently oxidized to produce luminescent silicon cores.[1, 2] The use of single-dot spectroscopy techniques allowed the luminescence from each nanostructure to be individually resolved. The luminescence spectrum, quantum efficiency and blinking characteristics (charging due to photoionization) of the dots were investigated. Possibilities for future work include the effect of hydrogen passivation on the optical properties these and other structures. Through single nanocrystal measurements, there is the opportunity to measure the passivation efficiency directly and definitively, and its effect on the luminescence energy.

Other structures, fabricated using a focused ion beam (FIB) and subsequent oxidation could also be investigated. FIB allows periodic arrays of Si nanostructures to be precisely created from silicon on insulator (SOI) wafers. An interesting phenomenon associated with the fabrication of these structures is the onset of self-limiting oxidation. As the dimensions of silicon structures used for semiconductor components have reduced over the years, it has become evident that the original Deal-Grove model is not completely sufficient for describing the oxidation of silicon. It has long been known that oxidation of a corner is slower than for a surface if the oxidation temperature is below the point of viscous flow of the oxide.[3] This is primarily due to stress build up in the oxide layer due to the curvature, which makes it energetically unfavourable for the oxidation to continue. At a certain curvature the oxidation will stop. Thus, we have a self-limiting process. Using starting structures created with FIB, this technique holds the potential for the creation of nanostructures in a controlled and reproducible way.

Theoretical modeling of materials is an important and fundamental aspect of materials science that will become even more important in the future. There has been much international work on the electronic properties of Si nanocrystals for small Si clusters.[4] However, more basic work, including the thermodynamic stability of nanoclusters based on free energy versus size, has been overlooked. Furthermore, computational investigation into the behavior of hydrogen in the Si/SiO_2 system is warranted. Density Functional Theory (DFT) calculations would allow the effect of hydrogen passivation on the electronic structure of nanostructures to be determined. Molecular dynamics could be used to study the diffusion of hydrogen in this system.

The samples studied in this thesis were prepared by ion implantation. This has the advantage of great controllability and is a standard industry process. However, it also introduces damage into the sample, which requires high temperature annealing to repair. For example, in the case of Er-doped samples, this annealing step is a problem because removal of damage typically requires annealing temperatures where the implanted Er will precipitate and become optically inactive. Sputter deposition could be used to incorporate Er and other materials into Si-rich SiO_2 without the presence of implantation damage. Sputter deposition also provides the capability of creating layered structures, such as superlattices, which have interesting and useful properties.

8.3 References

[1] J. Valenta, R. Juhasz, and J. Linnros, Appl. Phys. Lett. **80**, 1070 (2002).

[2] J. Valenta, N. Lalic, and J. Linnros, Appl. Phys. Lett. **84**, 1459 (2004).

[3] E. P. EerNisse, Appl. Phys. Lett. **35**, 8 (1979).

[4] M. Luppi and S. Ossicini, Phys. Rev. B **71**, 035340 (2005).